STARS

Electronic Theses and Dissertations, 2004-2019

2011

Photodisruption in Ocular Tissue Near and at the Boundary Between the Anterior Chamber and Crystalline Lens

Richard Ty Olmstead
University of Central Florida

University of Central Florida

STARS
Showcase of Text, Archives, Research & Scholarship

PHOTODISRUPTION IN OCULAR TISSUE NEAR AND AT THE BOUNDARY BETWEEN THE ANTERIOR CHAMBER AND CRYSTALLINE LENS

by

TY OLMSTEAD
B.S. Wright State University 1991
M.S. University of Rochester 1992
M.S. University of Central Florida 2007

A dissertation submitted in partial fulfillment of the requirements
for the degree of Doctor of Philosophy
in the College of Optics
at the University of Central Florida
Orlando, Florida

Spring Term
2011

Major Professor Martin Richardson

ABSTRACT

Lasers have been involved in Ophthalmology in the treatment of myopia and hyperopia for several years. Laser systems have transformed patients' quality of life, freeing them from the need for glasses, as in the case of LASIK. Ultrafast lasers have played an important role in surgery of the eye. In LASIK, they are used to cut the flap that is lifted to expose the stroma for UV Excimer laser treatment of this region. They are now being used for surgery deeper into the eye,for instance, treating the lens as part of treatments for cataract surgery. The use of ultrafast lasers in cataract surgery and how they can be applied to achieve better surgical outcomes is the focus of this work. It reports on an investigation of laser interaction at and near the anterior of the lens, in particular the boundary between the fibrous mass, capsule, and anterior chamber of the eye. The study reviews the biomechanics of the eye, develops an interaction model with lens tissue, and reports for the first time clinically studies using *ex vivo* testing of porcine eyes. The components of the treatment laser system are described along with the requirements. Results of the experiments are outlined and discussed, followed by a summary and conclusions including discussion of areas for further research.

This thesis is dedicated to my wife, my parents, and my family who have never failed to support

me during this process. Without your support and inspiration this could not have happened.

ACKNOWLEDGMENTS

I would like to thank my supervisor, Dr. Martin Richardson, for his encouragement and support throughout my academic career at UCF. With his support and guidance, my understanding of this subject area has been greatly increased.

I would also like to thank LensAR for access to equipment and biological materials used during this thesis. LensAR was an enabling entity in the completion of this thesis.

TABLE OF CONTENTS

LIST OF FIGURES

xvi

LIST OF TABLES

LIST OF ACRONYMS

ACD   Anterior Chamber Depth

A-Scan   Amplitude Modulation Ultrasound Biometry Scan

B-Scan   Brightness Ultrasound Biometry Scan

CDE   Cumulative Dissipated Energy

ECS   Energy Control System

EO   Electro Optic

EOM   Electro Optic Modulator

FWHM   Full Width Half Maximum

HAZ   Heat Affected Zone

HpD   Hematoporphyrin Derivative

IOL   Intra Ocular Lens

LASIK   Laser-Assisted In Situ Keratomileusis

LOCSIII	Lens Opacities Classification System III
LTA	Lithium Tantalate
MTF	Modulation Transfer Function
Nd:YVO$_4$	Neodymium Yttrium Vanadate
PDT	Photodynamic Therapy
PRK	Photorefractive keratectomy
SLED	Superluminescent Light Emitting Diode
CCD	Charge Coupled Device
DNA	Deoxyribonucleic Acid

CHAPTER 1 INTRODUCTION

Shortly after the advent of lasers in the late 1950's by Gould and implementation by Maiman (1) and Townes (2), investigations were conducted to investigate the mechanisms of interactions of lasers with biological tissues (3) (4) (5) (6). These early studies defined how lasers interacted with ocular and dental tissue. Some of these studies explored the potential dangers of the laser interaction with tissue (3), while others the possibility of using the laser for treatment (5). The latter of these studies suggested the laser could be used as a tool to aid in the treatment of various conditions of the eye. The unique laser-tissue interaction mechanisms caused the laser to quickly be incorporated into ophthalmologic practice where it was used to treat retinal detachment. As laser technology continued to develop, it found placement in many other surgical applications such as LASIK, cancer treatment, and more recently cataract surgery.

As lasers continued to develop, pulse-widths decreased and new experiments in laser interaction with biological tissues were conducted. Although the pulse-width decreased, the range of useful interaction of biological tissues with lasers appears to be bound in a fluence range of approximately 1 J/cm^2 to 1000 J/cm^2. This range of interaction has led to the classification of temporal interaction regions. These classifications are *photochemical interactions, thermal interactions, photoablation, plasma mediated ablation*, and *photodisruption as* shown in Figure 1 (7). Photochemical interactions are very near continuous wave (CW) for a laser. Thermal interactions are in

the range of CW to the microsecond range. Photoablation is in the range of nanoseconds. Plasma mediated ablation and photodisruption are interactions where the laser pulse width falls below a few tens of picoseconds.

Because of the nature of the biological constituents of the cell, if the laser interaction results in a cell's temperature being raised from a physiologic temperature of approximately 37°C to 60°C for a prolong period of time, irreversible damage to the cell occurs. This prolonged exposure to temperatures exceeding 60°C leads to denaturation of the proteins and collagens in the cell. From a materials interaction perspective, a temperature rise of 5°C typically does not irreversibly damage cells.

In the next sections, a brief description of the different interaction mechanisms outlined in Figure 1 will be expanded on in greater detail.
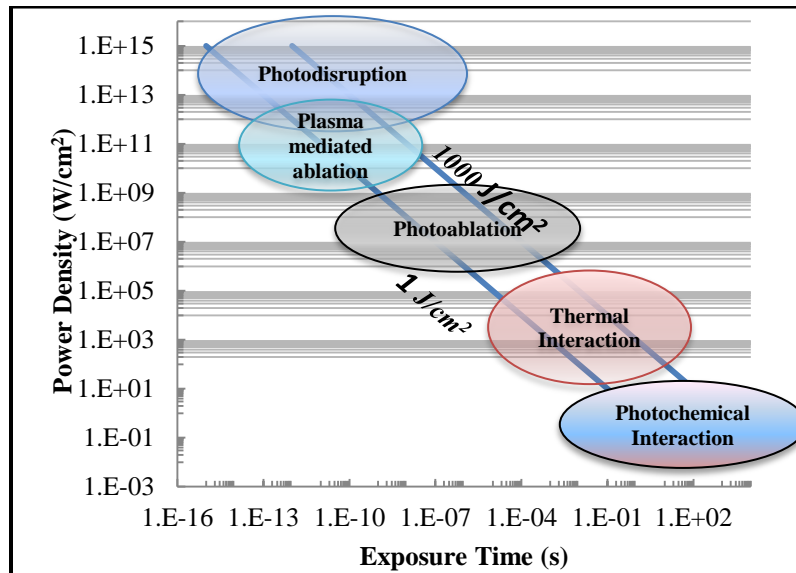
Figure 1 Layout of temporal spectrum versus laser interaction. (8)

1.1   Photochemical Interaction

Photochemical Interaction is a process that takes advantage of chemical interactions caused by photon induced chemical effects. Chemical agents, called photosensitizers, are introduced into the biological system. These photosensitizers then react in a predictable way when exposed to laser irradiation that allows targeted cells to be treated. This type of treatment is typically referred to as Photodynamic Therapy (PDT) (7). Photochemical interactions typically use long exposure times in combination with appropriate wavelengths in order to have sufficient tissue penetration depth to ensure a complete reaction of the photosensitive agents.

The first step in the photochemical interaction process is to incorporate a photosensitizer in to the targeted cells. Once photosensitizer uptake is complete, the cells are irradiated. The photosensitizer is excited by the incident radiation. Medical grade photosensitizers are designed to decay in specific ways, typically having intersystem crossing where a singlet transfers to a triplet state. This triplet returns to a ground state through Type I or Type II reactions. In Type I reactions, the triplet reacts with other organic compounds. This can lead to the development of free radicals in the cell. These free radicals can interact with the triplet oxygen and result in the increase in oxygen dioxide or superoxide anions in the cell. In Type II reactions, the triplet photosensitizer reacts directly with the triplet oxygen resulting in the oxidation of the cell. At the end of this process, the untreated cells are injected with a Carotenoid Protection agent to neutralize the photosensitizer and keep the healthy cells from being damaged. The steps in the reaction are illustrated in Figure 2 (8).
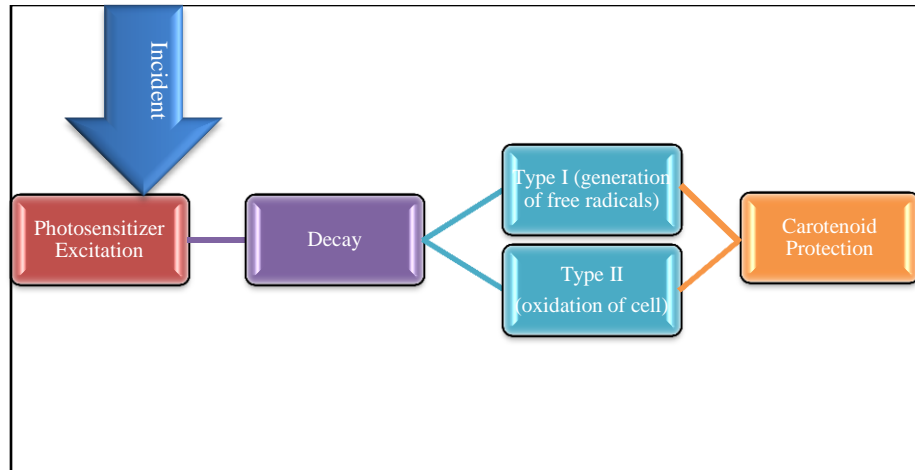
Figure 2 Basic Process in which cell is terminated.

Photodynamic therapies have been successful at treating a variety of conditions such as cancer and dental plaque in the mouth. To treat cancerous tumors a person is injected with hematoporphyrin derivative (HpD) (9) (10). This chemical is metabolized by healthy tissue in about 48 to 72 hours. However, cancerous cells have a harder time metabolizing HpD, allowing these cells to be targeted for treatment without damaging healthy tissue. The patient is sequestered in a dark room while the healthy cells metabolize the HpD. After this period of time the patient is exposed to light and the target cells are destroyed. Photosensitizers have also been used to reduce plaque. Wilson et al. investigated the use of various photosensitizer solutions to reduce dental plaque. He then irradiated the solution with HeNe laser light and measured the population of streptococcus sanguis post illumination. He found that when a 0.0025% (w/v) solution of hematoporphyrin ester was introduced to a population streptococcus sanguis the population of $2x10^8$ went to a population of 10^4 with an eighty second exposure (11).

1.2   Thermal Interaction

Thermal interaction can be used to describe a large variety of laser interactions where the laser is used to raise the temperature of tissue locally. As with photochemical interactions, thermal laser interaction can be used for a large variety of treatments from bacterial removal in a mouth to cancer treatment. Depending on the dosing of the laser, these thermal interactions with the cell can lead to cell decomposition and necrosis. The temperature effects of thermal decomposition are shown in Figure 3. The deposition of laser thermal energy can lead to coagulation, vaporization, carbonization, and melting of the area depending on how the area is irradiated. The processes that govern the generation of thermal effects in biological tissue are absorption of the tissue and exposure time. The area that is affected by the irradiation is related to the effectiveness of the transport of heat away from the target zone. The type of effect observed in the treated tissues is determined by the various parameters of the tissue. A schematic representation of thermal interaction is shown in Figure 4. First the laser irradiates tissue where water, melanin, or other cellular constituents absorb the radiation. Depending on the mechanics of the tissue, some of the energy absorbed by the tissue may be transported to neighboring tissue and cause a thermal rise in this tissue as well. The net area where a temperature increase occurs is termed the net effected treatment zone.
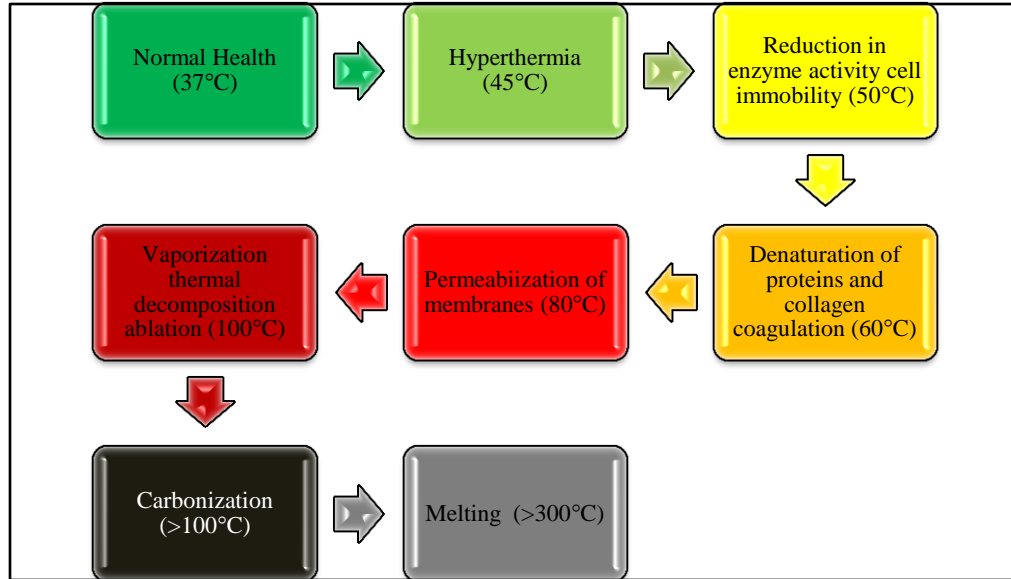
Figure 3 Thermal Decomposition of biological tissue due to laser irradiation (7)
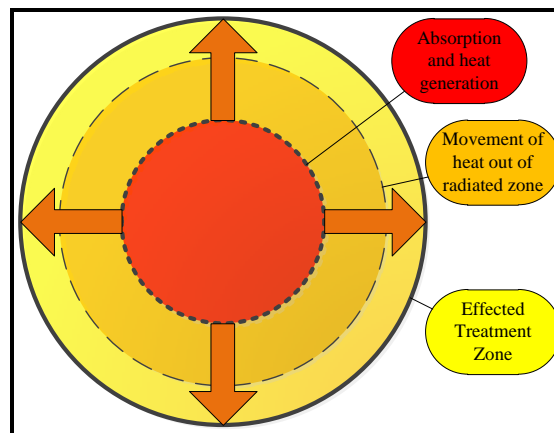
Figure 4 Schematic of thermal interaction with laser

At the molecular level the temperature increase in the tissue develops from the absorption of photons by the molecular vibrational-rotational bands followed by the non-radiative decay of the excited molecules resulting in the temperature increase in the surrounding material. When the laser interacts with a target molecule, A, it reacts in two steps. First the molecule absorbs the photon, $h\nu$, that excites the molecule to a new vibrational-rotational excited state, A*. This molecule then collides with an adjacent molecule, M, through an inelastic collision. Energy from A* is transferred to M resulting

6

in the kinetic energy of M increasing to M*. The magnitude of the increase in energy relates to the increase in temperature of the tissue and is dependent on how much energy A* transfers to M. More concisely, absorption can be described by

$$\text{Absorption:} \quad A + h\nu \rightarrow A^* \tag{1}$$
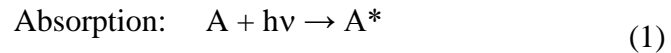
and deactivation can be described by

$$\text{Deactivation:} \ A^* + M(E) \rightarrow A + M(E+\Delta E). \tag{2}$$
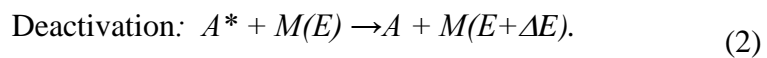
Examining this interaction from an energy standpoint shows that the energy of the lasers being used to thermally treat tissue is approximately five times greater than the nominal kinetic energy of tissue. The average kinetic energy of a molecule is on the order of 0.025eV whereas the photon energy of CO_2 (10.6μm), Nd:YAG (1.064 μm), and Ar (514nm) lasers are 0.12eV, 1.17eV, and 2.4eV respectively.

All of the previous mentioned laser sources have different interactions with the biological materials. These interactions are greatly affected by the absorption coefficients for the various wavelengths. Considering the absorbtions spectrum of water, as shown in The above mentioned laser sources all interact differently with biological materials. These interactions are greatly affected by the absorption coefficients for the various wavelengths. For example, the absorbtion spectrum of water, as in Figure 5, shows that water has an absorption minimum in the visible spectrum that quickly increases as you approach the infrared region of the spectrum. The heat generated by the absorption of the incident beam is

$$Q(r,t,z) = -\frac{\partial I(r,t,z)}{\partial z} = \alpha I(r,t,z). \tag{3}$$

Here Q(r,t,z) is the heat deposited per unit volume, I is the intensity of the incident beam

and α is the absorption coefficient of the material at the laser wavelength.
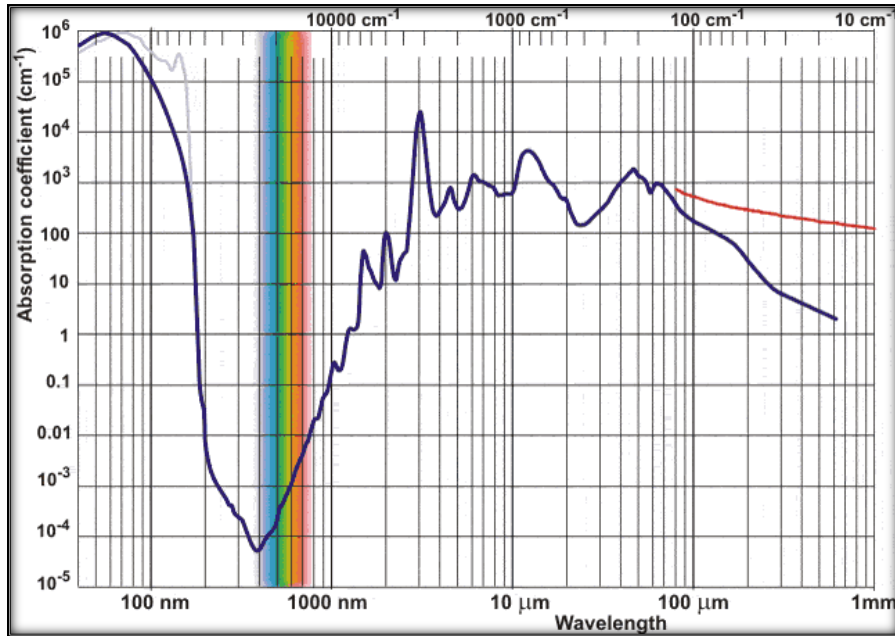
Figure 5 Absorption spectrum of water (12)

The thermal rise in a tissue can be calculated using the above heat equation and

the first law of thermodynamics, however, the time that the beam interacts with the tissue

needs to be considered in this calculation. Pulses that are less than 1 μs can be

considered not to have thermal damage when pulses are not stacked. This can be done

because 1 μs is less than the lowest thermal relaxation time in the visible and near

infrared spectrum. For ultra-short pulses in the range of less than nanoseconds, the

temperature increase in the tissue can be calculated by determining the laser energy that

is absorbed as a heat source and solving for the temperature rise using the first law of

thermodynamics (7). i.e.

$$\Delta T_{max} = \frac{Q}{mc} = \frac{\alpha(\lambda)I}{\varrho c}\tau. \tag{4}$$

In equation 4, ΔT is the maximum temperature rise, m is the mass of the material, ρ is the density of the material, c is the specific heat of the tissue, and τ is the pulse width of the laser, and $\alpha(\lambda)$ is the absorption coefficient as a function of incident wavelength. The specific heat can be approximated to reasonable accuracy using (13)

$$c = \left(1.55 + 2.8\frac{\rho_w}{\rho}\right)\frac{kJ}{kgK}. \tag{5}$$

Here ρ_w is the density of water and ρ is the density of the material of interest. Equation 4 shows a linear relationship between temperature and pulse width. The amount of temperature increase in the tissue is also a function of the wavelength that is related to the absorption coefficient.

One medical application of thermal interaction is in the treatment of posterior opacification of the lens capsule. When the fibrous mass of the lens is removed during cataract surgery, epithelial cells may remain adhered to the capsule. Proliferation of these cells may result in the formation of an opaque plaque between the intra ocular lens (IOL) and the posterior capsule. To treat this condition and improve the patients vision, an Nd:Yag laser is used to treat the posterior capsule. The laser system coagulates the cells and capsular bag behind the IOL, clearing the optical path (14) (15).

1.3   Photoablation

When laser energy approaches the binding energy of molecules, the laser energy is capable of directly causing the disassociation of the molecules. This type of interaction does not cause tissue necrosis because there is no thermal transfer from the laser interaction of the treated cells to neighboring cells. Typical binding energies of biological constituents, shown in Table 1, are in the UV spectrum, thus ultraviolet photons have enough energy to break the bonds of the molecules directly. There are a variety of lasers that can access this part of the spectrum including the ones shown in Table 2. Although these lasers have the advantage of being above the binding energies of various biological molecules, they do not penetrate tissue. This results in photoablation being very effective for surface treatment but incapable of treating below the tissue surface. The ablation depth associated with the laser energy can be related to the threshold intensity by (7)

$$ d = \frac{1}{\alpha} \ln \left\{ \frac{I}{I_{th}} \right\} \tag{6} $$

Here d is the ablation depth, α is the absorption of the material, I is the intensity of the laser beam and I_{th} is the threshold intensity necessary to achieve ablation.

Photoablation is a very effective way to treat biological surfaces; some caution must be paid to the spectral content of the laser being used. DNA has an absorption peak at about 260nm. Radiation in this area of the spectrum can lead to mutations in DNA and have unpredictable effects (16).

This laser interaction is used for ophthalmologic surgical techniques such as laser-assisted in situ keratomileusis (LASIK) and photorefractive keratectomy (PRK). The ophthalmic lasers used for these procedures are ArF lasers that emit at 193nm. This wavelength has a short tissue absorption depth contributing to the minimal risk of mutations within surrounding tissue. In these surgical processes, the stroma is exposed either by using a microkeratome or a laser to expose the stroma, as is the case for LASIK, or by chemically removing the epithelium of the cornea, as in the case of PRK. Once the stroma is exposed the ArF laser is used to sculpt the stroma as necessary to produce the proper power correction for emmetropia. In older patients the vision correction on each eye may be different resulting in mono-vision. One eye is corrected for near vision while the other eye is corrected for distance vision.

Table 1 Binding energies and disassociation wavelength of various carbon molecules (17)

Bond	Energy (kcal/mol)	Energy (J/mol)	Energy (J)	Energy (eV)	Wavelength (nm)
C≡O	258	1080246	1.79E-18	11.21	110.8
C≡N	213	891831	1.48E-18	9.26	134.2
C≡C	200	837400	1.39E-18	8.69	142.9
C=O (CO_2)	192	803904	1.33E-18	8.34	148.9
C=O (amide)	179	749473	1.24E-18	7.78	159.7
C=O (ester)	179	749473	1.24E-18	7.78	159.7
C=O (ketone)	178	745286	1.23E-18	7.73	160.7
C=O (aldehyde)	177	741099	1.23E-18	7.69	161.5
C=O (halide)	177	741099	1.23E-18	7.69	161.5
C=N	147	615489	1.02E-18	6.39	194.5
C=C	146	611302	1.01E-18	6.34	195.8
C=S (CS_2)	138	577806	9.59E-19	6.00	207.1
C–C	83	347521	5.77E-19	3.61	344.4

Table 2 Lasers with photon energy in the UV

Laser	Wavelength(nm)	Photon Energy (J)	Photon Energy (eV)
F_2	157	1.250E-18	7.81
ArF	193	1.030E-18	6.44
KrF	248	8.014E-19	5.01
Nd:Yag (4ω)	263	7.557E-19	4.72
XeCl	308	6.453E-19	4.03
XeF	351	5.662E-19	3.53

1.4   Plasma Mediated Ablation

Biological matter breaks down when intensities reach 10^{10} to 10^{12} W/cm^2 (18).

For a 10 pico-second laser this corresponds to an energy density in the range of 0.1 J/cm^2

to 10 J/cm^2. In the near infrared, where many present solid state short pulse length lasers

are presently developed, the linear absorption of various biological components is low, resulting in larger penetration depths. the absorption spectrum for some biological components. Because of the large penetration depths, near infrared light can be focused deep into the tissue, which is something that photoablative lasers cannot achieve. This is advantageous for ophthalmic treatments because the laser can be focused at any point within the eye. To reach the point of ablation though, plasma mediated ablation relies on the nonlinear absorption coefficient that is dependent on the incident laser intensity. Ultra-short lasers have very high intensities that make them ideal for this application. An electron density needs to get to approximately 10^{21}cm^{-3} to ignite plasma. To reach this density in a low absorption material, the laser intensity needs to exceed a threshold to allow for sufficient excitation of electrons in the media. This absorption is done through multi-photon excitation, which then leads to avalanche excitation. Multi-photon ionization refers to the excitation of a molecule caused by multiple photons combining to excite an electron. A simple schematic of this is shown in Figure 7, here several photons add linearly to excite an electron to the valence band of the material. The excitation energy of water is approximately 6.5eV, if water is considered as an amorphous semiconductor (19). For a laser with a central wavelength at 1064nm this corresponds to a requirement of 6 photons to raise one electron to the ionization energy.
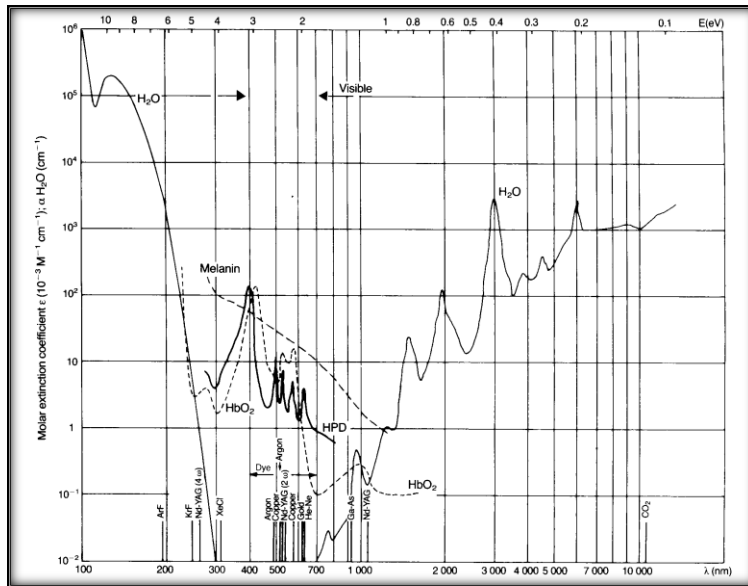
Figure 6 Absorption spectra of various biological components (8)
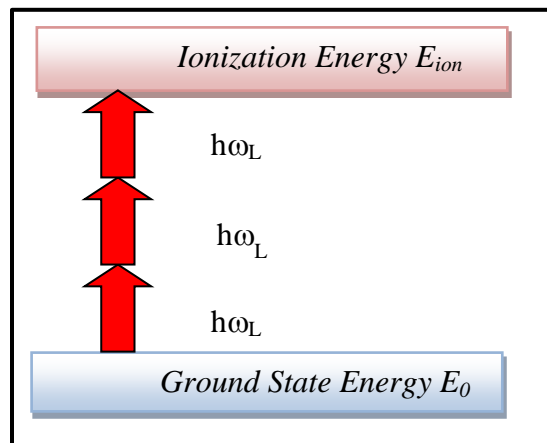
Figure 7 Schematic of multi-photon ionization

Once an electron or electrons are in the valence band of the material they are capable of absorbing more photon energy via inverse Bremsstrahlung. These electrons are accelerated to the point that when they collide with other atoms they free electrons from the atoms. These free electrons absorb more energy from the photons in the laser field and accelerate, collide with other atoms and free more atoms. This process causes an avalanche of electrons to be freed. A schematic of this process is shown in Figure 8. In water the time between collisions is approximately 1fs as reported by Vogel (20). The

final electron density is resultant from both multiphoton ionization and avalanche
ionization.
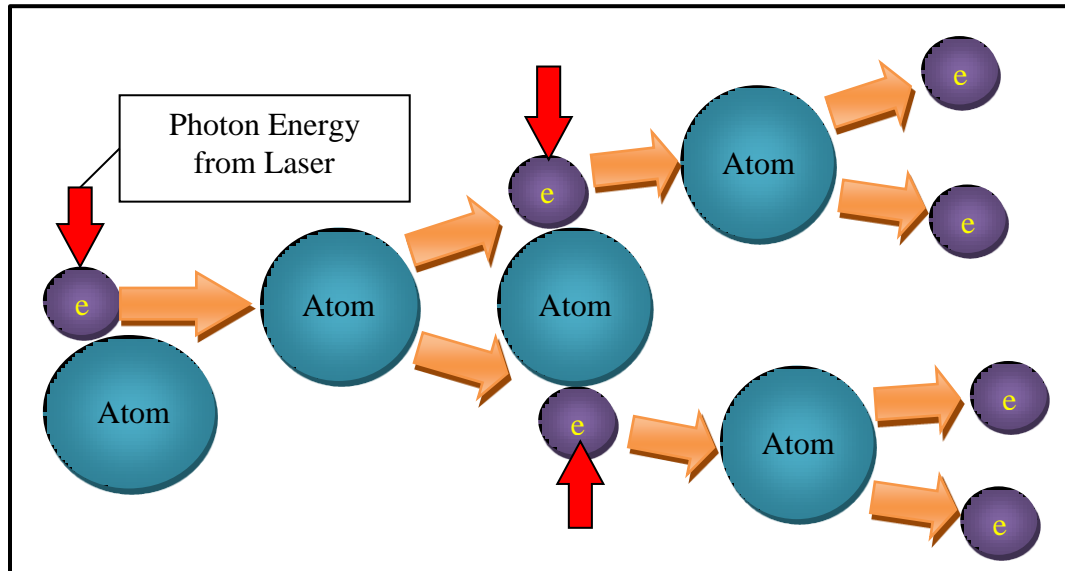
Figure 8 Avalanche Ionization of electrons

1.5   Photodisruption

Photodisruption is similar to plasma mediated ablation except there is more
energy available that generate stronger shock waves and other mechanical effects when
photodisruption occurs. If the energy is high enough, these mechanical features will
dominate the plasma interaction. Figure 9 shows the processes that are necessary to
achieve plasma mediated ablation and photodisruption. Photodisruption and plasma
mediated ablation have similar energy requirements, but there is more energy to form
cavitation bubbles and make stronger shock waves in photodisruption.
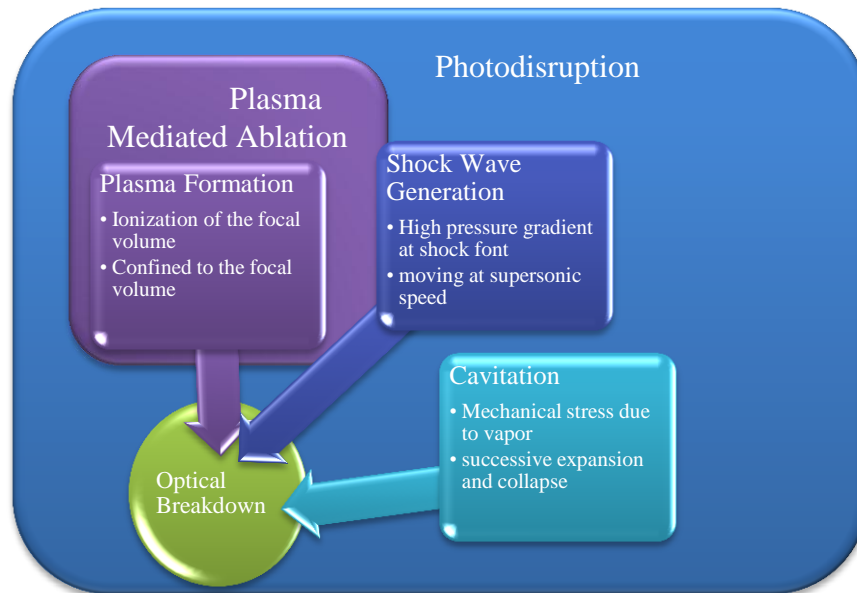
Figure 9 Comparison of interaction that results in optical breakdown in the case of Plasma Mediated Ablation and Photodisruption.

When plasma is formed during optical breakdown in tissue, the plasma reaches a temperature of several hundred degrees Kelvin. The electrons in the plasma have high kinetic energy, which gives rise to the high temperature of the plasma. As the electrons flow out of the plasma volume energy is transferred into the surrounding media, which is not within the laser plasma. This transfer of energy results in a shock wave propagating away from the plasma volume. The speed at which this initially occurs is hypersonic, but then slows down to the speed of sound in the material. The temperature rise in the focal volume of the beam happens in tens of picoseconds. The temperature rise in the focal volume of the beam happens in tens of picoseconds. This temperature rise is due to the thermalization of the free electrons. For a nominal system with a focal spot of approximately 2 microns in diameter, the acoustic wave would not make it out of the focal volume from the center of the focal volume in the time of the pulse. This results in the focal volume experiencing the maximum thermo elastic stress. To conserve momentum, the focal volume must be exposed to both compressive stresses and tensile

stresses causing this region to experience the maximum pressure due to the laser. The tensile stress in the focal volume may result in the material fracturing. In biological tissue this results in a bubble forming within the material (7).

Photodisruptive lasers are used daily in ophthalmology. They are used to make the flap in LASIK Surgery. The laser is targeted approximately 150 microns below the corneal surface and then raster scanned across the eye to make a flap. At the completion of the raster scan an edge incision is made along the edge of the flap. The surgeon then uses a blunt instrument to free the flap from the rest of the cornea. Once the flap is free it is folded out of the way to expose the smoothly incised stromal bed. A photoablative laser is then used to recontour the stroma to provide appropriate corneal curvature for emmetropia.

1.6   Objective of this study

Lasers have been involved in medical applications for many years. The medical profession has leveraged the strengths of lasers to develop a variety of treatment options. The specialty of ophthalmology has greatly benefited from the induction of lasers into medical practice. Lasers have enabled surgeons to treat many conditions without physically entering the eye (7) (21) (22). In cases of both intraocular and non-invasive surgery, the laser provides a predictable tool that aids the surgeon in achieving the best possible outcomes. Laser systems have transformed ophthalmic patients' quality of life by being involved in areas ranging from improvements in visual acuity, as in the case of LASIK, to aiding in cataract surgery by processing the lens to reduce the need for phacoemulsification (23).

The objective of this study is to investigate ps laser interaction at the anterior lens boundary. From a review of the literature, there has been significant work done in the area of lasers being used in the cornea for photodisruption, ablation, and sensing (24) (25) (26) (27) (28) (29) (30) (31). These studies, along with others, have helped industry in developing and guiding corneal refractive correction using laser-based systems. As of late there has been a growing interest in the area of laser cataract surgery (32) (33) (34) (35) (36) (37) (38) and more specifically how ps lasers can be applied to achieve more consistent outcomes in the surgical process. This has led to the commercialization of this industry and the founding of several companies pursuing the laser cataract market (39) (40) (41) (42). To date there has been much work in the area of posterior capsulotomies using Nd:YAG lasers (43) but little work done in understanding the laser physics across the anterior lens and capsule (44).

This study will investigate the laser interaction at and near the anterior surface of the lens, in particular the boundaries between the fibrous mass, capsule, and anterior chamber. First, the biomechanics of the eye will be discussed, leading to an investigation of the aging lens and eventual lenticular disease in the form of cataracts. A review of the standards of care for the aging lens and a look at the aspects of cataract surgery will follow. This will result in an understanding of why laser processing is warranted in the treatment of cataracts and how laser treatment of the capsule is useful.

In Chapter 3, the fundamental laser physics that will lead to the development of a description of the electron cloud population and how it relates to the formation of plasma will be explained. This foundation will be used to model the evolution and length of the plasma in Chapter 4. Additionally, the heat generation aspects of the laser interaction

18

with the ocular materials will be looked at to ensure that thermal damage to surrounding tissue is not significant. Thermal damage may lead to poor capsulotomy characteristics.

Chapter 4 will expand on the laser physics discussed in Chapter 3 and determine if consideration of Keldysh's more formal derivation for ionization is warranted in the analysis of the electron density. The effects of the capsule at the boundary between the fibrous mass and anterior chamber on the plasma evolution in electron density and effects on the length of the plasma will then be investigated to determine characteristics of the interaction of the plasma across the capsule This will be done by looking at 3 cases: 1) plasma generation in a uniform medium; 2) plasma generation in two media; and 3) plasma in three transparent media and the effect of different binding energies on the generation of continuous plasma.

In Chapter 5 the physical characteristic for an F/4.2 system with a 10ps laser capable of being used in the medical treatment of ocular tissue will be described. This system allowed the study of the laser interaction physics across the boundary of the lens capsule which will be addressed in Chapter 6 and 7.

Chapter 6 will study formation of plasma in water and gelatin. Effects of incident laser fluence on the evolution of the plasma in water, to identify photodisruption characteristics length, width, and shock wave with increased fluence will be examined. Photodisruption characteristics in gelatin will then be compared and contrasted to that of water. This will help in the understanding of how the plasma acts in stratified media. The work in gelatin will also help in characterizing the evolution of the pulse over a longer period of time in stratified media. Understanding the evolution of the

photodisruption will allow appropriate laser characteristic identification for incising the anterior lens.

In Chapter 7, photodisruption in the eye is examined. In vitro testing of porcine eyes is used to investigate laser behavior in the eye. These eyes are similar to human eyes and are readily available. The study targets the anterior lens. A series of laser pulses are moved across the capsule starting in the fibrous mass. This will allow the threshold in the fibrous mass and in the capsule to be determined. Additionally, by changing the axial distance between successive layers of shots, effects on the porcine capsule due to different axial shot spacing can be studied. This will be done at several fluence levels to see how the process evolves. The results of this testing can then be used to determine various aspects of laser interaction at the anterior of the lens.

In Chapter 8, a summary of the key conclusions, achievements, and areas for further research is presented. At the completion of this study, new areas of research are identified and guidance is provided. Direction of better techniques for performing capsulotomies is also given.

This chapter has introduced the reader to this thesis by outlining the subject area, the objectives, the approach, and the outline of this effort by indicating the methodology and approach by chapter.

CHAPTER 2 THE EYE

In this chapter, the anatomy of the eye and characteristic dimensional values for a population of cataractous Filipino patients will be presented. Anatomical data that is related to the research of this thesis are the cornea, anterior chamber, lens, and the vitreous which are illustrated in Figure 10. A better understanding of these tissues' structures may elucidate the manners in which lasers will beneficially interact. From the clinical data, an anatomical optical model of the eye will be built to look at the expected performance of the eye with age. A-Scan data collected from Filipino cataract patients were analyzed to build an anatomically correct patient model.
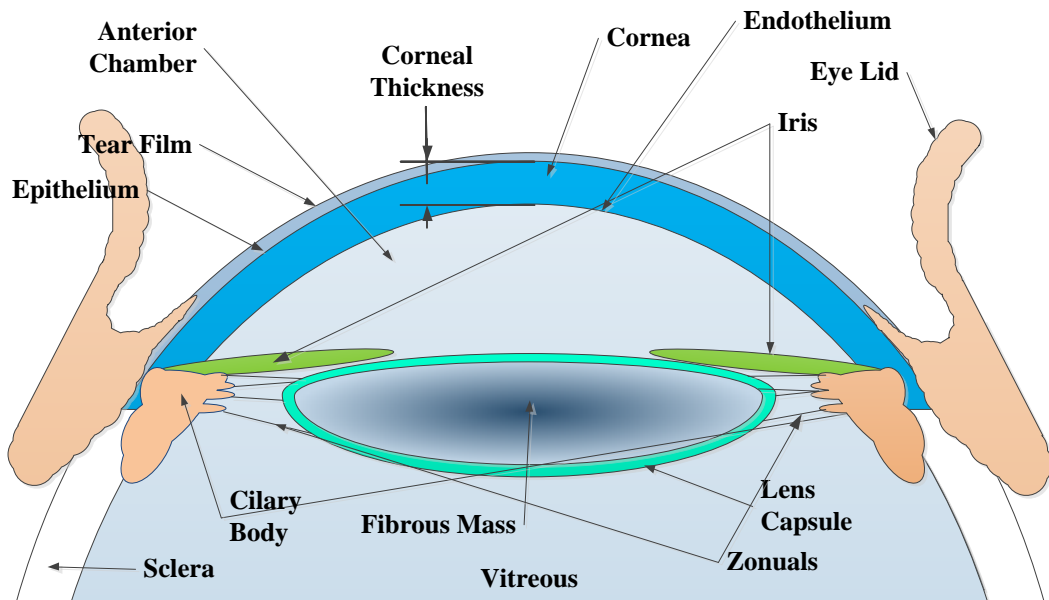
Figure 10 The anterior segment of the eye.

2.1 The Eye: an overview

The human eye is a complex optical system that is capable of dynamically adjusting to its environment in a way that allows visualization of one's environment under various external conditions. The eye does this by actively manipulating the constituents that make up the eye to accommodate to the environment. The lens and iris are actively manipulated to adjust the imaging capabilities of the eye to focus objects of interest on the retina. The components of the eye that limit the amount of retinal incident light are the sclera and iris. The sclera is the white wall of the eye. This fibrous material is difficult to penetrate helping to protect the inner workings of the eye (45). The iris lies along the plane of the anterior surface of the lens, in the posterior portion of the anterior chamber. The main function of the iris is to control the amount of light that is incident on the retina and the depth of focus, which is done by dynamically changing based on external stimuli or internal stimuli. If the brain perceives an object out of focus the iris is constricted to increase the depth of focus (46). The pupil is a central opening in the iris that can increase or decrease in size, controlling the intensity of the light incident on the retina. In dark conditions the iris opens the pupil, allowing more light to enter the eye. In bright conditions the iris sphincter constricts to limit the intensity of the light on the retina. Additionally, the iris may play a role in the accommodative response of the lens (47). The other component of the eye that is actively manipulated is the lens. The lens' main function is to adjust the focus of the light incident on the retina so that the brain perceives a clear image of the observed object, a process referred to as accommodation. As the eye ages, changes in the lens lead to a diminished range of accommodation (48), which when severe enough to affect visual acuity is referred to as presbyopia. The onset

of presbyopia starts by the early 40s reaching full maturation by the mid-50s to early 60s (49). As the lens continues to age, defects in the growth patterns of the fibrils can slowly cause a condition called cataracts. Cataracts result in the imagery projected on the retina becoming hazy and blurred (50) (51), due to the lens having more scattering and possible obscurations. The scattering resultant from a progressing cataract increases until vision is completely obscured.

Laser irradiation must first pass through the cornea and anterior chamber in order to be focused in the lens. The laser energy that is not absorbed by the cornea, anterior chamber, and the lens continues through the vitreous to the retina. In the next sections a more detailed description is given of the different major components of the eye that a laser treating the lens propagates through and disrupts: the cornea, the anterior chamber, the lens. Additionally the vitreous will be discussed as it pertains to building an anatomically correct optical eye model. Notably, the iris is not considered a major component of the eye during laser surgery because the iris is pharmacologically dilated to expose as much of the lens as possible. Other than playing a role in limiting the field of view of the lens, the characteristics of the iris are unimportant for this study.

2.2   Cornea

The cornea makes up the majority of the refracting power of the eye, having approximately 42 Diopters of power (52). The cornea can be broken into five separate segments: epithelium, Bowman's layer, stroma, Decement's membrane, and the endothelium. Typical thickness values for each of these layers are shown in Figure 11.
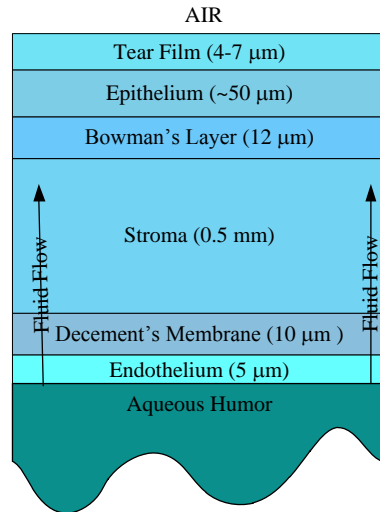
Figure 11 Layers making up the cornea of the eye

The outermost tissue layer of the cornea is the epithelium. This layer is approximately 50 μm in thickness. The epithelium protects the eye from toxic substances and larger molecules that try to penetrate the eye (52). The outermost cells of the epithelium are shed every 3 to 5 days. These cells are regularly replaced by the deepest layer of cells of the epithelium that are sitting on the basement membrane just above Bowman's layer. Only this deepest layer of cells of the epithelium goes through active mitosis (53).

Under the epithelium is the basement membrane and Bowman's Layer. Bowman's layer is found in most primates with the exception of the lemur (54). It is made of a layer of randomly arranged fibrils first discovered by William Bowman in 1947. Bowman's layer is an elastic lamina with a thickness of approximately 8 to 14 μm. Bowman's layer helps to protect the cornea from injury. Bowman's layer is the most anterior portion of the stroma (46).

The largest part of the cornea is the stroma, which is approximately 0.5mm thick. The stroma is composed mostly of aligned fibrils forming lamellae from 9 to 260 microns wide (46). Each of the lamellae layers of collagen fibrils run parallel to each other within a layer. Lamellas on different layers of the stroma run obliquely to the surrounding layers (55). This helps maintain the clarity of the cornea and increase its mechanical strength (56).

Descement's membrane is the basement membrane for the corneal endothelial cells. It slowly increases in thickness throughout life but is nominally 10 to 20 microns thick. This membrane helps protect the eye from infection.

The endothelium is the last layer of the cornea before the aqueous humor. The endothelium consists of a single layer of cells. These cells have a hexagonal appearance, making a honeycomb pattern on the back of the cornea. Endothelial cells regulate the fluidics of the cornea by keeping the stroma hydrated to about 78% water by volume (52). These cells do not undergo mitosis, but endothelial cells enlarge to fill any voids created by cell death (46). The health and clarity of the cornea can become compromised when significant endothelial cell loss occurs.

Optically the cornea can be thought of as a meniscus lens with two axes of power. In a population study conducted in the Philippines, the corneal radii of curvature of 487 eyes were measured (Figure 13). The average major corneal radius of curvature was found to be 7.568 mm, with a standard deviation of 0.251 mm. The mean of the minor radius was found to be 7.708 mm with a standard deviation of .267 mm. The mean thickness of the cornea measured for 600 eyes was found to be 0.540 mm with a standard

deviation of 0.037 mm (Figure 12). From the literature, the posterior curvature is nominally 6.5 mm with a range of 6.2 to 6.6mm (57). The index of refraction of the cornea is dominated by the index of refraction of the stroma having an effective index of 1.3771 (57).
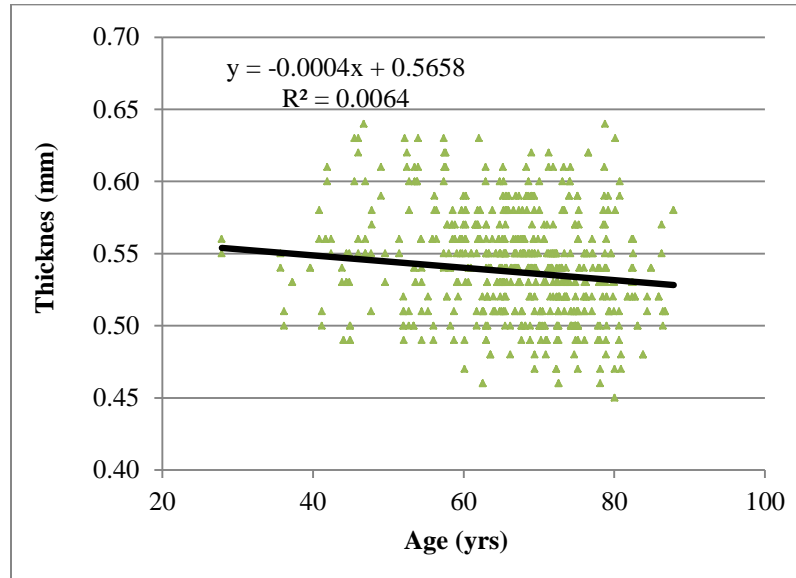
Figure 12 Plot of the Corneal Thickness for 600 eyes in a Filipino population measured with an ultrasound A-Scan.
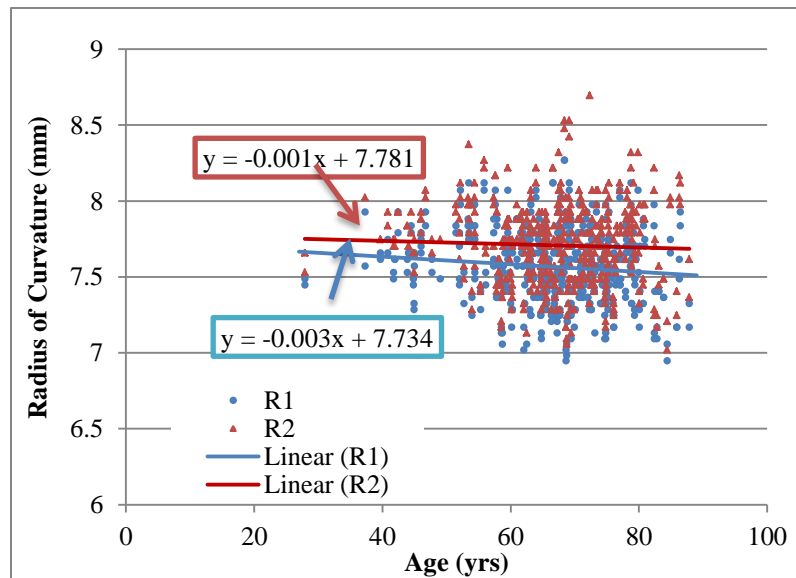
Figure 13 Minor (R1) and Major (R2) Corneal Radius of Curvature for 487 eyes in a Filipino population measured with an ultrasound A-Scan.

2.3   Anterior Chamber

Immediately posterior of the cornea is the anterior chamber, which is filled with a fluid called aqueous humor. Aqueous humor is produced in the posterior chamber, the area between the iris and the lens, by the ciliary epithelium, which lines the ciliary processes. It is used to nourish the avascular tissues of the eye, such as the cornea and lens. The aqueous humor is an electrolytic fluid made up of constituents including chlorides and bicarbonates, but is mostly water (58). The fluid dynamics of aqueous production and outflow generates approximately 15 mmHg pressure within the eye that is necessary to maintain its shape and optical characteristics. The aqueous humor leaves the eye passively through the trabecular meshwork and across the inner wall of Schlemm's canal. Convection of the aqueous humor within the anterior chamber occurs due to a temperature gradient, aqueous humor that is closer to the cornea is cooler than fluid near the lens.

Aqueous humor has an optical index of 1.3374 (57) but is treated as water for the purposes of modeling laser interaction. Water has shown behavior like an amorphous semiconductor with a binding energy of 6.5eV (19). The depth of the aqueous humor in the eye is referred to as the anterior chamber depth (ACD). Like the cornea, the anterior chamber depth varies between patients. In Figure 14, 572 ACD A-Scan measurements are plotted versus age. The average ACD was found to be approximately 3.115mm for a population ranging in ages from 27 to 89. A linear fit of the data results in a gradual trend in the plot that indicates that the anterior chamber shallows with age. This is consistent with gradual lens growth over time.
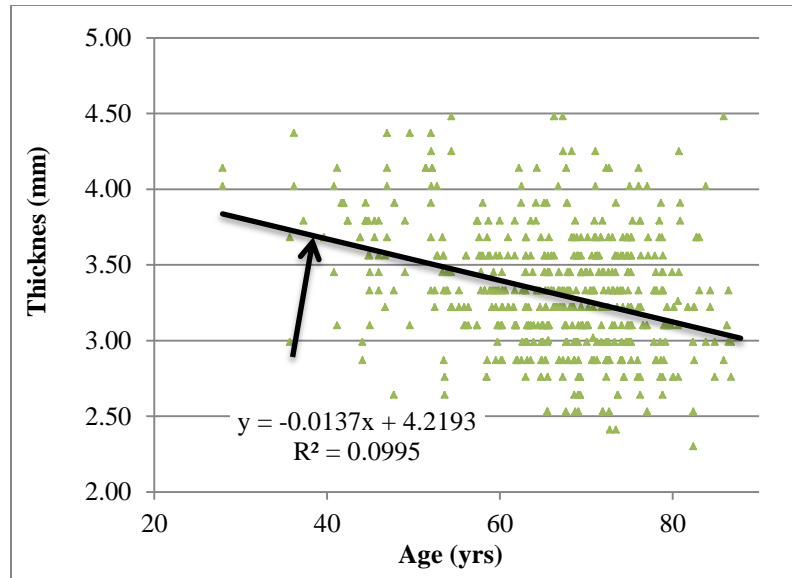
Figure 14 Anterior chamber depth of 572 Filipino eyes in a Filipino population measured with an ultrasound A-Scan.

2.4   Lens

The lens controls the optical power of the eye by changing shape and position. The shape of the lens is manipulated by changing the tension applied to the lens capsule via the ciliary muscle.   The ciliary muscle is coupled to the capsule by zonular fibers that attach to the capsular bag near the edge. When the ciliary body contracts, the muscle moves centripetally, relaxing the tension of the zonules on the capsule. This allows the lens to become more spherical, thickening centrally, and results in accommodation. In contrast, when the ciliary body is relaxed, the zonules and lens capsule have the most tension on them, which places the lens into an unaccommodated, flattened, state allowing for distance viewing. A schematic of the lens is shown in Figure 15.

Inside the lens capsule, the lens is a highly organized set of cells that are laid down in concentric shells much like an onion. The cells are structurally arranged to maintain clarity of the optical field whether the lens is flattened or rounded. This

structure is made up of cells that are not metabolically or mitotically active. The germinal centers for the lens are located at the lateral margin of the lens capsule. These cells divide at a progressively slower rate as aging occurs (46). As the marginal epithelial cells divide, the cells start to elongate across the surface of the lens. During this process, the elongated cells lose their organelles and become less metabolically active (59) and do not replicate. These elongated cells are sometimes referred to as fibers. The lens continues to grow at a predictable rate throughout the life. The center of the lens is composed of the fibrils that formed during gestational infancy and is referred to as the fetal lens. The adult lens is often divided into two regions, the central region, the nucleus, and the outer zone, the cortex. These fibrous are resultant from lens growth after infancy. The lens is unusual in that it does lose cells during its growth. This results in the lens growing approximately 1.5 times its original size though out the life (46). In this thesis, the nucleus and cortex are referred to as the fibrous mass.
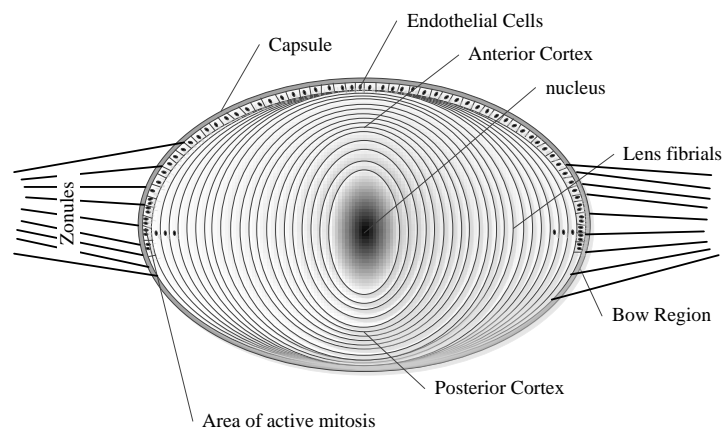
Figure 15 Cross sectional view of the Lens

Optically the lens changes as it ages. Early in the life cycle of the lens there is a gradient index of refraction across the lens. The index of refraction gradient goes from

the outer portion of the lens to the nucleus of the lens. Later in life the gradient changes

becoming less across the lens. For an older person the index of refraction becomes more

constant across the lens, reducing the effect of the changes in the radius of curvature (60).

The index of refraction was reported by Jones et al to be $n_c = 1.4204(\mp 0.0039) - $

$5.1(\mp 7.9)x10^{-5} * Age$ for the center region of the lens and $n_s = 1.3709(\mp 0.0020) - $

$3(\mp 400)x10^{-7} * Age$ for the surface of the lens (60). The mean population anterior

radius of curvature of the lens is 10.2 mm. This radius of curvature has a range of 8.8 to

11.90mm in the population (57). The posterior radius of curvature is approximately

6.45mm (52) with a range of 6.81 mm to 5.4 mm. Lens thickness changes over age.

Figure 16 shows the lens thickness of 562 eyes versus age in a Filipino population

evaluated for clinical purposes. The average lens thickness for this population was 4.438

mm with a standard deviation of .579 mm.

The capsule is made primarily of a Type IV collagen. It is approximately 20 μm

in thickness in human eyes. It is approximately 40 μm thick in the porcine eye.

Collagens are a natural occurring protein in animals. In the protein structure are peptide

bonds that have a core functional group of –(C=O)NH- called a peptide link. The

covalent bonds have a binding energy of approximately 7.8 eV. The fibrous mass is

made of cellular elements, with a high concentration lens crystallines, and water (61). It

is approximately 70% water with 30% protein. The cell walls of the fibrous mass are

lipid bilayer, but the water soluble crystallines are proteins. The lens being 70% water is

similar to the aqueous humor and its binding energy for water. To approximate the net

binding energy of the water and collagen mixture of the fibrous mass a combination of

70% binding energy of water is added to 30% binding energy of the covalent protein

bonds bond. Using this approximation the binding energy of the fibrous mass is close to the binding energy of water having an effective binding energy of 6.8eV.
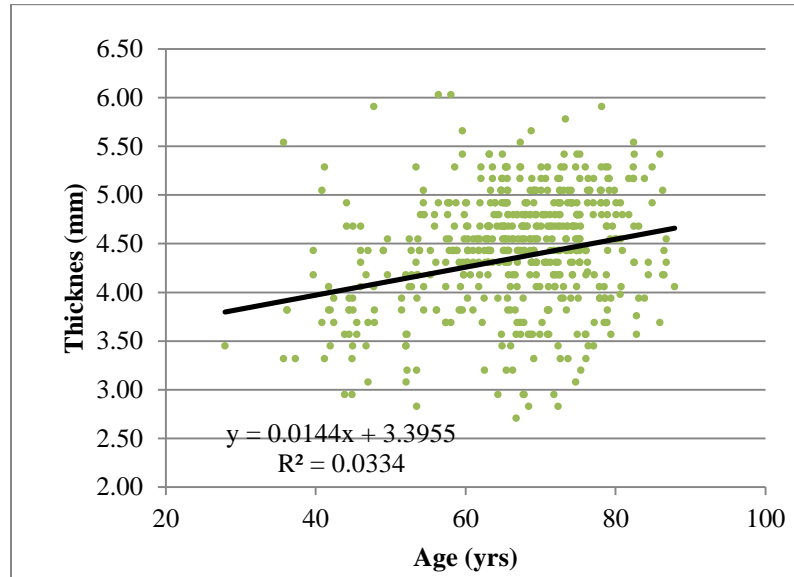
Figure 16 Lens thickness versus age for 562 eyes in a Filipino population measured with an ultrasound A-Scan.

2.5   Vitreous

The vitreous makes up approximately 80% of the volume of the eye. Vitreous is a colorless and gelatinous material. In the mature vitreous the body of the vitreous is not completely homogenous having both an anterior and posterior cortex. The anterior cortex or hyaloid is approximately 30 μm thick. The posterior cortex of the vitreous is approximately 100 μm thick. In the cortex the collagen fibrils are densely packed. The index of refraction of the vitreous is approximately 1.336. The chamber filled by the vitreous was found to have an average axial length of 15.201 mm with a standard deviation of .972 mm in a population of 538 Filipino eyes. A plot of the distribution of the vitreous lengths is show in Figure 17.

$$y = -0.0139x + 16.112$$
$$R^2 = 0.0223$$
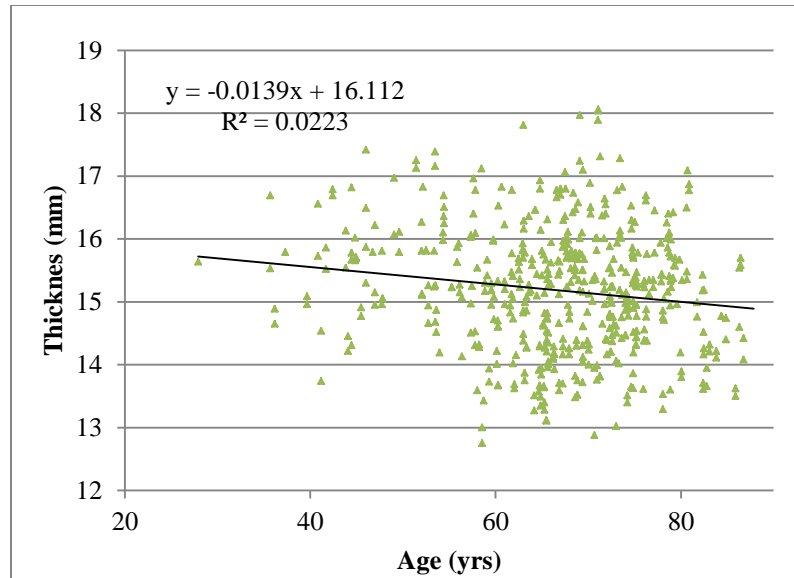
Figure 17 Vitreous length of 538 Filipino eyes in a Filipino population measured with an ultrasound A-Scan

2.6   The Aging Eye

As the eye ages, it slowly loses efficiency in working as an accommodative optical system. This is primarily due to the lens of the losing the ability to alter its shape in response to ciliary contraction.

2.6.1   Presbyopia

As a person ages, they slowly lose their ability to focus at reading distances. This loss of accommodation with age is called presbyopia. The primary source for the loss in accommodative response is the hardening of the lens (49) (62) (63). Although other parts of the eye age and lose some function, the slow hardening of the lens is believed to be the primary reason for the loss in accommodation. A gradual loss in accommodation is seen though out life starting at about age 8. Full loss in accommodation is typically complete by age 60.

2.6.2   Cataract

As the crystalline lens ages, cataracts develop reducing the visual acuity and reducing the retinal illumination. This disease occurs as opacities form in the lens. Theses opacities may lead to eventual blindness. There are many theories to the cause of cataract (64) (65) (66) (67) (68) (69). The severity of cataract is graded clinically. There are several ways that cataracts are graded clinically based on their severity (70) (71) (72) (73) (74). The primary method of grading cataracts used by ophthalmologists is presently the Lens Opacity Classification System version III, LOCSIII. LOCSIII grades cataracts base on opacity and color.   At each level of cataracts, the patient's vision is affected differently. In the case of a white cataract the patient is blind and cannot see any detail of their environment, except light or darkness. From a laser interaction standpoint each level of cataract has a different scattering coefficient that will result in laser energy being lost as the laser is focused in the lens.

2.6.3   Standards of Care

To treat different ailments of the eye different standards of care are used. For hyperopic or myopic patients corrective lenses are normally prescribed or Lasik surgery is used to improve the patient's vision. In the case of Presbyopia, the patients distance vision may require a different optical correction than that for near vision. This is treated with the use of bifocals (75), Dual focus Lasik surgery (76) (77) (78), insertion of a multifocal IOL (79) (80) (81), refilling the lens capsule (82) (83) (84), or more recently laser treatment of the lens (85) (86) (32).

If an eye is cataractous, surgical intervention is required to improve the patient's vision. Cataracts are removed surgically by an ophthalmologist, who starts the process by making a small stab incision in the sclera just posterior to the limbal margin (87) (88) (89) (79). Through this incision the surgeon injects a viscoelastic material to protect the cellular lining of the cornea and the tissues of the uvea (iris and ciliary body) (90) (91) (92). This is used to help protect the endothelium cells of the cornea from being damaged. The next step in the procedure is the capsulorhexis (capsule tearing). The surface of the capsule is punctured using a needle with an angle in the sharp beveled tip. The surgeon than grasps the edge of the capsular rent and by using delicate traction tears a circular window in the anterior lens capsule (93) (94) (95) (96) (97). At the completion of the capsulorhexis, the fibrous mass is decoupled from the capsule by hydrodissection (98) (99). This is done by placing a cannula between the lens capsule and fibrous mass and introducing balanced salt solution to free the fibrous mass from the capsule. The fibrous mass is then split into four quadrants using the "divide and conquer" technique. An ultrasonic phacoemulsification device is used to remove the pieces of the fibrous mass. The phacoemulsification device uses both an irrigation system along with vibrational waves to remove the lens material from the capsular sac. The amount of acoustic power used during the phacoemulsification process is recorded in units of cumulative dissipated energy (CDE). As the hardness of cataract increases, the CDE will increase. At completion of the phacoemulsification process, the ophthalmologist switches to an irrigation and aspiration hand piece to finish the removal of any residual fibrous material from the capsular sac. Once all the fibrous mass is removed from the capsular sac, the sac is then filled with viscoelastic to protect the posterior of the capsule

from being punctured. The initial surgical incision in the cornea is approximately 2mm

to allow the placement of an intra-ocular lens (IOL) in the capsular sac (79). The IOL is

inserted and manipulated to place the optic centrally within the capsular opening. The

surgeon then removes the viscoelastic from the anterior chamber and lens bag,

replenishing the chamber with balanced salt solution. In the final step the corneal

incision is closed using the syringe to cause edema at the incision site.

2.7   Anatomical Optical Model of the Eye

From the clinical data presented in the previous sections an optical model can

constructed for the average Filipino eye of a prescribed age within the Filipino sample.

Although this model incorporates the data from the clinical information there are still

some shortcomings in the data. No data is available from this patient population for

conic constants for the cornea, the conic constant of the lens, the posterior or anterior lens

radius of curvatures, or index of refraction for each element of the eye. Not having this

information does limit this model, but some insight is still obtainable. Using the norms

from the general population presented in David Atchison's book *Optics of the Human

Eye* (52) for the parameters of the unknown values, a realistic eye model can be generated

for the average Filipino of a prescribed age. Eye models for ages 27, 40, 60, and 80

presented in Figure 18 through Figure 21. In each of these figures, an image of the eye

model, a spot size diagram, and the eye's MTF is shown. On each model the lens was

optimized to reduce the spot size on the retina. The lens was approximated by an even

asphere with one aspheric term beyond the conic constants. The conic terms were

allowed to vary in the range of published data for the eye (52). The aspheric term on the

posterior and anterior surfaces of the lens were allowed to vary as well. The lens model

uses an approximation for the gradient index nature of the lens by breaking up the lens

into six symmetric gradient index subsections. For the case of the 27 year old a close to

diffraction limited spot size was obtained, being able to barely resolve the expected

resolving power of 1 arc min. As the models for age increase the resolving power of the

clinically based model eye becomes less. The index shells of the lens behave as expected

for the 40 and 60 year, but deviate for the 80 year old model when compared qualitatively

to Jones (60) measured data. Additional clinical data is needed to further this optical

model. Future work should attempt to collect more data on lens curvatures. An index

model that has more gradient steps should also be investigated.
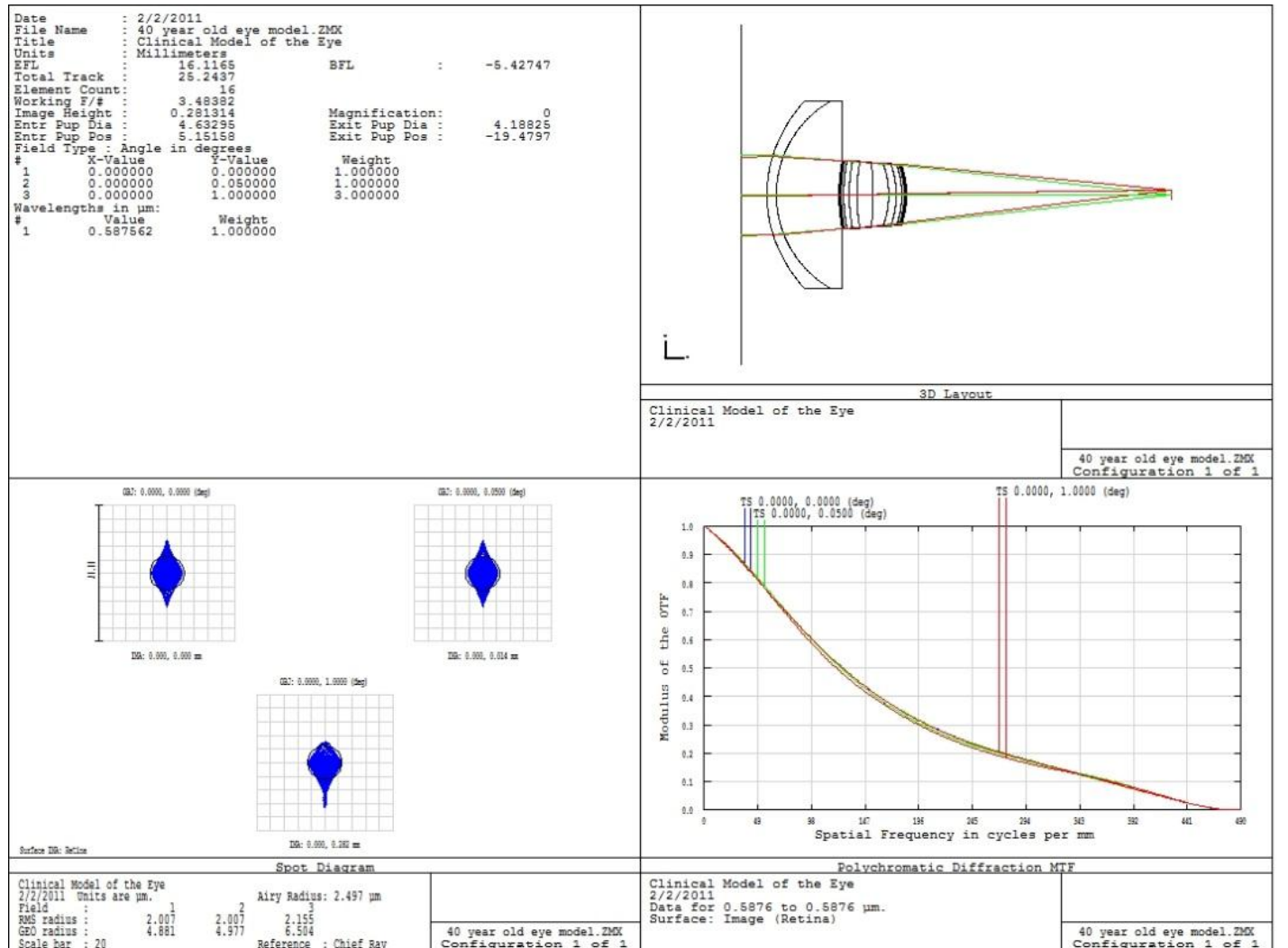
Figure 19 40 year old average Filipino Eye Models constructed using clinical data for Filipino patients.
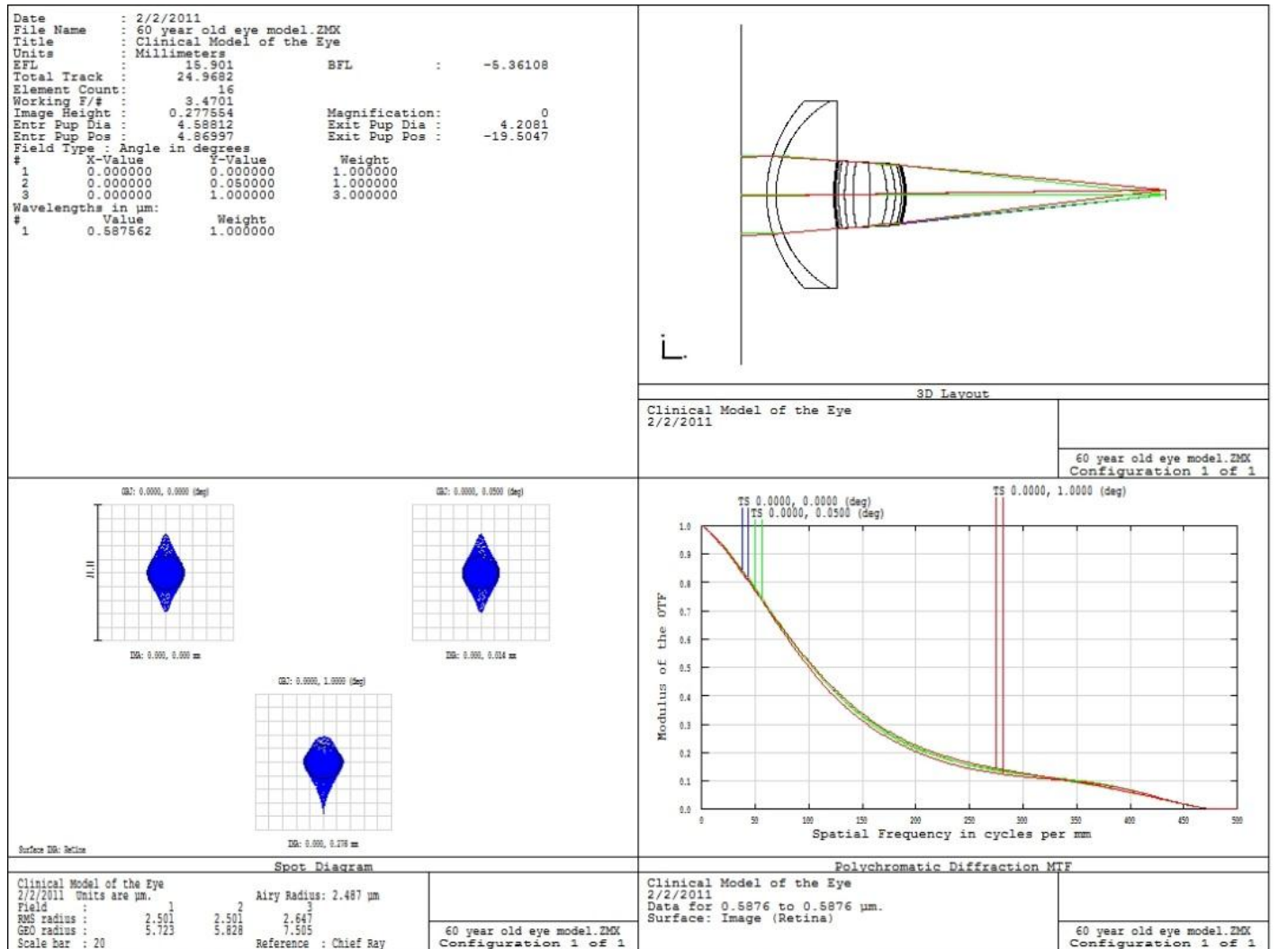
Figure 20 60 year old average Filipino Eye Models constructed using clinical data for Filipino patients.
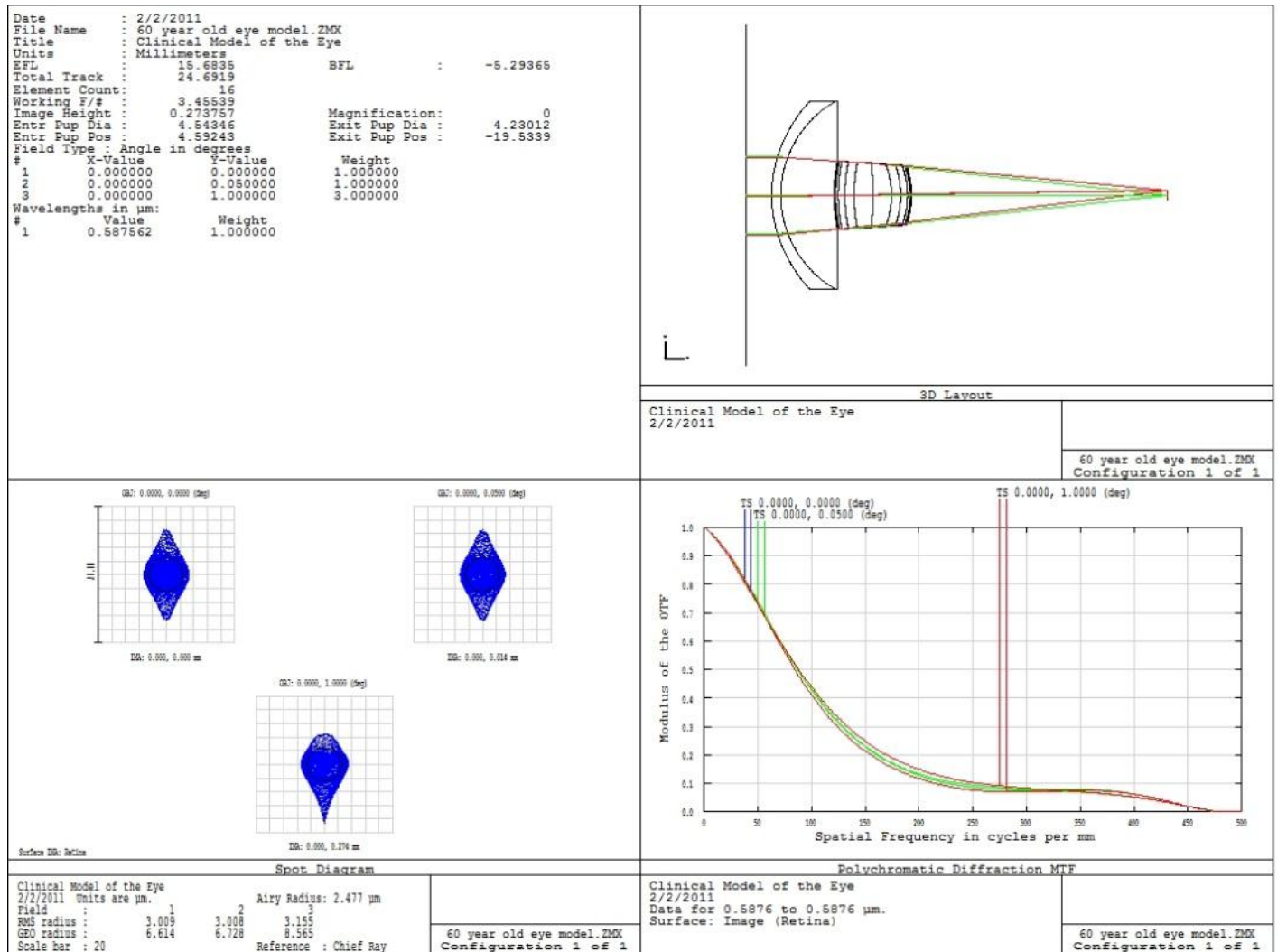
Figure 21 80 year old average Filipino Eye Models constructed using clinical data for Filipino patients.

2.8   Summary and Conclusions

The anatomy of the eye has been investigated using clinical data measured for a population of Filipino patients as a source of comparison for various aspects of the eye. Table 3 shows a summary of the clinical data collected for Filipino cornea, anterior chamber and lens thicknesses. This data has also been used to investigate how aging affects the performance of the average Filipino eye with age.

Table 3 Filipino Clinical Data Summary for the Cornea, Anterior Chamber, and Lens Thicknesses

Constituent	Ave (mm)	StDev (mm)	Max (mm)	Min (mm)
Cornea	0.54	0.04	0.64	0.45
Anterior Chamber	3.32	0.41	4.48	2.11
Lens	4.44	0.58	6.03	2.71

Disorders such as cataract have been described. As explained in Section 2.93 Standards of Care, the standard of care for treating cataracts is to surgically remove the fibrous mass and replace it with an IOL. This process presently requires the doctor to pierce the cornea, open the capsule by means of a capsulorhexis, and using phacoemulsification techniques to remove the fibrous mass. After the fibrous mass is removed, an IOL is inserted into the capsular sac. Lasers can help the doctor with this process by preprocessing the lens. This will reduce the complexity of the surgery. The first step for the laser processing of the lens is to process the capsule and perform a capsulotomy to allow the doctor access to the fibrous mass. A more thorough knowledge

of the laser physics at the anterior of the lens will help in bettering the standard of care for patients. This effort contributes to that knowledge based upon results obtained from experimentation.

CHAPTER 3 PULSED LIGTH INTERACTION WITH ORGANIC MATTER

iological matter breaks down when intensities reach 10^{10} to 10^{12} W/cm^2 (18). For a 10 pico-second laser this corresponds to an energy density, fluence, in the range of 0.1 J/cm^2 to 10 J/cm^2. Near infrared solid state short pulse lasers have low absorption in the eye which allows them to be focused deep into the eye. For these lasers to reach optical breakdown in the eye, nonlinear absorption must occur. High peak intensity of short pulse lasers can be absorbed in the eye by nonlinear absorption and optical break down can occur. Optical breakdown can be affected by self-focusing, self-phase modulation, and group velocity dispersion. Self-focusing can cause the beam to breakdown prior to the intended focus. Self-Phase Modulation and Group Velocity dispersion can cause the laser pulse to broaden reducing the peak intensity reducing the effectiveness of optical breakdown in the eye. When optical breakdown does occur, plasma is formed from the ionized electrons.   In this chapter, the requirements for optical breakdown are studied. Material effects due to intense laser fields are considered. Critical power is determined for a system with an F# of 4.2. A model is introduced that describes the rate at which the electron density increases as a function of the laser intensity. This model is used to look at threshold for a 100fs laser and 10ps laser with a wavelength of 1064nm. A thermal model is then used to study thermal effects and shock wave velocity of due to the laser pulse in water.

3.1   Effects of Intense Light in Media

The intensity of a short pulse laser can cause nonlinear effects in materials. A collimated beam can be focused due to the nonlinear index of refraction. This can cause the laser pulse to breakdown if the critical power is exceeded. Pulse broadening can also occur which reduces the peak intensity of the laser pulse reducing the effectiveness of the laser interaction. In the next sections, some fundamental results of intense pulse laser are studied.

3.1.1   Nonlinear Index of Refraction

Intense short pulse lasers can see effects of nonlinear index of refraction. By considering Maxwell's equations, an intensity dependent index of refraction can be derived. Equation 7, 8, 9, and 10 define Maxwell's equations. Equation 7 defines the divergence of the electric displacement, D, is equal to the free charge density, ρ. Equation 8 defines the divergence of the magnetic field, B, is equal to zero. Equation 9 defines the cross of the electric field, E, is equal to the time derivative of the magnetic field. Equation 10 defines cross of the auxiliary magnetic field, H, as equal to the time derivative of the electric displacement and the free current density, J. Equations 11 and 12 relate the auxiliary magnetic field and electric displacement in terms of the electric field; magnetic field; polarizability, P; magnization, M; permittivity of free space, ε_o and permeability of free space, μ_o. (100).

$$\nabla \cdot D = \rho \tag{7}$$

$$\nabla \cdot B = 0 \tag{8}$$

$$\nabla \times E = -\frac{\partial B}{\partial t} \tag{9}$$

$$\nabla \times H = -\frac{\partial D}{\partial t} + J \tag{10}$$

$$D = \varepsilon_o E + P \tag{11}$$

$$H = \frac{1}{\mu_o} B - M \tag{12}$$

By considering no charge variation in the material, no free current, and to magnetic properties in the material, the wave equation can be found by using

$$\nabla \times \nabla \times E + \frac{1}{c^2}\frac{\partial^2 E}{\partial t^2} = \frac{-1}{\varepsilon_o c^2}\frac{\partial^2 P}{\partial t^2}, \tag{13}$$

which can be further simplified using the vector identity

$$\nabla \times \nabla \times a = \nabla(\nabla \cdot a) - \nabla^2 a \tag{14}$$

to get

$$\nabla^2 E - \frac{1}{c^2}\frac{\partial^2 E}{\partial t^2} = \frac{1}{\varepsilon_o c^2}\frac{\partial^2 P}{\partial t^2}. \tag{15}$$

The polarizability, P, can be defined in terms of an electric field expansion,

$$P = \varepsilon_o\left(\tilde{\chi}^{(1)}E + \tilde{\chi}^{(2)}EE + \tilde{\chi}^{(3)}EEE\right), \tag{16}$$

where χ is the susceptibility.

In isotropic media on even terms of the polarizability exist; this reduces Equation

16 to

$$P = \varepsilon_o\left(\tilde{\chi}^{(1)}E + \tilde{\chi}^{(3)}EEE + \tilde{\chi}^{(2n+1)}E^{2n+1}\right). \tag{17}$$

The higher order terms of χ are many orders below $\chi^{(3)}$ so they can be ignored safely

(101). This result in equation 17 further simplifying to

$$P = \varepsilon_o\left(\tilde{\chi}^{(1)}E + \tilde{\chi}^{(3)}EEE\right), \tag{18}$$

that can be expressed as

$$P = \varepsilon_o\left(\tilde{\chi}^{(1)} + 3\tilde{\chi}^{(3)}|E|^2\right)E. \tag{19}$$

The $|E|^2$ term is related to the intensity of the incident light, by recalling that

$$I = \frac{|E|^2}{2\eta}, \tag{20}$$

where η is the impedance of free space and is equal to

$$\eta = \sqrt{\frac{\mu_o}{\varepsilon_o}}. \tag{21}$$

Equation 19 then becomes

$$P = \varepsilon_o\left(\tilde{\chi}^{(1)} + 3\tilde{\chi}^{(3)}2\eta I\right)E. \tag{22}$$

Substituting Equation 22 into Equation 15 the results yields

$$\nabla^2 E - \frac{1}{c^2}\frac{\partial^2 E}{\partial t^2} = \frac{1}{\varepsilon_o c^2}\frac{\partial^2 \varepsilon_o \left(\tilde{\chi}^{(1)} + 3\tilde{\chi}^{(3)} 2\eta I \right) E}{\partial t^2}. \tag{23}$$

This result can be re-expressed as

$$\nabla^2 E - \frac{1 + \tilde{\chi}^{(1)} + 3\tilde{\chi}^{(3)} 2\eta I}{c^2}\frac{\partial^2 E}{\partial t^2}. \tag{24}$$

The effective index of refraction of the material, $n_{eff,}$ can be defined as

$$n_{eff} = \sqrt{1 + \tilde{\chi}^{(1)} + 3\tilde{\chi}^{(3)} 2\eta I}. \tag{25}$$

Recalling that the index of refraction, n, is

$$n = \sqrt{1 + \tilde{\chi}^1}, \tag{26}$$

Equation 25 can be reexpressed as

$$n_{eff} = \sqrt{n^2 + 3\tilde{\chi}^{(3)} 2\eta I}, \tag{27}$$

which can be simplified to

$$n_{eff} = n\sqrt{1 + \frac{3\tilde{\chi}^{(3)} 2\eta I}{n^2}}. \tag{28}$$

This result reduces to

$$n_{eff} = n + \frac{3\tilde{\chi}^{(3)} \eta I}{n}, \tag{29}$$

by using the approximation

$$\sqrt{1 + a} = 1 + \frac{1}{2}a, where\ a \leq 1. \tag{30}$$

This second term in Equation 29 is considered to be the nonlinear index of refraction. Equation 29 is often expressed as

$$n_{eff} = n + n_2 I. \tag{31}$$

Some typical values of n_2 are given in Table 4.

Table 4 n_2 values for intensity dependent index of refraction for select materials (102)[1]

Material	Wavelength (nm)	$n_2(10^{-20} m^2/W)$
MaF$_2$	532	.67
	804	1.15 +/- 0.20
	1064	.835[1]
BK7	694	3.86
	804	3.75 +/- 0.30
	1064	3.515[1]
Distilled Water	532	4.75[1]
	804	5.7 +/- 0.5
	1064	3.45[1]
Benzene	580, 550	80
	804	24 +/-1
	1064	168

3.1.2   Self-Focusing

As a consequence of the intensity dependence in index of refraction of the material, the intensity field sees a gradient in the index of refraction with the central part of the beam seeing a higher index of refraction than the wings of the field. This gradient

---

[1] Multiple reported values of n_2 were averaged for given wavelength

in index leads to focusing of the laser beam in the media. As the beam focuses, it reaches a critical point where the self-focusing nature of the beam will equal the dispersive nature of the media. The critical power is defined as the power necessary in the beam such that the angle for total internal reflection equals the far field diffraction angle. The critical angle, θ_c, can be defined as (103)

$$cos(\theta_c) = \frac{1}{1 + \left(\frac{n_2 I}{n_o}\right)} \tag{32}$$

for small angles this can be re-expressed as

$$\theta_c = \sqrt{2\frac{n_2 I}{n_o}}. \tag{33}$$

Diffraction will cause the beam to expand as

$$\theta_D = \frac{1.22\lambda}{n_o D}. \tag{34}$$

Here λ is the wavelength of the incident light and D is the diameter of the beam. Setting $\theta_c = \theta_D$ and solving for D the following can be found:

$$D = \frac{1.22\lambda}{n_o}\left(\sqrt{2\frac{n_2 I}{n_o}}\right)^{-1}. \tag{35}$$

Recalling that the power, P, is

$$P = I\frac{\pi}{4}D^2 \qquad (36)$$

Substituting for D in equation 35, the critical power can be found to be (103)

$$P_{cr} = \frac{\pi(1.22)^2\lambda^2}{8n_o n_2} \qquad (37)$$

For a Gaussian beam, the critical power is slight different and can be expressed as

$$P_{cr} = \alpha\frac{\lambda^2}{4\pi n_o n_2} \qquad (38)$$

α is equal to 1.8962 for a Gaussian beam. For a 1064nm pulse in distilled water the critical power is 3.7MW. Some authors have reported lower values for the critical power, 2.4 +/- 1.2 MW for a 30ps pulse (104). For a Sech^2 beam the peak power of the laser can be expressed as

$$P = \frac{.88E_L}{\tau_L}. \qquad (39)$$

The laser pulse width and laser energy are τ_L and E_L respectively (105). To exceed the critical power for a 10ps, 1064nm laser the laser fluence must be greater than 34.55 J/cm^2 in distilled water for an F/4.2 optical system. If the power goes above

$$P_c = 3.7P_{cr} \qquad (40)$$

the beam will breakdown and collapse (106).

3.1.3 Self -Phase Modulation

The intensity dependent index of refraction also can cause temporal changes in the pulse. Considering a Gaussian pulse with a temporal profile of

$$I(t) = I_0 e^{-2at^2}, \tag{41}$$

the phase shift for this pulse going a length, L, in a nonlinear medium can be calculated to be (103)

$$\phi(t) = \frac{2\pi(n_0 + n_{2I}I(t))L}{\lambda}. \tag{42}$$

From this the phase velocity can be calculated by taking the derivative of Equation 42. The result of this is

$$\frac{\partial\phi(t)}{\partial t} = \frac{2\pi n_{2I}L}{\lambda}\frac{\partial I(t)}{\partial t} = \frac{-4a\pi n_{2I}L}{\lambda}I_0 t e^{-2at^2}. \tag{43}$$

Equation 43 indicates that the pulse will increase in temporal length when passing through this media. As the intensity increases the phase front will be delayed, causing a shift to longer wavelengths. As the phase front goes negative for the latter part of the pulse, the pulse will be shifted towards the blue. The result of this is the pulse gets temporally longer.

3.1.4 Group Velocity Dispersion

When broad spectrum light passes through an optically transparent material, each of the wavelengths making up the wave packet travels at a slightly different speed than the other wavelengths. In the case of typical glasses, the red portion of the spectral band

51

moves ahead of the blue bands of the spectrum resulting in a broadening of the pulse temporally. This temporal broadening of the pulse can lead to dramatic effects on the laser pulse. Typically, for convention optical material for each cm of glass that a 100fs laser goes through the pulse width increases by approximately a $\sqrt{2}$ temporally. Depending on the amount of material the laser pulse is going through, the temporal nature of the laser pulse can be affected due to the material interaction.

3.2   Rate Equation for Organic Matter Breakdown

To support a plasma and cause organic matter breakdown, the free electron density must increase to approximately 10^{21}cm^{-3} for a 1064nm laser source (107) (106). To reach these densities in low absorption materials, the laser intensity needs to exceed a threshold value to allow for sufficient excitation of electrons in the media. The initial electron excitation forms by multi-photon excitation. This provides a seed electron for avalanche excitation. The multi-photon absorption is related to the intensity of the source, I, by I^k where k is the number of photons necessary to excite an electron through the band gap. In water, the band gap energy is approximately 6.5eV when considering the water as an amorphous semiconductor (19). For a laser with a central wavelength at 1064nm, this corresponds to 6 photons summing together to be able to raise one electron to the ionization energy. Once the first seed electron is excited, it is accelerated through inverse Bremsstrahlung absorption. The electron gains energy until it is able to free a second electron from another atom. This process continues to increase the population of electrons through a cascading or avalanche effect. These two population increasing

processes are countered by diffusion of electrons out of the focal volume and the recombination of electrons.

To describe the rate of change in the electron density from these processes, a rate equation which incorporates the various components of the organic matter breakdown process can be expressed as, (104),

$$\frac{\mathrm{d}n_e}{\mathrm{d}t} = \left(\frac{\mathrm{d}n_e}{\mathrm{d}t}\right)_{\mathrm{mp}} + \eta_{\mathrm{Aval}}n_e - gn_e - \eta_{\mathrm{rec}}n_e^2 \tag{44}$$

The first term on the left describes the increase in the total density of the electrons due to all the processes. The first term on the right , $\left(\frac{\mathrm{d}n_e}{\mathrm{d}t}\right)_{\mathrm{mp}}$, corresponds to the generation of electrons due to multi-photon ionization. The second term in equation 44, $\eta_{\mathrm{Aval}}\,n_e$, describes the generation of electrons due to avalanche or cascade ionization of electrons. The third term, gn_e, the first loss term, is due to the diffusion of electrons out of the focal volume. The fourth term, $\eta_{\mathrm{rec}}n_e^2$, is the recombination rate term where η_{rec} is the rate at which electrons recombine reducing the total density of free electrons. Several authors ignored the multi-photon term (7), (108), (109), which may be acceptable for long pulses where avalanche ionization dominates the ablation process. In short, pulse lasers multiphoton ionization play a significant role in the ionization of electrons. Calculating the electron density for short pulse lasers and not considering the multiphoton term results in larger errors in population density estimation (107).

In the next sections, a description of each of the constituents making up equation 44 is presented.

3.2.1 Multi-photon Ionization $\left(\frac{dn_e}{dt}\right)_{mp}$

     Keldysh derived expressions for the probability of multi-photon ionization of both gases and condensed media (110). In condensed media, the process of ionization generates an electron hole pair. The electron transitions from the valance band to the conduction band of the material during the ionization process. In the case of in incident monochromatic field the transition can occur if photons can stack freeing an electron. To be able to free an electron from an atom, k photons are needed where

$$k = \langle\frac{\Delta E'}{\hbar\omega_0} + 1\rangle$$
(45)

$\langle\frac{\Delta E'}{\hbar\omega_0} + 1\rangle$ denotes the quanta of photons necessary to free the electron from the atom, ω_0 is the laser frequency and $\Delta E'$ is the effective ionization potential, and $\hbar$ is Plank's constant. The effective ionization potential can be expressed as

$$\Delta E' = \Delta E\left(1 + \frac{1}{4\gamma^2}\right)$$
(46)

ΔE is the ionization energy of the material. The term γ is defined here as the Keldysh coefficient. It corresponds to the ratio of the optical field frequency to the tunneling frequency and can be expressed as

$$\gamma = \frac{\omega_0}{\omega_t} = \omega_0\frac{(m'\Delta E)^{1/2}}{eE}$$
(47)

where m' is the reduced mass of the electron and hole expressed as

$$\frac{1}{m'} = \frac{1}{m_e} + \frac{1}{m_h},$$ (48)

e is the electron charge, and E is the incident electric field.

In the case of multi-photon absorption for laser fluence levels near threshold for laser pulses down to 100fs, γ is very large. This results in $\Delta E'$ being roughly equal to ΔE. Using this fact, the Keldysh expression for the probability of multi-photon absorption can be calculated to be

$$\left(\frac{dn_e}{dt}\right)_{mp}$$

$$\approx \frac{2\omega_0}{9\pi}\left(\frac{m'\,\omega_0}{\hbar}\right)^{3/2}\left[\frac{1}{16\,\gamma^2}\right]^k e^{2k}\Phi\left(\sqrt{2k - \frac{2\Delta E}{\hbar\omega_0}}\right).$$ (49)

This can be re-expressed as (107) (110)

$$\left(\frac{dn_e}{dt}\right)_{mp}$$

$$\approx \frac{2\omega_0}{9\pi}\left(\frac{m'\omega_0}{\hbar}\right)^{3/2}\left[\frac{e^2}{16m'\Delta E\omega_0{}^2 c\epsilon_0 n}I\right]^k e^{2k}\Phi\left(\sqrt{2k - \frac{2\Delta E}{\hbar\omega_0}}\right).$$ (50)

by using the relation

$$\frac{1}{\gamma^2} = \frac{e^2}{m'\Delta E\omega_0{}^2 c\epsilon_0 n}I.$$ (51)

In equation 50 the term, $\Phi(x)$, corresponds to the Dawson integral:

$$\Phi(x) = e^{-x^2} \int_0^x e^{y^2} dy. \tag{52}$$

3.2.2 Avalanche Ionization η_{Aval}

Once a seed electron is ionized in the tissue, the process known as inverse Bremsstrahlung takes place as the electron interacts with the atom in presence of the electric field. The electron gains energy during this interaction. This gain in energy can be described by considering the mean energy of an electron in an electric field of the laser, $\frac{e^2 E^2}{2m_e \omega_o^2}$. Typically the electron will only oscillate in the field, but when the electron encounters an atom it causes the electron motion to abruptly change. During this process, a finite amount of the incident electric field is coupled into the electron motion. The finite amount of energy that is coupled into the electron can be found to be (111):

$$\frac{\partial \epsilon}{\partial t} = \frac{e^2 E^2}{2m_e \omega_o^2} \nu_{eff} \frac{\omega_o^2}{\omega_o^2 + \nu_{eff}^2}. \tag{53}$$

In equation 53, ν_{eff} is mean collision frequency which is equal to $n_a v_e \sigma_{tr}$, where n_a is the atomic density, v_e is the electron velocity, and σ_{tr} is the electron transport cross-section. Considering in cases where the electron does not gain energy, but instead loses energy due to the interaction with the atom, then the loss in energy is

$$\frac{\partial \epsilon}{\partial t} = \frac{-2m_e \epsilon_{av}}{M} \nu_{eff} \frac{\omega_o^2}{\omega_o^2 + \nu_{eff}^2}. \tag{54}$$

In equation 54, m_e is the mass of the electron and ε_{av} is the average energy of the electron. Combining equation 53 and equation 54, the average energy rate can be described as

$$\frac{\partial \epsilon}{\partial t} = \left(\frac{e^2 E^2}{2m_e \omega_o{}^2} - \frac{2m_e \epsilon_{av}}{M} \right) \nu_{eff} \frac{\omega_o{}^2}{\omega_o{}^2 + \nu_{eff}{}^{2.}}. \tag{55}$$

If instead of expressing equation 55 in terms of the mean collision frequency, ν_{eff}, equation 55 can be re-expressed in terms of the mean collision time, τ, as

$$\frac{\partial \epsilon}{\partial t} = \left(\frac{e^2 E^2}{2m_e \omega_o{}^2} - \frac{2m_e \epsilon_{av}}{M} \right) \frac{\tau \omega_o{}^2}{\tau^2 \omega_o{}^2 + 1}. \tag{56}$$

Equation 56 expresses the rate that the energy of the electron in the presence of an electric field changes. If equation 56 is divided by the ionization energy it will describe the rate at which electrons gain enough energy to ionize another electron. Considering this, equation 56 can be modified to

$$\eta_{Aval} = \left(\frac{e^2 E^2}{2m\omega_o{}^2} - \frac{2m\epsilon_{av}}{M} \right) \frac{\tau \omega_o{}^2}{\tau^2 \omega_o{}^2 + 1} \frac{1}{E_{ion}}. \tag{57}$$

Recalling that $E^2 = I/cn\varepsilon_o$, equation 57 can be re-expressed in terms of intensity as (107)

$$\eta_{Aval} = \left(\frac{e^2 I}{2m\omega_o{}^2 cn\varepsilon_o} - \frac{2m\epsilon_{av}}{M} \right) \frac{\tau \omega_o{}^2}{\tau^2 \omega_o{}^2 + 1} \frac{1}{E_{ion}}. \tag{58}$$

Given that only electrons with ionization energy E_{ion} are being considered the average energy of the electrons, ϵ_{av} is E_{ion}, which allows equation 58 to be expressed as (104)

$$\eta_{Aval} = \frac{\tau}{\omega_o \tau^2 + 1} \left[\frac{e^2}{cn\epsilon_o m\Delta E} I - \frac{m\omega_o{}^2}{M} \right].$$ (59)

3.2.3 Diffusion and Recombination $gn_e + \eta_{rec}n_e{}^2$

The first loss terms, gn_e, in equation 44 represents the diffusion and trapping of electrons and the second term $\eta_{rec}n_e{}^2$ represents the loss terms due to recombination. The trapping levels of water are ~1.5 +/-0.5eV (107). These energies are low enough that any avalanche ionization would quickly re-ionize the electrons in these states. Diffusion then is the dominate factor in the loss rate, g. Diffusion out of the focal volume can be described by

$$g = \frac{D}{\Lambda^2}.$$ (60)

Here D is the electron diffusion coefficient and Λ is the characteristic diffusion length. The diffusion coefficient can be described by

$$D = \frac{2\epsilon_{av}}{3m_e v}.$$ (61)

The diffusion length, Λ, is a cylindrical volume defined by the beam waist and the Rayleigh length of the beam. The diffusion length is

$$\Lambda = \sqrt{\frac{1}{\left(\frac{4.8}{2\omega_0}\right)^2 + \left(\frac{1}{z_r}\right)^2}}$$ (62)

Taking the definition for diffusion length and electron diffusion coefficient the loss due to electron diffusion can be expressed as (104):

$$g = \frac{\tau \Delta E}{3m_e} \left[\left(\frac{2.4}{\omega_0} \right)^2 + \left(\frac{1}{z_r} \right)^2 \right].$$
(63)

In Noack and Vogel's paper (104), they report that the recombination rate was found empirically by Docchio to be

$$\eta_{rec} = 2x10^{-9} \frac{cm^3}{s}.$$
(64)

3.2.4 Initial Population

The development of the electron density in media depends on the state of the initial population. As mentioned previously, avalanche ionization starts when a free electron is in the media. This initial free electron density comes from the ionized molecules, impurities or the ionization of carriers in shallow traps. Two ionization methods are optical absorption and thermal excitation. Thermal excitation can come from phonons in structured media or molecule-molecule collisions in liquids. The initial free carrier density can be defined by (107),

$$\rho_o = \rho_{ot} + \rho_{om},$$
(65)

where ρ_{ot} is the part of the population generated from thermal excitation and ρ_{om} is the part of the population generated from multi-photon excitation. The description of multi-photon ionization was presented in 3.2.1 and will not be presented again here.

The free carrier density due to thermal excitation can be described by a Maxwell-Boltzmann distribution with temperature, T. The distribution of interest to the ablation process is the distribution relative to the ionization energy, E_{ion}. This can be expressed as

$$P = e^{-(E_{ion}/k_B T)},$$ (66)

where k_B is Boltzmann constant. Considering P as a strict probability, it can be converted to a population by multiplying the density of the bound electrons in the media (107),

$$\rho_{ot} = \rho_b P$$ (67)

Equation 67 represents the electron density that is present in the volume due to thermal excitation.

3.2.5 Modeling results for Electron Population Evolution

Considering the above conditions, a model can be calculated to examine the effects of pulse duration on the evolution of the electrons density. In Figure 22 (a) and (b) presents two threshold conditions of the electron density for a 100 fs and a 10 ps laser pulse. The red line is the evolution of the total population density and the blue line is the evolution of the multi-photon electron density. In both cases, the ionization of electrons is dominated by avalanche ionization. The experimental work of this thesis uses a 10 ps laser system. The avalanche ionization contributes more to the 10ps than the 100 fs pulse because of the 10 ps has more time for avalanche ionization to occur.
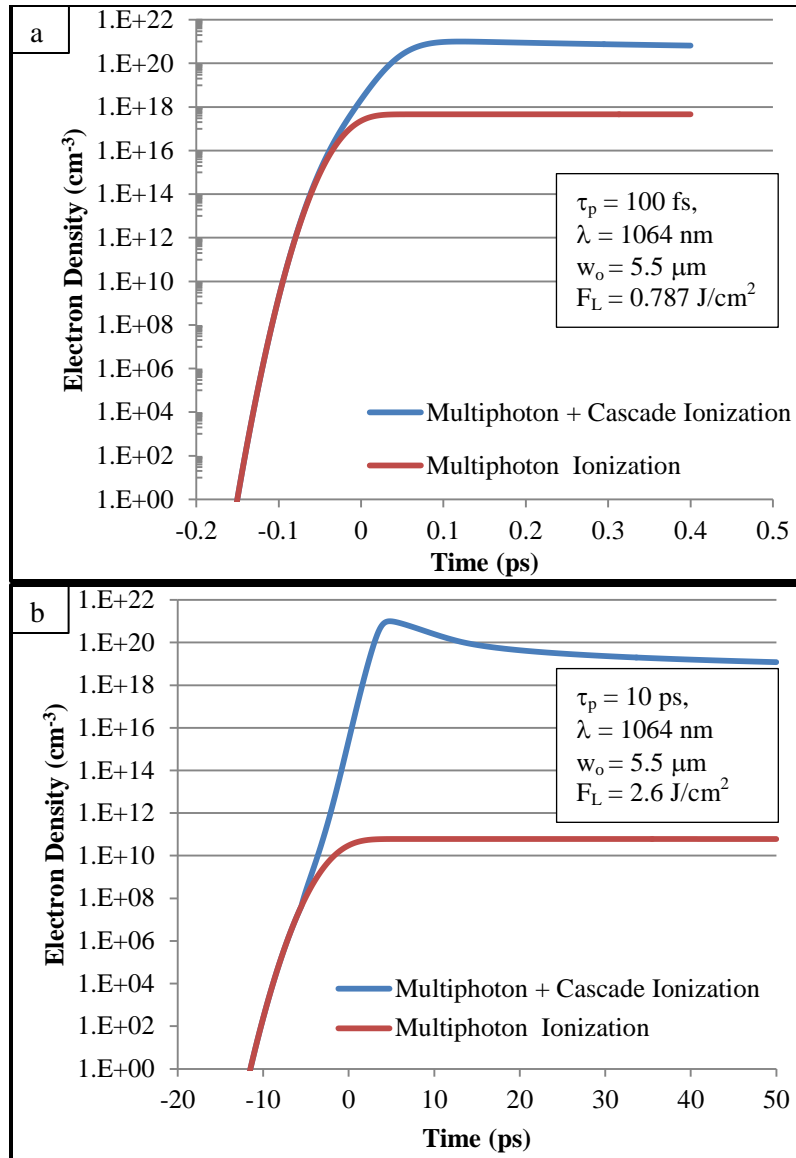
Figure 22 Evolution of electron density at focus for (a) 100fs pulse and (b) 10ps at threshold fluence.

3.3   Electron Distribution

Although the radial intensity distribution can be found by using Fraunhofer

diffraction, it can be approximated by using an ellipsoid of radial dimension, a, and axial

length, b, where a and b denote the $1/e^2$ values of the Gaussian irradiance pattern in each

axis (112). The functional form of this is

$$I(r, z) = I_o \exp\left\{-2\left(\frac{r^2}{a^2} + \frac{z^2}{b^2}\right)\right\}. \tag{68}$$

I_o corresponds to the peak intensity of the field, r is the radial dimension from the axis

and z is the axial dimension of the intensity. For an ultra-fast laser pulse where multi-

photon absorption is the dominant form of absorption the electron density goes as the

intensity to the power of the quanta number of photons necessary to for multi-photon

absorption. This approximation neglects the weaker dependence of avalanche ionization

that would be seen in the latter half of the temporal pulse. Avalanche ionization would

broaden the field distribution of the electrons as in the case of a 10ps pulse. Multiphoton

ionization results the electron density forming the plasma being more confined in the

central portion of the beam. The electron density can then be expressed as

$$\rho(r, z) = \rho_o \exp\left\{-2k\left(\frac{r^2}{a^2} + \frac{z^2}{b^2}\right)\right\}, \tag{69}$$

where ρ_o is the peak density on axis with the peak intensity I_o, k is the quanta of photons

necessary to excite one electron. The major and minor axis of the ellipse, a and b,

correspond to the $1/e^2$ radial extents of the incident field intensity. From equation 67 it is

seen that the electron density is reduced by a factor $\sqrt{k}$ when compared to the distribution

of the intensity. This means that as the wavelength of the incident beam gets shorter, the

reduction in spot size will not correlate linearly to the electron density linearly. Instead

the electron density will increase as the $\sqrt{k}$. This has direct effects when considering

tissue processing with the plasma. The spot to spot separation to cut tissue will be less

than the spot laser spot size. For an F4.2 lens this means that the electron density would

be approximately 4.5 μm when focused in water at 1064nm. For the 10 ps laser pulse

though, the avalanche ionization broadens the electron density. As fluence levels are increased the electrons density would be expected to approach the size of the focal spot.

3.4　Temperature Rise in Tissue

When the laser energy is deposited in the media it generates excited electrons. These electrons can be further accelerated by the incident radiation and interact with the environment around them by either reaching energies that allow them to excite other electrons or interact with other molecules in the media. Interaction with molecules can result in collisional energy transfer or non-radiative recombination. These processes result in the heating of atomic, molecular, and plasma constitutes. To determine the equilibrium temperature, the characteristic time for electron cooling and recombination rate in which electrons rehydrate in the media need to be considered. The time constant for electron cooling is a few picoseconds and the hydration of free electrons in water about 300 fs. Hydration states lifetimes are much longer being approximately of 300ns. These processes are modeled in the previous defined model of Section 3.2 as the recombination term. In the model previously described, the recombination of electrons goes as the electron density squared. This results in it taking between a couple of picoseconds and tens of picoseconds until a thermodynamic equilibrium is reached (112).

The temperature rise can be calculated by determining the volumetric energy density gained during the laser pulse. For the 10 ps laser pulse interaction time is short enough that the energy during the interaction can be considered to only go into the interaction volume. The energy density for the interaction volume goes as the total electron density multiplied by the mean electron energy. The mean electron density is

calculated by summing the ionization energy and the average kinetic energy of the electrons. The average kinetic energy of the electrons is $(5/4)\Delta$ where Δ is the ionization energy for an electron. Using this, the plasma energy density can be calculated by (112)

$$\varepsilon = \rho_{max}\left(\frac{9}{4}\right)\Delta.$$

(70)

This approximation of the electron energy density does not consider the changes in the energy due to impact ionization that may result in a slight under estimation of the energy of one electron. It treats the energy produced by electrons that are produced by multi-photon ionization the same as electrons that are produced by collisional ionization that results in an overestimation of the energy density. Using equation 68, the temperature rise due to one pulse for the laser is

$$\Delta T = \frac{\varepsilon}{\rho_0 C_p}.$$

(71)

Here ρ_o is the density of the media and C_p is the heat capacity of the media.

The temperature evolution in and around the interaction volume can be calculated by solving the heat diffusion equation with the appropriate Green's function with an appropriate source. In equation 72, the laser is treated as a Gaussian heat source (112).

$$Q(x,y,z) = \frac{A}{\rho_0 C_p} \exp\left\{ -2\left(\frac{x'^2 + y'^2}{a^2}\right) - \frac{2z'^2}{b^2} \right\}$$

(72)

A is the peak density of absorbed power the irradiated volume, ρ_o is the density of the media, C_p is the heat capacity, a and b are the short and long half-axes of the beam for the 10ps laser. The density and heat capacity of water are 1000 kg m^{-3} and 4187 J K^{-1}kg^{-1}

respectively. Inserting this heat source into the appropriate Green's function for a source in an infinite space the temperature in space can be expressed as (113):

$$
\begin{aligned}
&T(x, y, z, t) \\
&= \int_0^{\min(t,\tau_L)} \frac{A}{\rho_o C_p \left(4\pi\kappa(t - t')\right)^{3/2}} \int \int_{-\infty}^{\infty} \int \exp\left\{-2\left(\frac{x'^2 + y'^2}{a^2}\right)\right. \\
&\left. -\frac{2z'^2}{b^2}\right\} \times \exp\left(\frac{-[(x - x')^2 + (y - y')^2 + (z - z')^2]}{4\kappa(t - t')}\right) dx'dy'dz'dt'
\end{aligned}
$$
(73)

κ is the heat diffusivity with a value of $1.38\times10^{-7}\mathrm{m^2s^{-1}}$. The integration value $\min(t,\tau_L)$ refers to the integrand being integrated to t or τ_L whichever is lower, and τ_L is the laser pulse width.

Solving equation 73, the temperature distribution can be found to be

$$
\begin{aligned}
&T(x, y, z, t) \\
&= \int_0^{\min(t-\frac{n}{f},\tau_L)} \frac{A}{\rho_o C_p} \frac{\pi a^2}{8\kappa(t - t') + a^2} \sqrt{\frac{\pi b^2}{8\kappa(t - t') + b^2}} * \\
&\qquad exp\left\{-2\left(\frac{x'^2 + y'^2}{8\kappa(t - t') + a^2}\right) - \frac{2z'^2}{8\kappa(t - t') + b^2}\right\} dt'
\end{aligned}
$$
(74)

Figure 23 through Figure 26 show the thermal effects of one pulse being focused into water for several fluence levels of interest for the 10 ps laser. These plots show both the spatial extent and the temporal effect of the laser interaction. In all cases the temperature rise drops to 1/100 of a degree in about a μs. For frequency that less than 500 kHz, the temperature of the water would be expected to return to within 0.01 of its starting temperature.
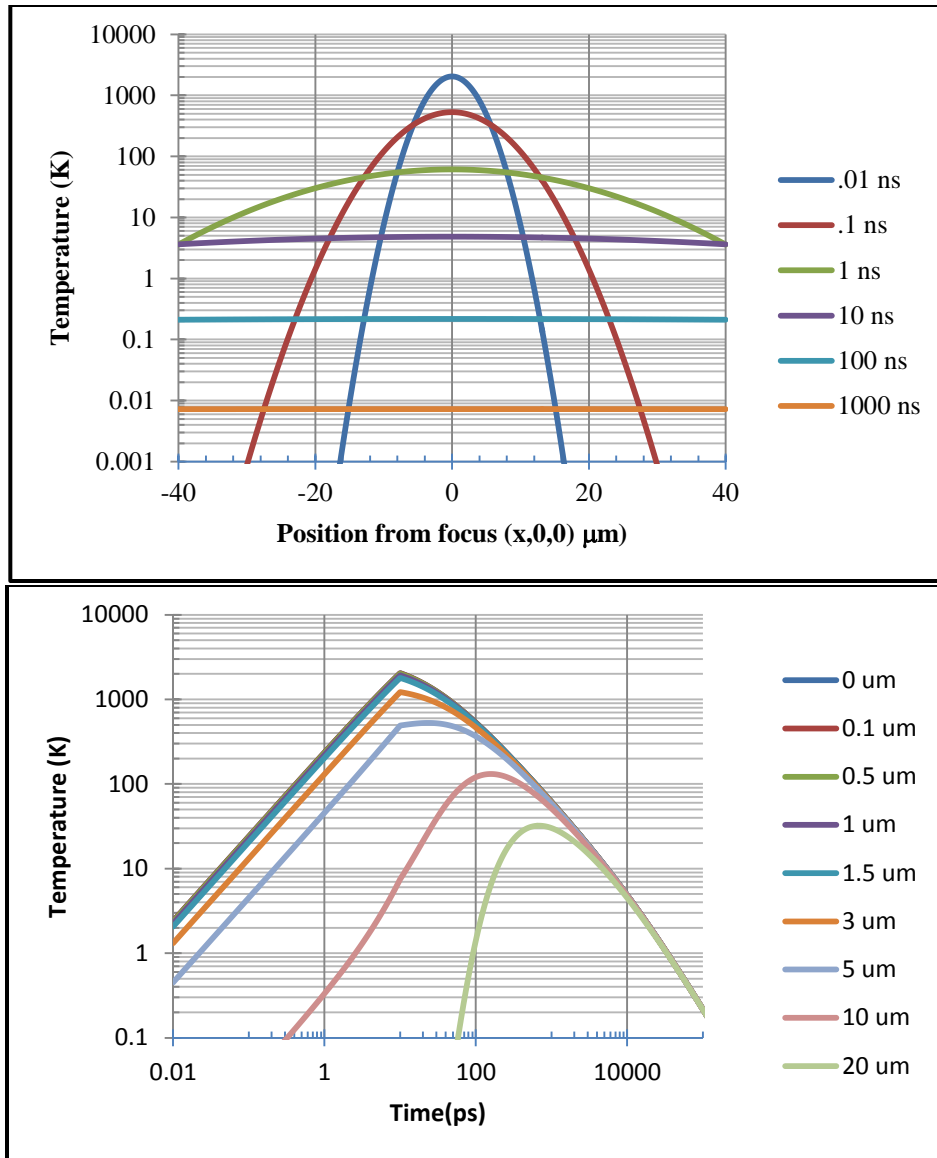
Figure 23   (a) Temperature spatial distribution for a 10ps, 25.34 J/cm^2 pulse in an F/4.2 system at different times (b) Temperature evolution for different radial positions over time.
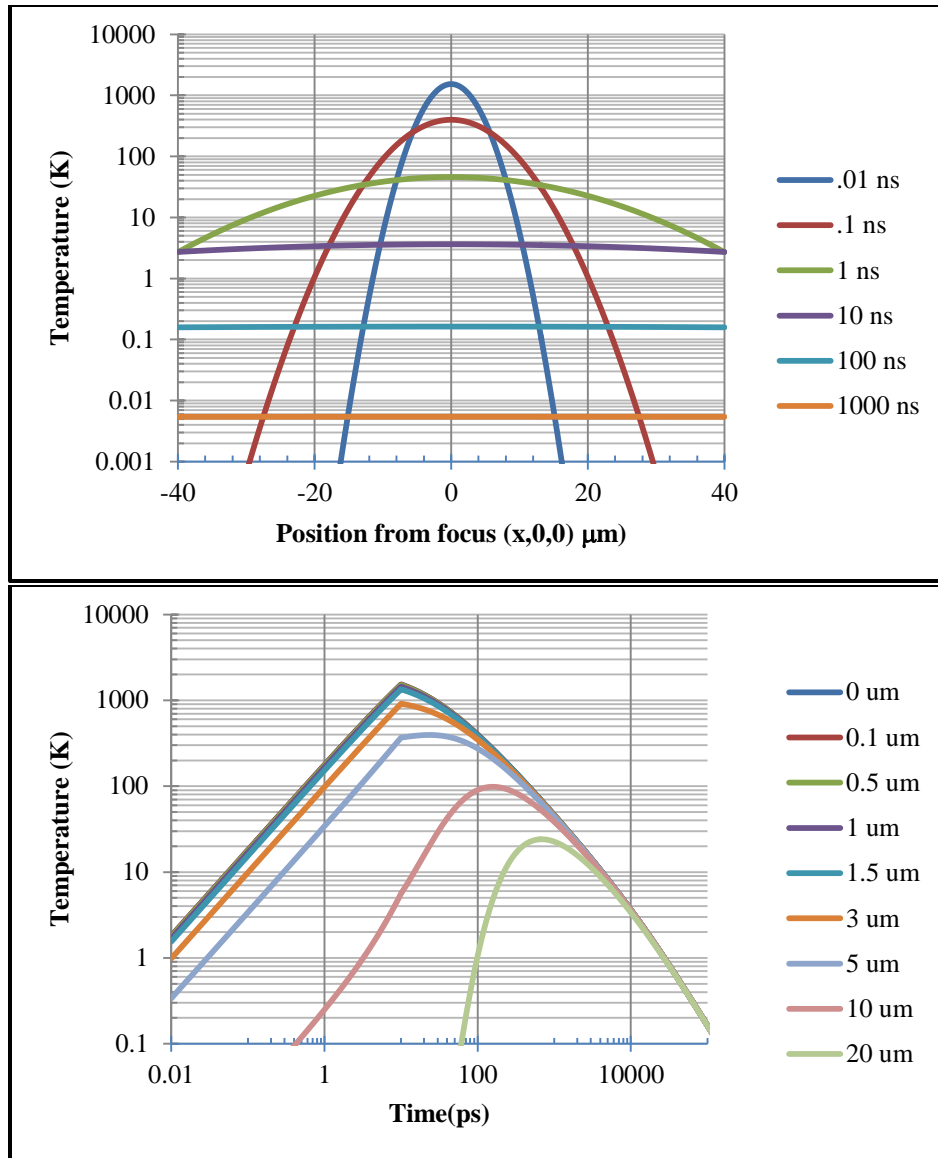
Figure 24 (a) Temperature spatial distribution for a 10ps, 19.01 J/cm^2 pulse in an F/4.2 system at different time (b) Temperature evolution for different radial positions over time.
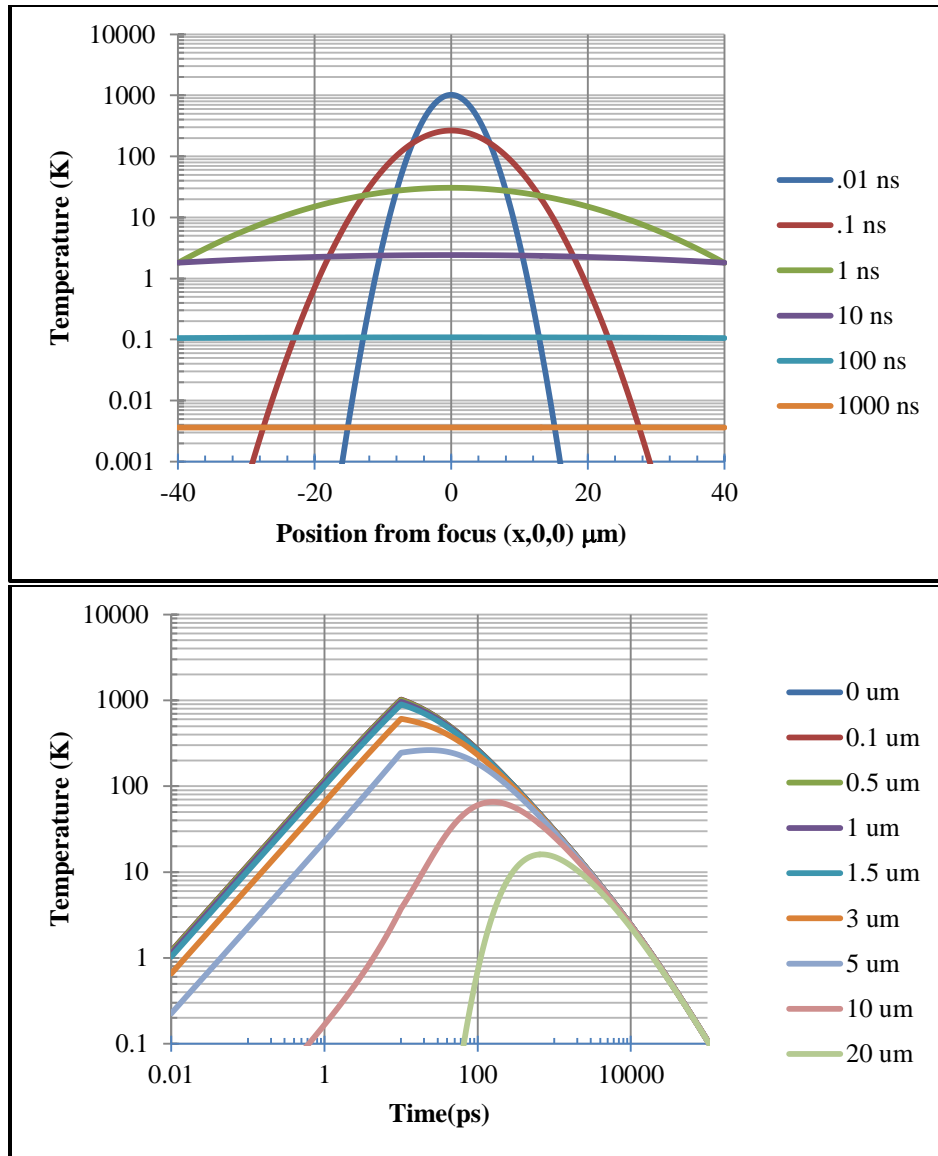
Figure 25(a) Temperature spatial distribution for a 10ps, 12.67 J/cm^2 pulse in an F/4.2 system at different time (b) Temperature evolution for different radial positions over time.
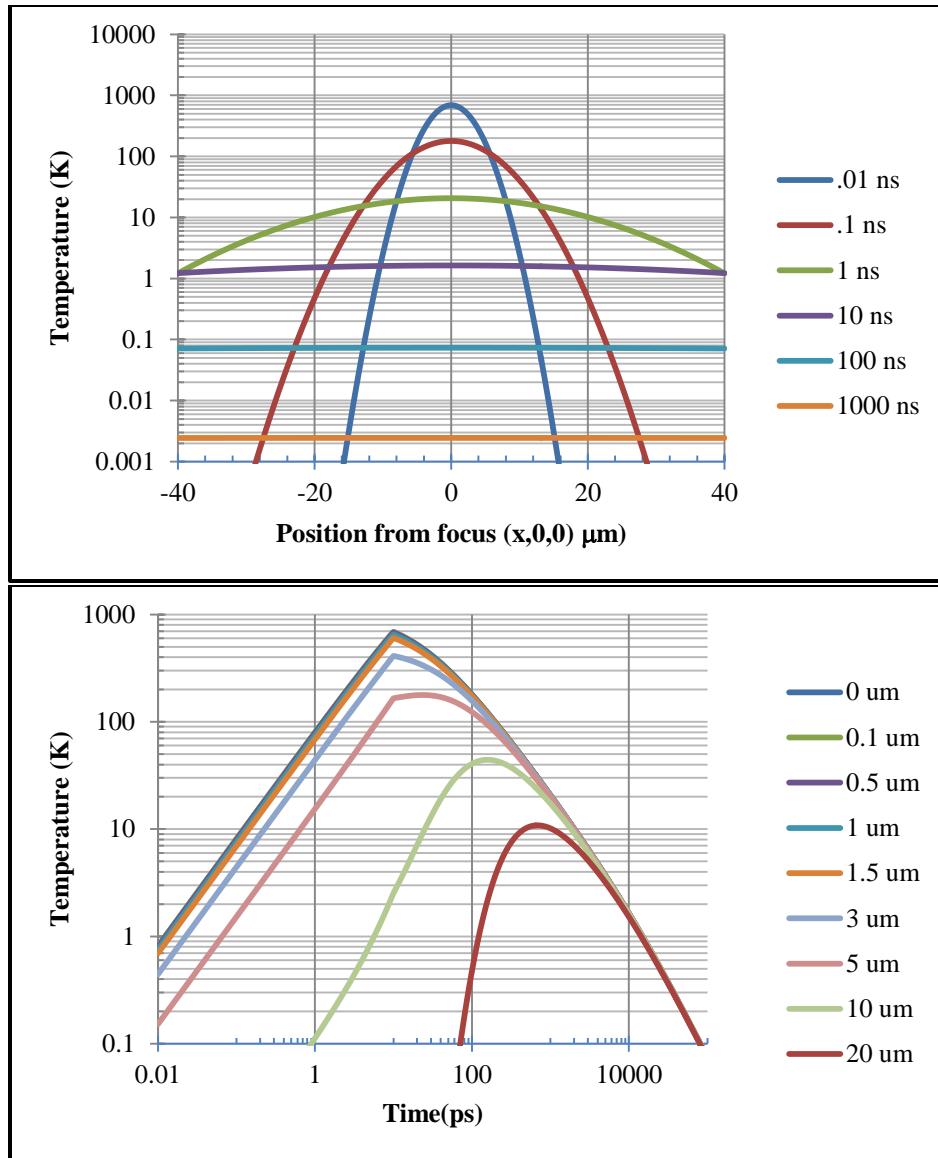
Figure 26 (a) Temperature spatial distribution for a 10ps, 8.55 J/cm^2 pulse at different time (b) Temperature evolution for different radial positions over time.

3.5   Shock Wave and Pressure

When an ultrafast laser is focused into tissue with fluence above threshold it is

causes photodisruption. During the process of plasma generation the tissue is heated.

The heat generated can be associated with the kinetic energy of the electrons in the

plasma. Due to their high kinetic energy the electrons are not limited to the focal volume.

They diffuse to the surrounding material. The electron interaction with the surrounding inert ions results in mass being moved and a shock wave. The mean kinetic energy of the particles can be calculated by using Equation 71. From the mean kinetic energy the particle velocity can be determined to be

$$v_p = \sqrt{\frac{2\varepsilon}{\rho_0}}. \tag{75}$$

The shock wave velocity can be equal to (114)

$$v_s = A + Bv_p. \tag{76}$$

A is the speed of sound in the material. B is a numerical constant. In water, B is equal to 2.08.

Knowing the shock was velocity, v_s, and the particle velocity, v_p, the pressure can be determined from the photodisruption as

$$P - P_o = \rho_0 v_p v_s. \tag{77}$$

P_o is the hydrostatic pressure.

3.6   Summary and Conclusion

Short pulse lasers can affect materials nonlinearly because of the peak intensities of the laser pulse. If the pulse exceeds the self-focusing threshold, the photodisruption can be affected. For an F/4.2 10ps laser system, it was found that the laser fluence that results in self-focusing of the laser pulse is 34.55 J/cm^2 in water. This sets an upper limit

to the maximum fluence that can be focused in the eye and not have self-focusing due to the laser power occur.

The rate equation for organic matter breakdown was found to be:

$$\frac{dn_e}{dt} = \left(\frac{dn_e}{dt}\right)_{mp} + \eta_{Aval}n_e - gn_e - \eta_{rec}n_e. \qquad (44)$$

Each of the components that make up this rate equation has been defined. It was determined from this rate equation that for a 10ps pulse that avalanche ionization plays a large role in developing the electron density near threshold.

The temperature effects of a 10ps pulse were also investigated. It was determined that a 25.34 J/cm^2 causes a local rise of 2000K for 10ps pulse in an F/4.2 system. Even when the laser fluence is reduced to 8.55 J/cm^2 there is still a rise of several hundred Kevin in the material near the laser pulse. This may cause residual side effects if the laser pulse is focused into fixed media. The heating of the material results in a shock wave that emanates from the photodisruption. The shock wave initially travels at hypersonic speeds, but over time will slow to the speed of sound in the material.

In this chapter, the effects of laser intensity have been considered from the standpoint of self-focusing, pulse dispersion, ionization, and rise in temperature of material due to the laser pulse. Self-focusing limits have been found. The electron density has also been considered. It was found that the avalanche ionization plays a large role in ionization for a 10ps laser pulse. Finally, it was determined that the laser pulse at the edge of the electron density raised the temperature of tissue significantly for a short

period of time. If the pulse is placed in the lens and the fibrous mass of the lens is not

removed, remnants of the laser pulse may be observable over time.

CHAPTER 4 MODEL OF PLASMA FORMATION

In chapter 3, the components of the plasma physics that describe the growth of the electron population over time was introduced. The threshold population that was necessary for the generation of plasma was defined to be approximately 10^{21} electrons/cm^3 for a 1064nm laser. For a 10ps laser source this electron density is reached by a combination of both multiphoton ionization and avalanche ionization. In this chapter, this theory is applied by considering the evolution of the electron density near and at the boundary between the crystalline lens and anterior chamber for a fluence level three times the threshold fluence level necessary to achieve plasma formation. Several cases are considered using these conditions. The first case considered is the laser focused deep in the fibrous mass of the lens. This represents the uniform media model. The second case is focus is at and the capsule. Cases 3 through 5 position focus to consider how the capsule is affected by plasma formation. Before making these calculations, the simplification used in chapter 3 where the Keldysh coefficient was assumed to be large is examined for laser powers greater than threshold.

4.1   Photodisruption in a volume

Threshold fluence level for a 10ps laser forms plasma at focus. Fluence levels above threshold cause a column of plasma to form. This leads to a region where there is optical breakdown and a region that remains unaffected by the incident light as illustrated in Figure 27. The optical breakdown region starts at focus and grows to the point where

the electron density can no longer support plasma. The rate equation for organic matter breakdown, Equation 44, can be used to model the plasma formation. One approximation made in Chapter 3 was that the Keldysh coefficient was large in Equation 46. This may lead to a large overestimation of the electron population. If the Keldysh coefficient is small for different laser intensities of interest, it may need to be considered in the calculation of the population density. To determine if this approximation is acceptable, the ionization density using the Keldysh coefficient and using the large Keldysh coefficient approximation must be compared.
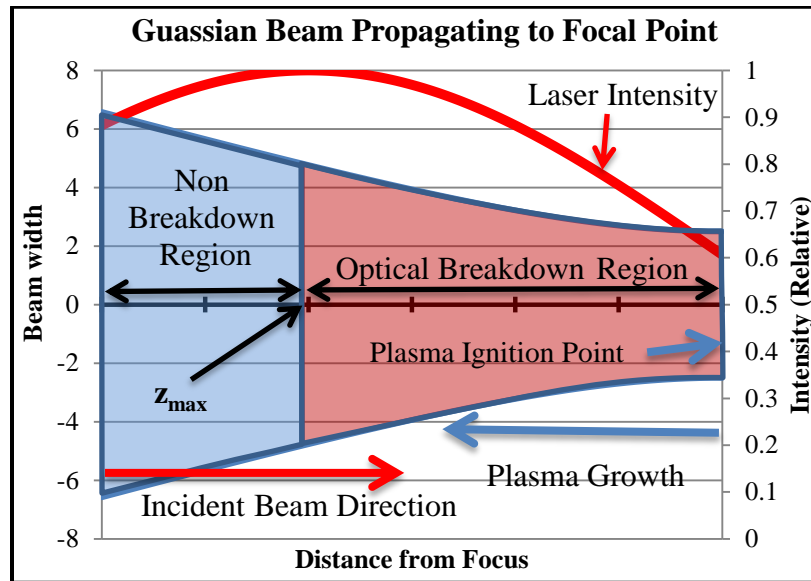
Figure 27 Optical breakdown and a non-breakdown region inside a Gaussian envelope

4.2   Effects of the Keldysh Coefficient on Population Density

Figure 28 shows a plot of the Keldysh coefficient, γ, versus axial distance from laser focus for different laser intensities for a 10ps laser pulse focused by an F/4.2 lens. The intensities have been scaled relative to the threshold intensity necessary to achieve a population density necessary to ignite plasma. Here β represents the multiplicative term

multiplied by the threshold power necessary to achieve plasma, $\beta = {}^P/_{P_{th}}$. For the region of Beta less than 5, γ is much larger than 1. For β larger than 5, the Keldysh coefficient quickly approaches 1, so making the approximation of Chapter 3 for large γ becomes less appropriate. To determine if the simplification of using the large Keldysh coefficient on determining peak electron density is appropriate, the case of water will be examined by comparing the directly calculating the threshold where no approximation is used to the large γ approximation method. This will determine the point where this simplification breaks down.
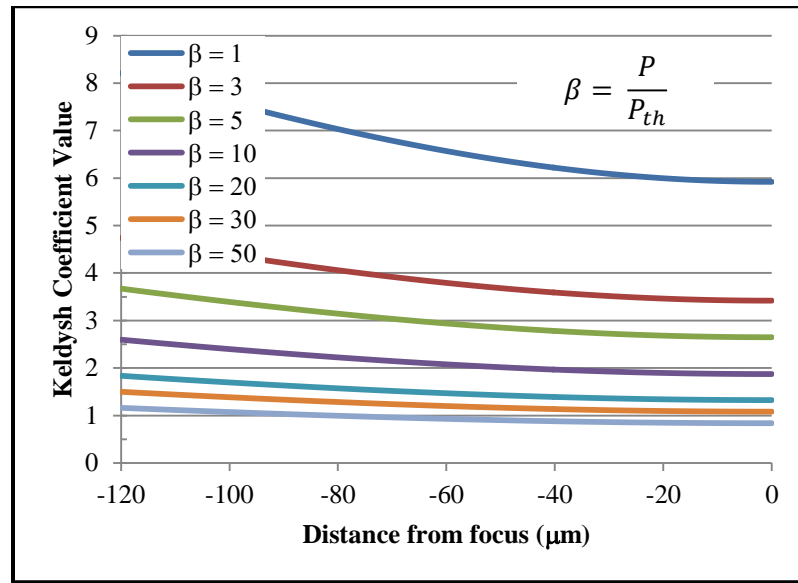
Figure 28 Keldysh coefficient, γ, versus distance from focus for 10 ps laser pulse.

4.2.1   Effects Large Keldysh coefficient, $\gamma >> 1$, approximation in the Photodisruption of Water

In chapter 3 the rate equation for electron density ionization was given by:

$$\frac{d\rho}{dt} = \left(\frac{d\rho}{dt}\right)_{mp} + \eta_{Aval}\rho - g\rho - \eta_{rec}\rho. \tag{44}$$

The multi-photon term was expressed as:

$$\left(\frac{d\rho}{dt}\right)_{mp}$$

$$\approx \frac{2\omega_0}{9\pi}\left(\frac{m'\omega_0}{\hbar}\right)^{3/2}\left[\frac{e^2}{16m'\Delta E\omega_0{}^2c\epsilon_0 n}I\right]^k e^{2k}\Phi\left(\sqrt{2k-\frac{2\Delta E}{\hbar\omega_0}}\right). \tag{50}$$

By not making the large Keldysh coefficient, $\gamma \gg 1$, approximation, the ionization energy terms become larger. This reduces the rate at which electrons are excited by multiphoton absorption. A plot of the rate that electrons are absorbed with and without the approximation for a large value of the Keldysh coefficient is shown in Figure 29. It is seen in this plot that the use of the large Keldysh coefficient approximation, $\gamma \gg 1$, leads to an overestimation of approximately 10,000 times the absorption rate when compared to the calculation when the Keldysh coefficient is considered, γ.
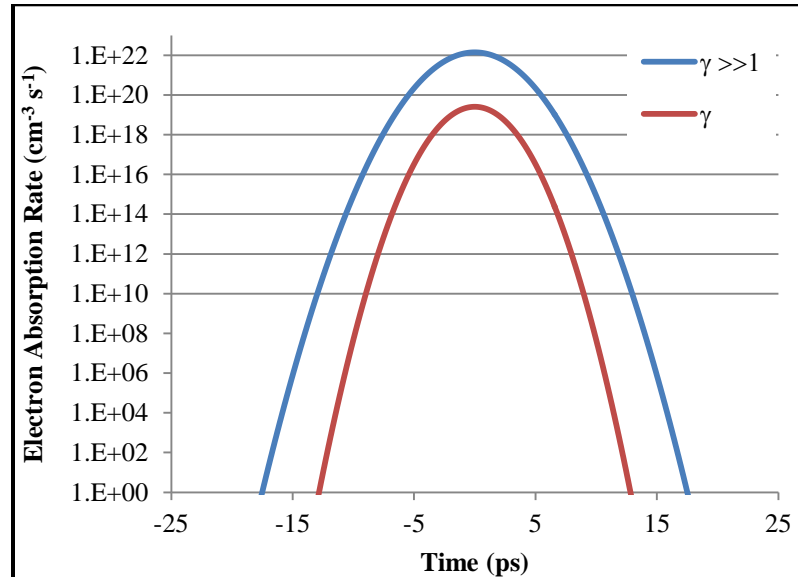
Figure 29 Multiphoton Absorption Rate over time with and without large γ approximation for 10 ps Pulse

The second term in equation 44 is the cascade term. Recalling from Chapter 3 this term can be expressed as:

$$\eta_{Aval} = \frac{\tau}{\omega_o \tau^2 + 1} \left[\frac{e^2}{cn\epsilon_o m\Delta E} I - \frac{m\omega^2}{M} \right]. \tag{78}$$

The term that is affected by the Keldysh coefficient is again the ionization energy term, ΔE. By not making the large Keldysh coefficient approximation, the avalanche ionization term does not promote many electrons into the electron cloud resulting in less electrons being promoted from this mechanism. Directly calculating the avalanche ionization without using the large Keldysh coefficient approximation, $\gamma \gg 1$, results in a loss of 36%, see Figure 30.
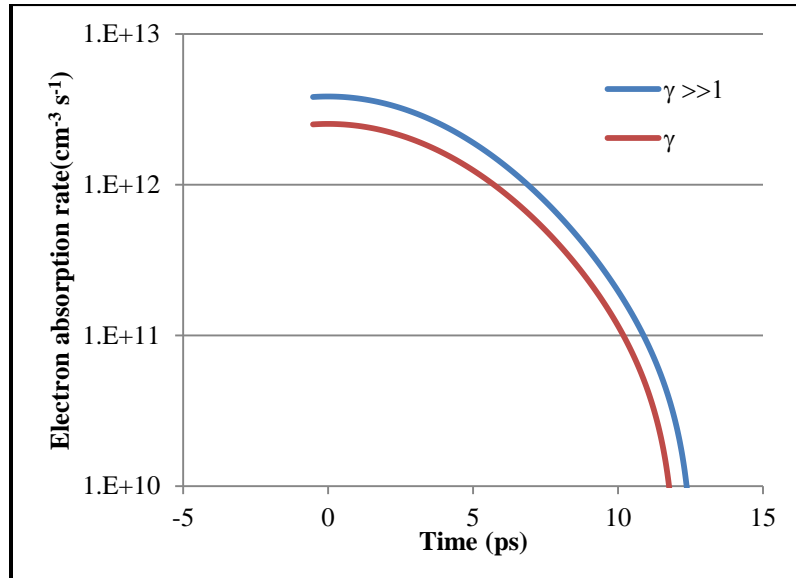
Figure 30 Avalanche absorption rate over time with the large Keldysh coefficient approximation and without, for 10 ps pulse.

By not making the large γ approximation, the threshold intensity necessary to achieve the threshold electron density that is necessary to support plasma formation will increase. A plot of the threshold condition is shown both the large Keldysh coefficient

approximation model, $\gamma \gg 1$, and the directly calculated model, γ, in Figure 31 in water. The functional form of both the large γ approximation term and the direct calculation term are the same. The start time at which each occurs is different though. This is because the avalanche and the multi-photon terms don't scale linearly with the increase in the intensity that is required for the direct calculation. The fluence required to reach threshold is 2.6 J/cm^2. This has a corresponding peak power of 0.285MW. The power required to reach threshold is 1.695 times higher when the large Keldysh coefficient approximation is not used. Figure 32 is a plot comparing the electron densities at focus to the relative power necessary to achieve them. The β curve is the electron density calculated using the large Keldysh coefficient approximation and the $\beta\gamma$ curve is the electron density calculated not using the large γ approximation. $\beta\gamma$ is defined as $\beta_\gamma = \frac{P}{P_{th\beta}}$. $P_{th\beta}$ is the threshold power for the large Keldysh coefficient approximation. The electron densities predicted by the two methods quickly diverge for larger β values. If electron density calculations are done for $\beta > 10$; the large γ approximation overestimates the electron population. The overestimated population will result in the model predicting that the plasma will be longer. At lower β values the electron densities are similar so the use of the large γ approximation is more acceptable. In the study that follows, a value of $\beta = 3$ will be considered for modeling the plasma evolution over time. To achieve the same electron density not using the large γ approximation would require that the $\beta\gamma$ be 1.56 times larger than the β using the large γ approximation. This is still reasonable, so the large γ approximation model will be used to calculate the electron density.
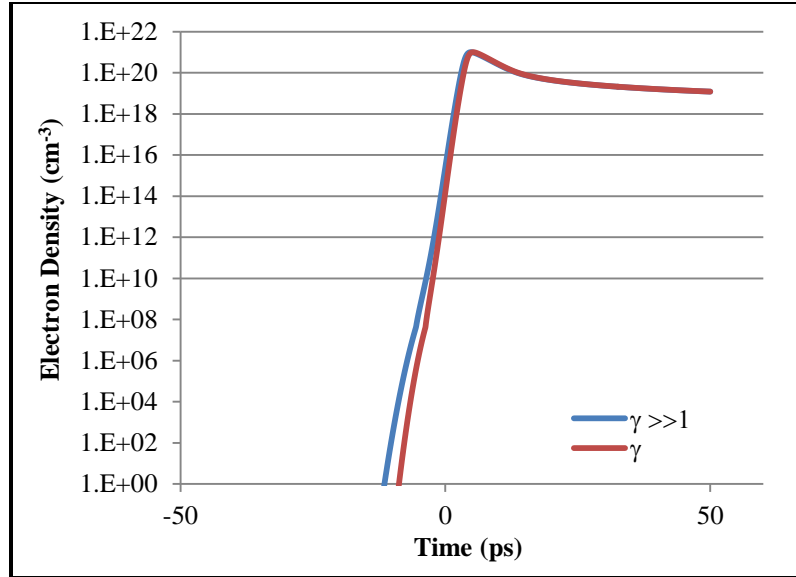
Figure 31 Threshold for F/4.2 10 ps laser pulse with and without large γ approximation.
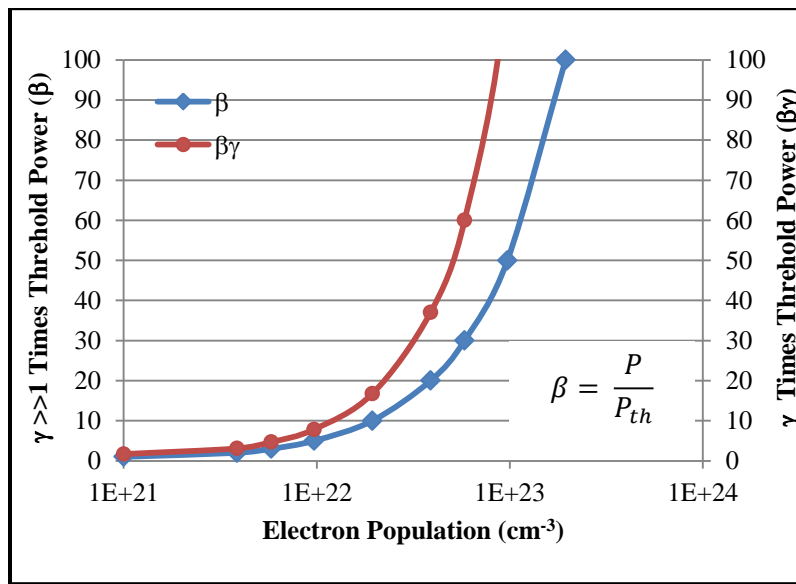
Figure 32 γ >> 1 approximation (β) and directly calculated (βγ) population density for various laser powers

4.3   Evolution of the plasma

As mentioned in Section 4.2, when a laser breaks down material, the region of breakdown is known as the optical breakdown region. When modeling this phenomenon, the plasma is considered to form when the electron density reaches plasma threshold

79

condition. For this study this value is taken to be 10^{21} electrons/cm^{-3}. The plasma will

last at this point for as long as the electron density exceeds this critical density. If each

point along the optical axis is considered in isolation as shown in Figure 33, an electron

density for each position can be calculated. If the electron density exceeds the threshold

density, this point can be considered to have plasma at that point. The region where

plasma exists and does not exist can then be determined by comparing the electron

density at each measured position over time. This allows the evolution of the plasma to

be studied. Summing the regions where the electron density is high enough to support

plasma allows the axial length where the electron density is high enough to support

plasma to be calculated.
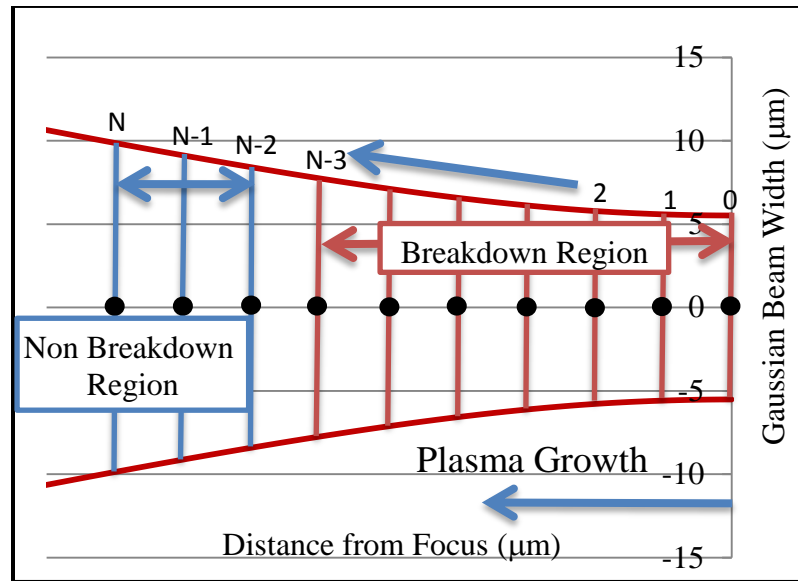
Figure 33 Discrete process used to model the plasma growth evolution.

4.3.1   Plasma Shielding

When the electron density is sufficient to support plasma, the plasma starts to

attenuate the laser pulse that is transmitted through it. As successive plasma form up

stream of the initial plasma, they start to attenuate the laser trying to propagate through

the plasma. At time before the electron density is high enough to support the plasma, the incident beam is unaffected by the electron population at this point. This reduction in transmitted intensity reduces the energy available for sustaining the plasma that formed closer to the laser focus. This causes the electron density of plasma downstream of the newly formed plasma to lose energy to maintain the plasma from the laser pulse. In the case of this model, this corresponds to a reduction in peak electron density achieved which reduces the time that the electron density is high enough to support the plasma. The time in which plasma is capable of maintaining itself can be determined by considering the difference in times where the plasma is above the critical density. The plasma starts when the electron density crosses the critical density boundary and continues until the electron density falls below the critical density, see Figure 34. For the period of time where the electron density is above the critical density, the plasma shields the plasma downstream from laser energy. By breaking up the interaction volume into segments as depicted in Figure 33, the start and stop times for each of the plasma can be determined for each sample point along the axis. By using the position of each of the plasma and the time that each one goes above and goes below the critical density an attenuation length can be derived that can describe the effective distance the source must propagate to reach a point where plasma has formed. Multiplying this length by an attenuation coefficient allows the attenuation function to be expressed as

$$f(z,t) = \exp(\alpha z_d(z,t)). \tag{79}$$
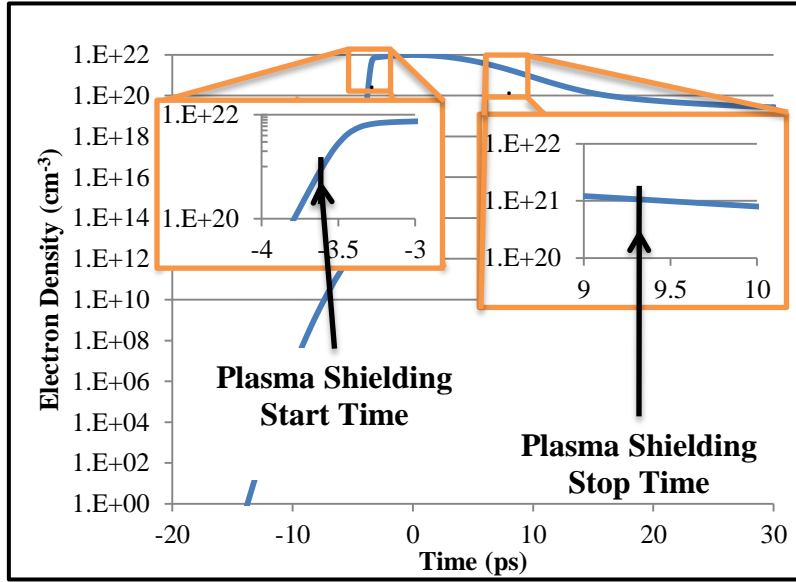
Figure 34 Plasma ignition and stop times based on critical density

α is an attenuation constant and $z_d(z,t)$ is a function describing the effective length of the

plasma that the laser propagates through. For the purposes of this study the attenuation

coefficient for three times threshold presented by (115) for a 30ps laser is used for the

value of α, 75 cm^{-1}. $z_d(z,t)$ can be found by first calculating the un-attenuated electron

density along the path of the incident beam and determining the start and stop times for

each of the plasma. Before the electron density is high enough to support the plasma, the

incident beam is unaffected by the electron population at this point so this function would

be zero. When the electron density is high enough to support the plasma, the incident

beam is attenuated so this function would have an effective length. At the time at which

the electron density falls below the critical point necessary to support the plasma, the

incident beam is no longer attenuated. The effective length of the attenuation function

can be determined as a function of time. A typical plot of $z_d(z,t)$ at focus is shown in

Figure 35. Each of the points represents a location where plasma has started or stopped

as indicated. These points are then fitted to third order polynomial function that is

piecewise continuous to the start time and stop time data defined as f(t). The attenuation length, $z_d(z,t)$, can then be expressed as

$$z_d(z,t) = \begin{cases} (f(t) - z) \, if \, f(t) - z \geq 0 \\ 0 \, otherwise \end{cases}.$$ (80)

This technique can also be used in the case multiple materials, see Figure 36, by calculating a function description for each region where plasma forms. In the case of Figure 36, $z_d(z,t)$ can be expressed as

$$z_d(z,t) =$$ (81)

$$\begin{cases} f_1(t) + f_2(1) - z \, if \left((f_1(t) + f_2(1) - z \leq 0) \wedge (z \geq Z_{12}) \right) \\ f_2(t) + Z_{12} - z \, if \left(\left(((f_2(t) + Z_{12} - z) \leq 0) \right) \wedge (z < Z_{12}) \right). \\ 0 \, otherwise \end{cases}$$
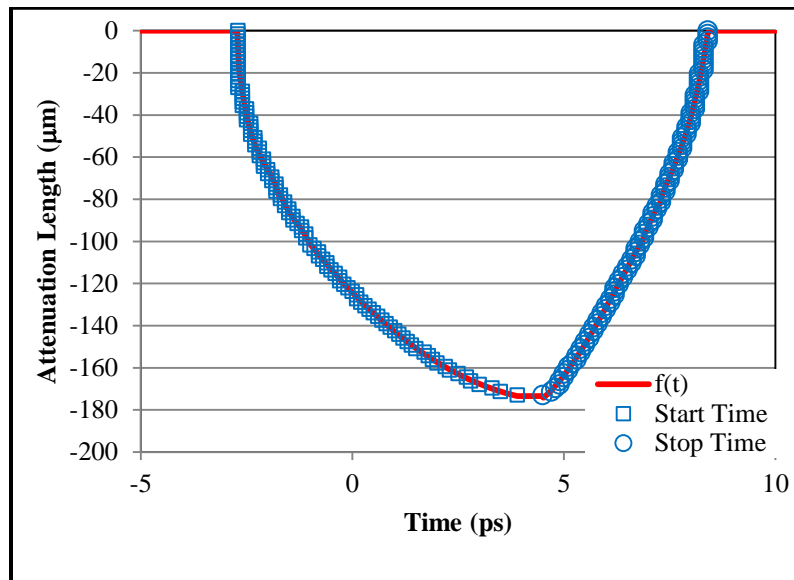
Figure 35 Effective attenuation length over time due to plasma shielding for 10ps pulse
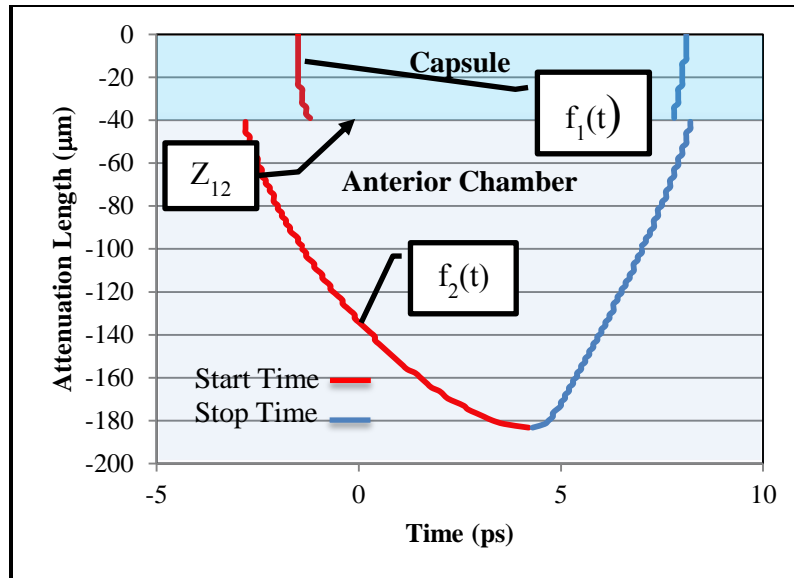
Figure 36 Plasma start and stop times for laser focused in capsule.

4.3.2   Effects on Intensity with Plasma Shielding

Once the attenuation length as a function of time and position is found, the next step in the model is to calculate the growth of the electron density with consideration of attenuation. The only change in the model is that f(z,t) of Equation 79 is multiplied by the intensity function. Figure 37 shows the effect of the plasma formation on the intensity of the beam seen at focus over time. Here the incident beam with no attenuation is shown with a peak intensity of approximately 13 W/cm^2 but drops to a peak intensity of 6.1 W/cm^2 once the attenuation function is considered.
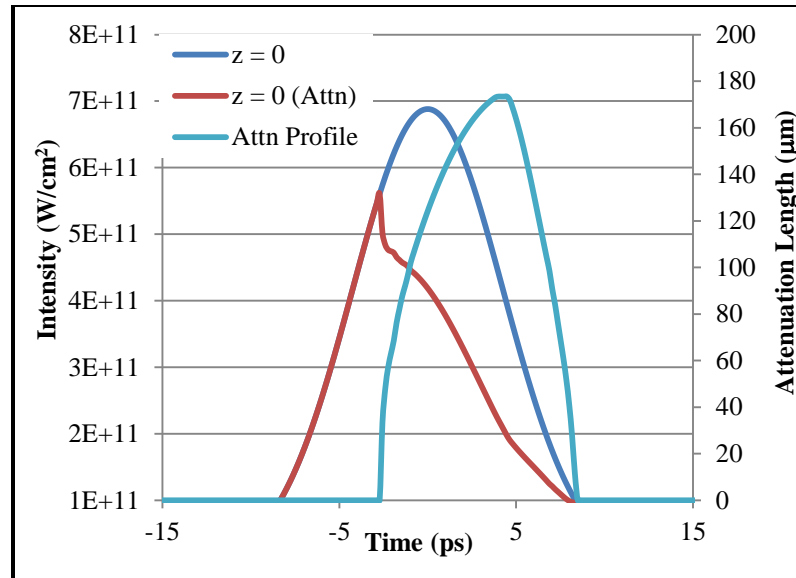
Figure 37 Laser Pulse Intensity over time with and without attenuation consideration

4.4 Plasma Interaction at and Near the Anterior Lens

When a capsulotomy is being cut at the anterior portion of the lens, the laser focus is targeted to cause a photodisruption below the capsule and be sequentially moved up until the photodisruption goes through the capsule into the anterior chamber. Although theoretically the laser could be focused directly on the capsule and the capsule could be photodisrupted, present uncertainties in measurement techniques do not allow for this. Because of this uncertainty, several pulses are used to cut the capsule. These pulses move progressively anteriorly out of the lens into the anterior chamber. This leads to five cases to be studied as the laser moves into the anterior chamber. Case 1: The laser is focused in the fibrous mass. Case 2: the laser is focused in the capsule with sufficient energy to disrupt the capsule. Case 3: The laser is focused in the fibrous mass sufficiently close to the capsule such that the capsule is cut with the laser pulse. Case 4: The position of the laser focus is such that only part of the capsule is photodisrupted. Case 5: The laser focus is such that the electron density is high enough to photodisrupt in

85

the anterior chamber and in the fibrous mass but insufficient to photodisrupt in the capsule. These separate cases are possible because the binding energy of the capsule is slightly higher than that of the fibrous mass and aqueous humor. As previously mentioned in Chapter 2, the aqueous humor will be treated like water with a binding energy of 6.5eV, the capsule is treated as having a binding energy of 7.5eV, and the fibrous mass is treated as having a binding energy of 6.8eV. Although the length of the aqueous humor and fibrous mass can be considered semi-infinite for modeling purpose, the capsule is finite in the model. A capsular length of 40 μm which is representative of porcine capsular dimensions will be used for modeling. This is done because *ex vivo* testing described later in this thesis uses porcine eyes.

To examine multi-material interaction, the model developed to this point will be modified to put the materials with different binding energies along the optical axis. The effects of the material placement along the optical axis can then be modeled using the technique outlined in Section 4.4. At each sample point along the axis, the electron density as a function of time was determined. During the evolution of the electron density the absorption starts and stops points were determined. The data was then fit to a third order polynomial for each region to define the effective attenuation length as a function of time. Once the attenuation function was defined, the electron density was calculated again to determine the electron density with the consideration of the attenuation due to the plasma closer to the laser than the point of calculation. The peak population of each axial point along the axis was then determined and compared to the population necessary to support plasma. A critical density of 10^{21} electrons per cm^3 is used as the threshold for the plasma formation. Plots showing the progression of the

86

plasma over time and the electron density versus position are used to show the effects of the laser interaction near and at the boundary between the crystalline lens and anterior chamber.

4.4.1 Case 1: Plasma Interaction with the Fibrous Mass
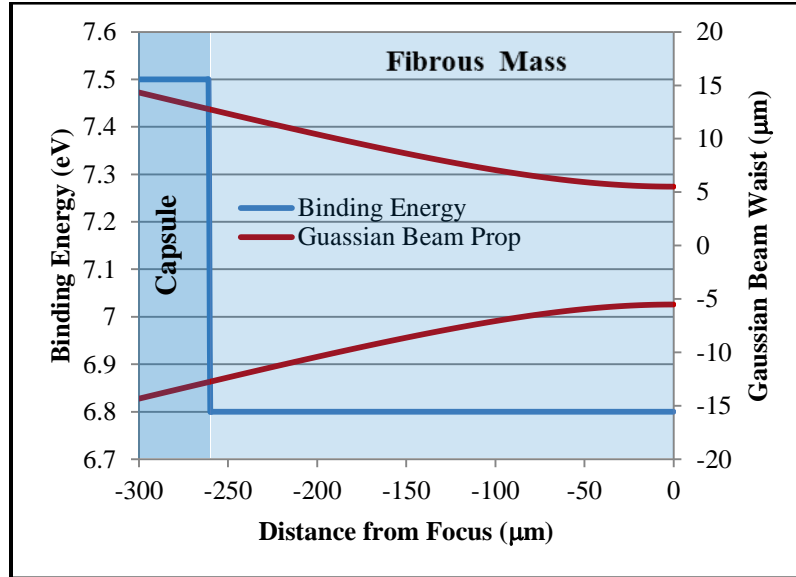
Figure 38 Beam Focus location in fibrous mass approximately 260 μm from lens capsule

Case 1 focuses the laser deep in the fibrous mass of the lens as shown in Figure 38. This case is the uniform media case. The laser power used for this analysis is three times the threshold power value, $\beta = 3$, of the fibrous mass. For comparison purposes, the moving breakdown model is used as a guide to the expected length of the plasma. Using the moving breakdown model, the length of the plasma is calculated to be approximately 176 μm. The laser is focused approximately 260 microns beyond the capsule in the fibrous mass of the lens. The focus spot size is based off of an F/4.25 system. The corresponding $1/e^2$ Gaussian beam waist is 5.51 μm. The expected Rayleigh

range for the beam is 124 μm in the lens. The fluence necessary to reach threshold was 2.6 J/cm^2.

The peak electron density for a 10ps laser is calculated and shown in Figure 39. This figure shows an axial length plasma is approximately 175 μm. This is within 1 microns of the moving breakdown model. Figure 40 shows the electron density for discrete times during the laser interaction. Here it is seen that the electron density rises and falls as the laser pulse interacts with the material. This is different than the moving breakdown model because the time evolution of the pulse is considered. These discrete times can be modeled to determine the peak electron density versus time; this is shown in Figure 41. This model actually predicts that the plasma starts later than what the moving breakdown model predicts. It also rises faster than the moving breakdown model. The plasma model shows that the plasma extinguishes approximately 8 ps after forming.
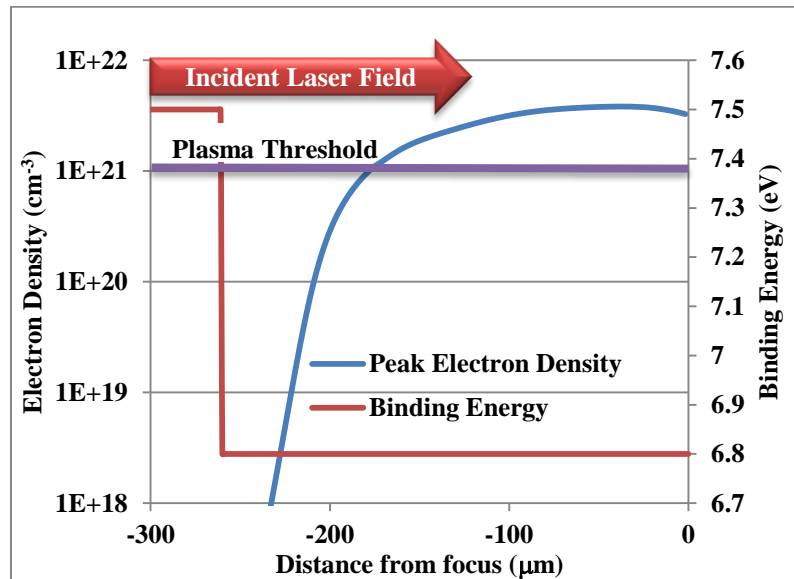
Figure 39 Peak electron density along axial length moving away from focus
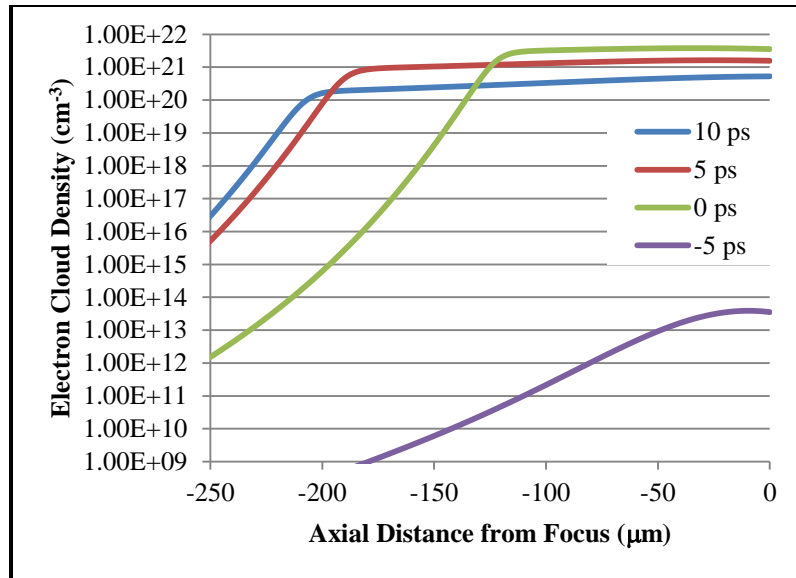
Figure 40 Electron Cloud Density versus Axial Distance from Focus for discrete times
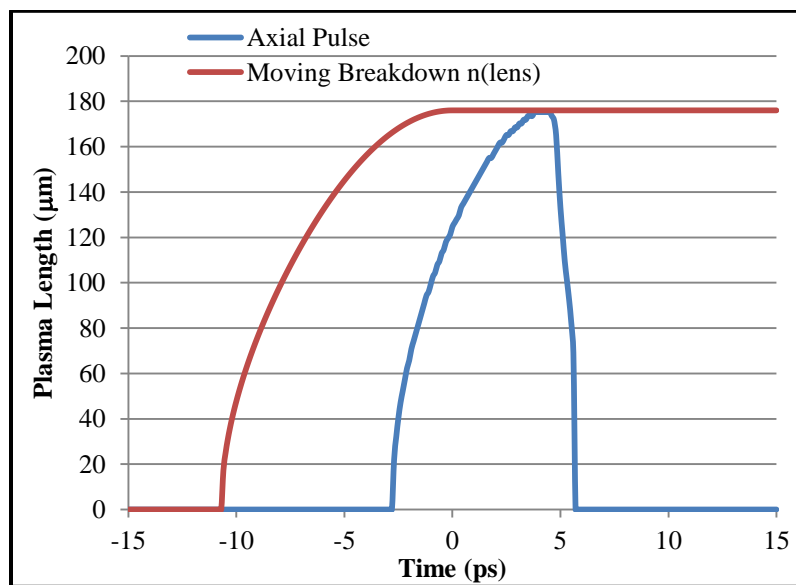
Figure 41 Plasma length over time in water for $\beta = 3$ for a 10ps pulse.

4.4.2 Case 2:Focus in the Capsule
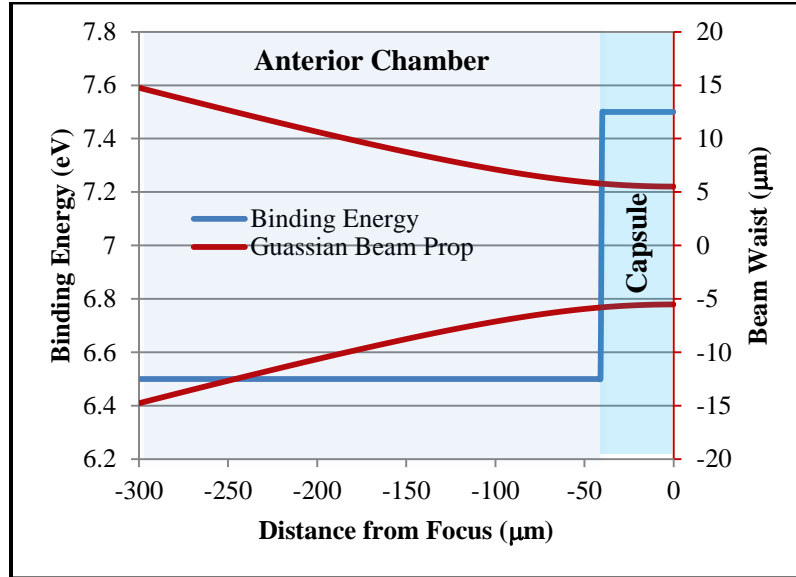
Figure 42 Focus in the capsule for laser at for 3 times laser threshold power, $\beta = 3$.

For the case that the laser is focused in the capsule, the model predicts that the plasma forms in the anterior chamber before forming in the capsule. Figure 43 shows the start time for the start and stop times for the electron density to reach and fall below the threshold condition when no attenuation is considered. All laser beam parameters used are the same as was discussed in 4.4.1 for this calculation. The electron density reaches threshold in the anterior chamber before the capsule by approximately 0.8 ps. A plot of the peak electron density versus position is shown in Figure 44. The peak electron density predicted by the model is slightly higher than what is predicted by the moving breakdown model. The model predicts a plasma length of 182 µm. The time evolution of the plasma is shown in Figure 45. Again in this plot, the predicted plasma length is greater than the length predicted by the moving breakdown model for the lens. This is not unexpected because the binding energy of the aqueous humor in the anterior chamber

90

is less than the binding energy of the fibrous mass. This model does predict that the

capsule is dissected by the plasma which forms in the capsule.
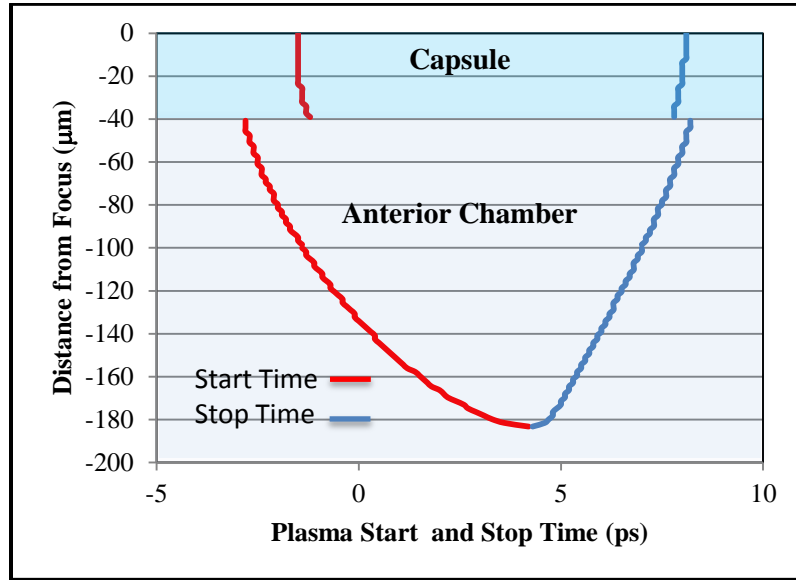
Figure 43 Plasma start and stop times versus axial position relative to focus.
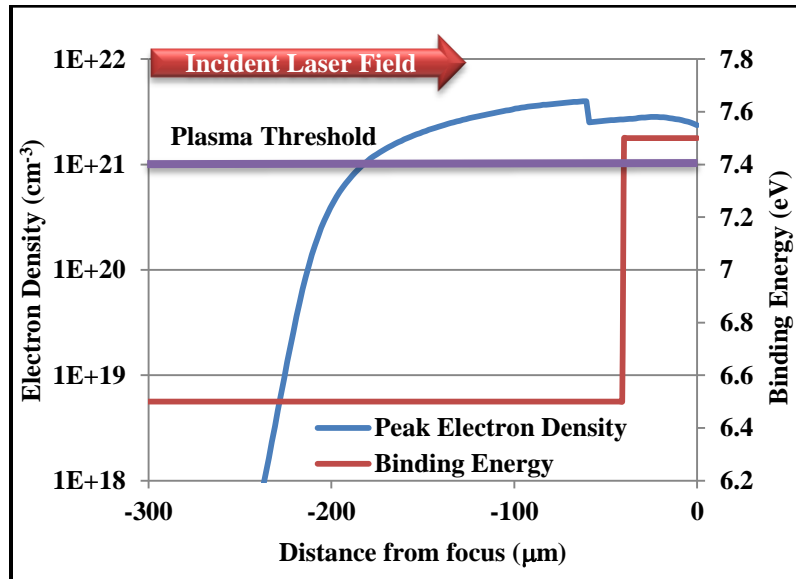
Figure 44 Peak Electron Density as a function of position from laser focused for 3 β = 3.
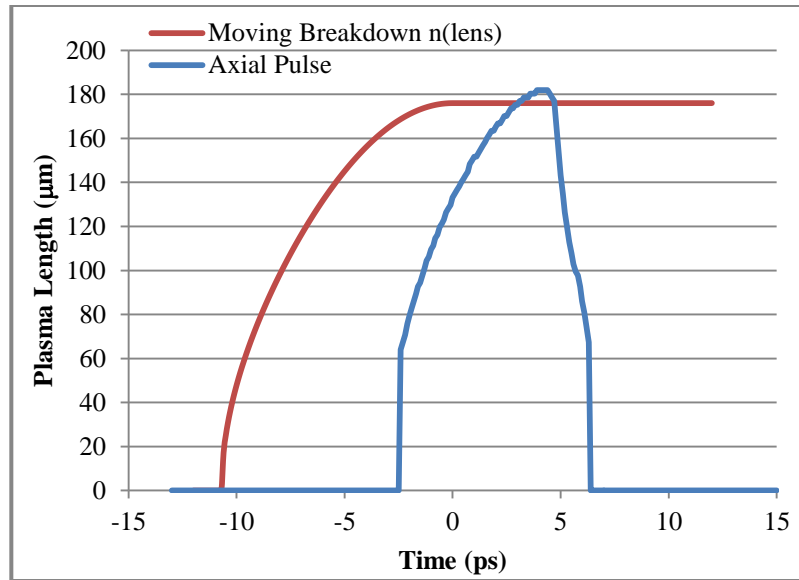
Figure 45 Plasma length versus time for laser focused in the capsule for 3 times threshold power, β = 3.

4.4.3   Case 3: Focus beyond the Capsule in the Fibrous Mass
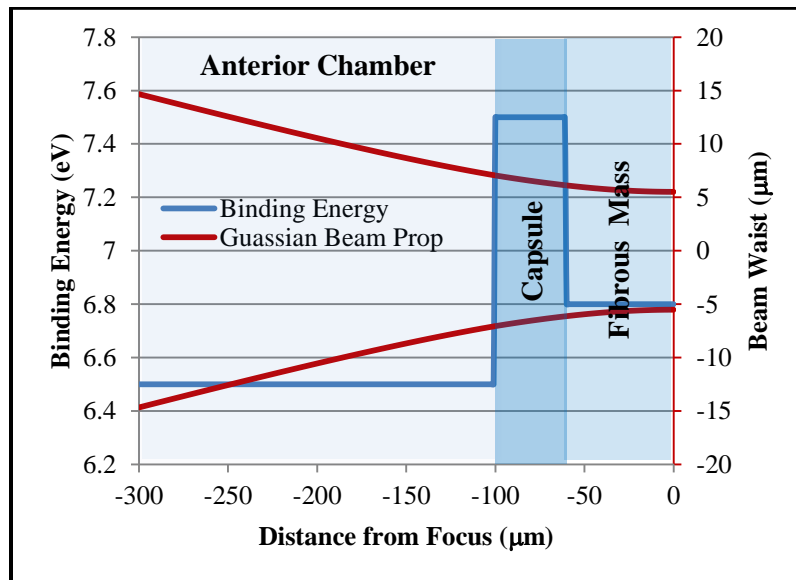
Figure 46 Focus near the capsule for laser at for 3 times laser threshold power, β = 3.

In this case the laser focus is in the fibrous mass 60 μm posterior of the capsule. This represents the plasma forming in the fibrous mass and continuing through the

capsule into the aqueous humor, resulting in the capsule being dissected by the plasma. All parameters are as defined in Section 4.4.1.

The peak electron density curve is shown in Figure 48. Here it is seen that in the region of the capsule the electron density is reduced and causes a discontinuity in the electron density across the capsule. The electron density is still high enough though to support plasma.

In Figure 48, the total plasma length is larger than what is expected using the moving breakdown model for the lens. The reason for the plasma length to be larger than the predicted moving breakdown model is the aqueous humor's a binding energy that is lower than the binding energy of the fibrous mass. The threshold intensity used was determined using the fibrous mass binding energy value to find the appropriate laser energy to ignite the plasma. The fact that the binding energy of the aqueous humor is lower than the binding energy of fibrous mass causes the electron population to be high enough to support a plasma for longer than what would be expected using the moving breakdown model for the fibrous mass alone. As can also be seen in Figure 47, the plasma does not immediately start in the capsule. This results in the plasma length remaining constant for a short period of time as shown in the plot. Once the plasma does form, the length of the plasma continues to grow. The capsule would be expected to be dissected by the laser in this case.
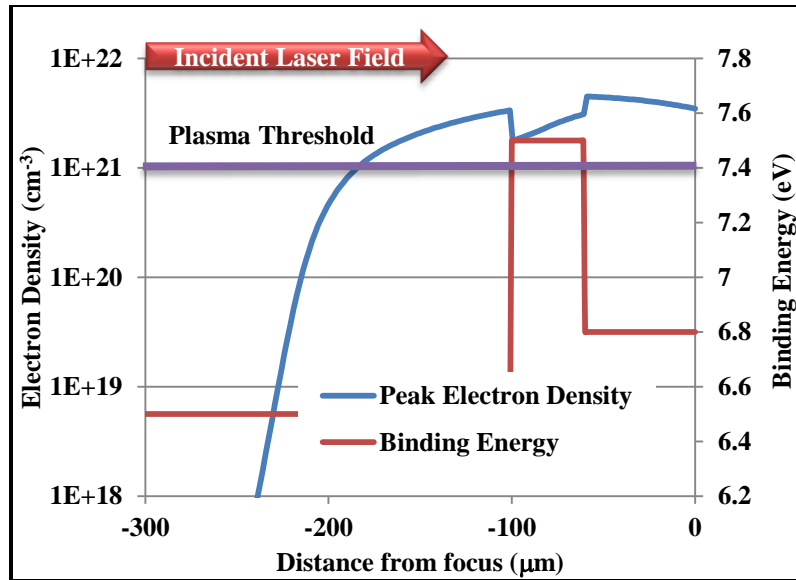
Figure 47 Peak Electron density relative to focus for β = 3
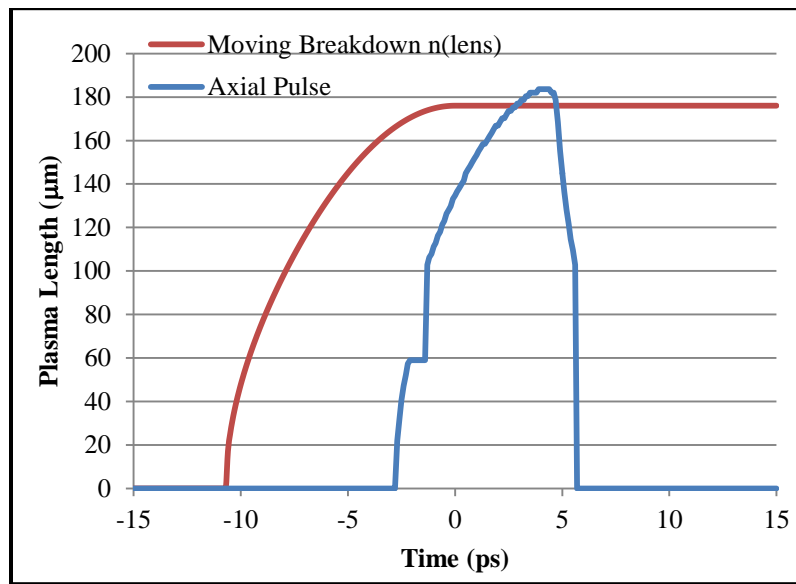
Figure 48 Plasma Axial Length versus Time for multiple element model and moving break down model for β = 3

4.4.4   Case 4: Laser focus 100 μm posterior of the capsule for β = 3
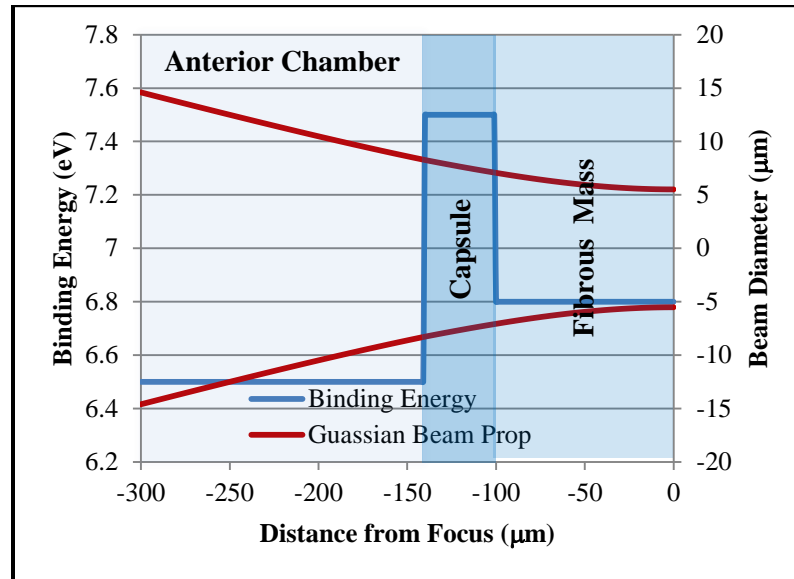
Figure 49 Laser focus 100 μm beyond capsule

In this case, the laser is focused 100 μm beyond the capsule. The laser parameters are the same as the parameters defined in Section 4.4.1. This case shows the condition where the plasma generated by the laser pulse is insufficient to cut all the way through the capsule.

The peak electron density versus position is shown in Figure 50. As the pulse interacts with the capsule the electron density is high enough next to the fibrous mass but slowly deteriorates across the capsule to the point where it no longer is able to support plasma. The result of this is that the capsule would only be partially dissected. In the anterior chamber of the eye, the electron density again increases above the plasma.

The time evolution of the plasma is presented in Figure 51. The plasma forms in the fibrous mass and grows towards the capsule. At the capsule, the plasma does not initially form. This causes the plasma length to remain constant for a period time.

Eventually the plasma forms in the capsule and propagates through most of the capsule. There is a part of the capsule where the plasma does not form so it would be possible for this portion of the capsule to remain unaffected by the laser. The length is predicted to be longer than the moving breakdown model predicted length because a large portion of the beam is in the aqueous humor. The binding energy of the aqueous humor is less than the binding energy of the fibrous mass in this model. The calculated plasma length calculated by the model is 185 μm
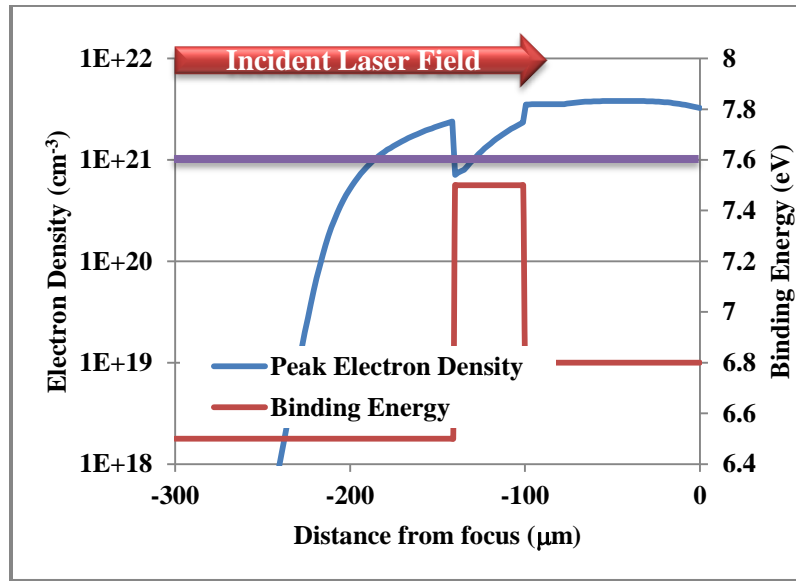
Figure 50 Peak electron density versus axial position for laser focus 100 μm from capsule in fibrous mass for laser power three times threshold, β = 3.
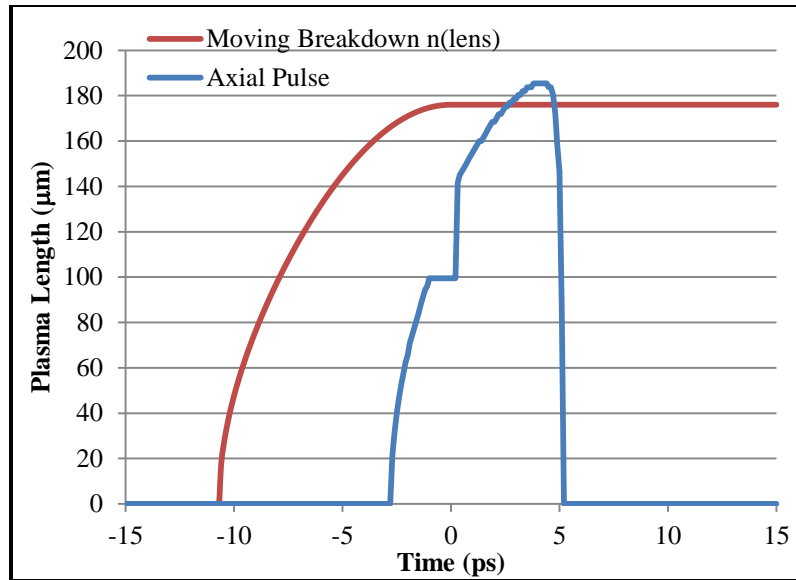
Figure 51 Plasma length versus time for laser focus 100 μm from capsule in fibrous mass for laser power three times threshold, β = 3.

4.4.5   Case 5: Laser focus 140 μm posterior of the capsule for β = 3
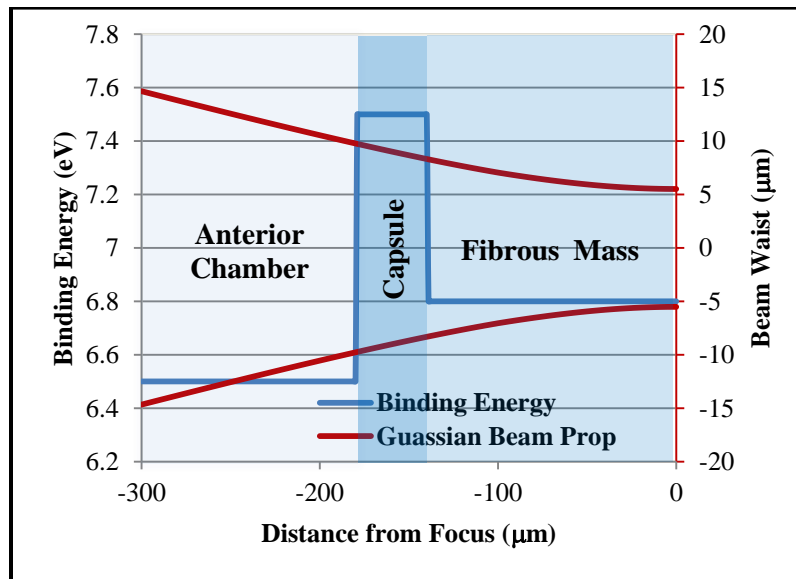
Figure 52 Laser focus 140 μm beyond capsule for laser power three times threshold, β = 3.

In this case the laser focus is 140 mm to the posterior of the lens. . The laser parameters are the same as the parameters defined in Section 4.4.1. This case shows a condition where plasma does not form in the capsule.

97

The peak electron density versus position is shown in Figure 53. As the pulse interacts with the capsule, the electron density is high enough to support plasma next to the fibrous mass but is unable to support plasma across the capsule. In this case, the plasma would not be expected to dissect the capsule.

The time evolution of the plasma versus time is shown in Figure 54. The plasma ignites in the fibrous mass and grows towards the capsule. At the capsule the plasma length remains the same for approximately 2 ps. Then the plasma briefly ignites in the aqueous humor. As the electron density decreases to the point where plasma cannot be supported in the anterior chamber, it skips back to the fibrous mass. Once in the fibrous mass, the plasma eventually dissipates. The interaction length is longer than the moving breakdown predicted model with a length of 187 microns.
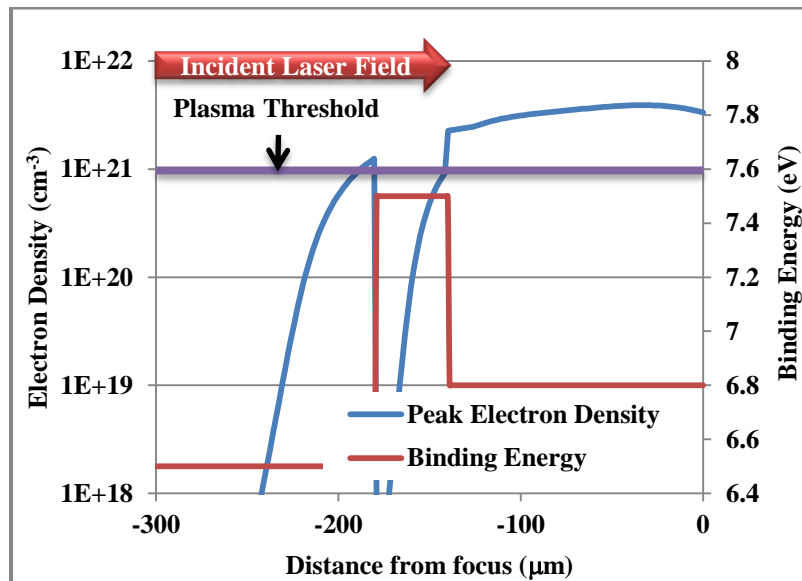
Figure 53 Peak electron density versus axial position for laser focus 140 μm from capsule in fibrous mass for laser power three times threshold, β = 3.
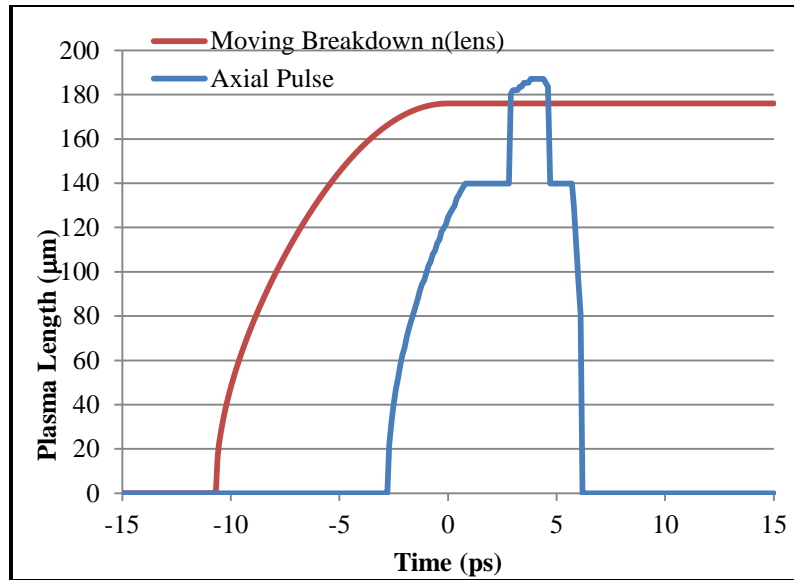
Figure 54 Plasma length versus time for laser focus 140 μm from capsule in fibrous mass
for laser power three times threshold, β = 3.

4.5   Summary and Conclusions

In this chapter, modeling has been considered to look at the interaction of the

laser with the various materials of the lens and anterior chamber. . In the first model in

continuous media, the model predicted an axial length in the plasma that is very

comparable to the moving breakdown prediction. This model considered the effects of

plasma ignition ahead of the initial plasma formation. When the model was expanded to

look at plasmas generated in an environment where there are multiple materials as are in

the eye, a more complex interaction occurred. In some cases, the plasma was continuous

across all the different materials and in other cases the plasma did not form completely in

all the different materials resulting in the materials not being cut. In the time evolution of

the plasma across the boundary of an eye using porcine dimensions for the capsular

length, it was found that the moving breakdown model for one material was insufficient

to describe the interaction of the laser. There were cases where the plasma evolution is

affected by the proximity of the capsule and resulted in the plasma not behaving as would be predicted by the moving breakdown model.

In the next chapters, an experimental perspective will be considered to see the effects of the laser interaction in biological materials. This process will start by identifying a laser system that is necessary to treat eyes. This system will then be used to study laser interaction with model materials representing the aqueous humor and the fibrous mass. The information gained from this experiment will then be applied to look at laser interaction in *ex vivo* testing done on porcine eyes.

CHAPTER 5 TREATMENT LASER SYSTEM

The laser system used to conduct the photodisruption experiments is critical for the successful analysis of the anterior lens boundary interaction. To be able to treat an eye, the system must control the position of the laser focus spot very accurately to ensure that only areas of interest are treated by the laser system This requires that the laser system not only scan in two dimensions, but in three dimensions. Because each eye is different, the system must adjust laser focal position to each eye prior to treating the capsule with the laser. This puts a need not only for the treatment laser system, but also a beam directing system that adjusts the main laser system for each eye prior to treatment with the laser. The method that was employed is outlined in Figure 55. The beam directing system is a calibrated scanning slit laser and camera system. Prior to the eye being treated with the main laser system, the slit laser scans the eye, stopping periodically, while an image was taken. The calibrated camera system determines the mechanical position of the lens relative to the laser focus. The laser system is then adjusted to position the laser focus to the appropriate location. The laser system then treats the area of interest. Periodically during the treatment of the eye, an integrated optical imaging system is used to monitor the progress of the surgery. This camera system is collinear to the laser.

Given these general requirements, specific requirements of operating on a human eye need to be considered for the treatment laser system requirements. In Chapter 2 Table 3,

clinical data was presented on the various anatomical features of Filipino eyes. This data sets minimum requirements on the laser system to treat human eyes. To be effective in treating humans, the treatment laser must be able to measure and treat eyes with these characteristics. The range of corneal thickness for the population was from 0.45 mm to 0.64 mm. The anterior chamber depths ranged from 2.1 mm to 4.48 mm. The lens thickness ranged from 2.7 mm to 6 mm. The minimum depth that the laser would need to reach to treat 99.7% of patients is average cornea and anterior chamber depth measurement minus three standard deviations of each measurement minus an arbitrary distance from the capsule. This arbitrary distance is selected to ensure that the laser focus is moved through the capsule even if there is gas build up from below due to photodisruption in the lens. It is selected to be 0.5 mm. The minimum depth that the laser must operate at is 2.01 mm. The maximum depth that the laser system must operate at is the sum of the average cornea, anterior chamber depth, and lens measurement plus three standard deviations of each measurement. The maximum depth is 11.39 mm. The minimum depth and maximum depth set the range that the laser system must work at axially. This distance is 9.38 mm in medium. Additional axial depth can be added to compensate for other tolerances in the system. An eye can dilate up to 10mm. This sets the minimum diameter that the experimental laser system must work over. When treating an eye, the system must also be able to determine where the lens is under the cornea.

In the next section, a more detailed overview is given about the laser system and operational characteristics.
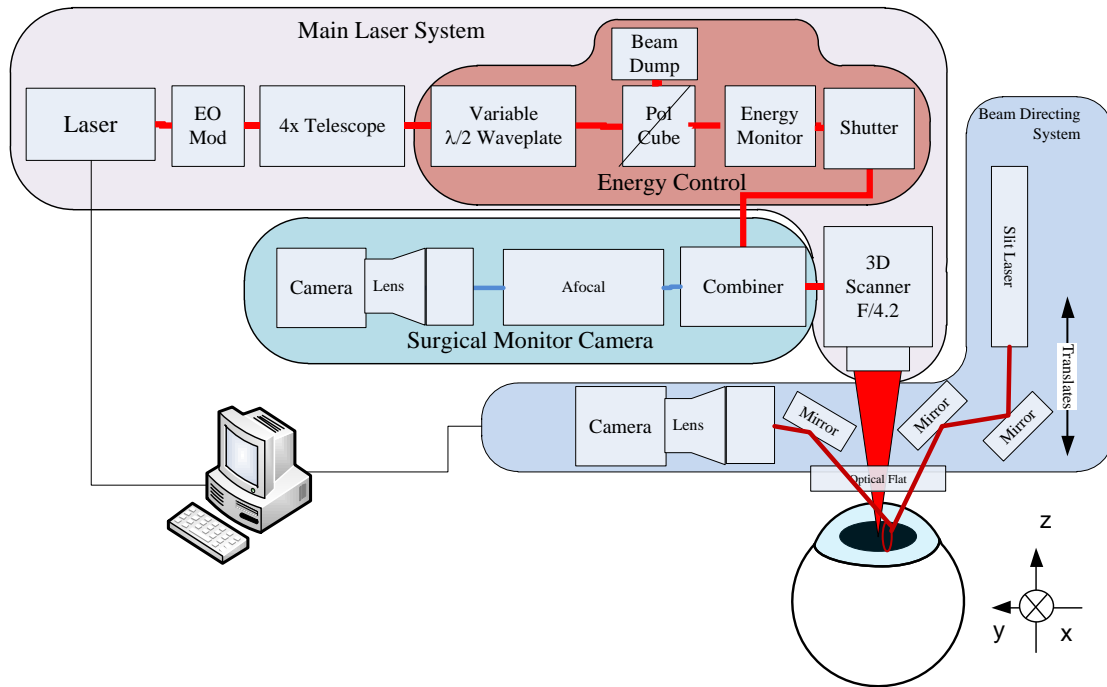
Figure 55 Block diagram Laser System consisting of the main laser system, surgical monitor camera, and beam directing system

5.1   Main Laser System

The main laser system was outlined in Figure 55. The laser in the system is a 10ps Nd: YVO_4 laser. Gating the laser is an electro optic modulator subsystem. This subsystem consists of an electro optic crystal and polarizer combination. The electro optic modulator subsystem is necessary because of the laser design. The lasers first several pulses of a series of pulses must be blocked because these pulses have a greater than desired energy. To control the energy at the eye, an energy control subsystem is used. This subsystem consists of a light valve, shutter, and an energy monitor. Coupling the output of the electro optic modulator to the energy control subsystem is a 4x telescope. This telescope is a Newport HB-4x.AR33. In addition to enlarging the beam diameter for the energy control subsystem, the telescope is used to over fill the input to

the 3D laser beam positioning system. The 3D laser beam positioning system consisting

of a z scanning module integrated with an f-theta based galvanometer scanning system.

In the next several sub sections more detail is given on the various components outlined

above.

5.1.1   Laser

The laser in the laser system is a Lumera diode pumped Nd:YVO$_4$ Rapid System

(116). The laser parameters for this laser are given in Table 5. This diode pumped laser

system is designed around a seeder laser and two amplifiers. The seeder laser has a

50MHz cavity. Pulses from the cavity are picked by Pockel cell and directed to the two

stage amplifier subsystem. The output of the two amplifiers is controllable with the

adjustable waveplate in combination with a Brewster window. A schematic of the laser

design is given in Figure 56.

Table 5 Output Beam Characteristics of the Lumera Laser System (116)

Output Beam Specifications: Model Rapid	
Wavelength	1064 nm
Average power	~10 W
Repetition rate	10 to 500 kHz
Free-running frequency drift	< 5 kHz/hour
Spatial mode TEM $_{00}$	$M^2 < 1.2$
Pulse width (sech^2 pulse fit)	< 13 ps
Amplitude noise	< 1 % rms
Polarization, linear	> 100:1, s
Beam divergence (full angle)	< 2 mrad
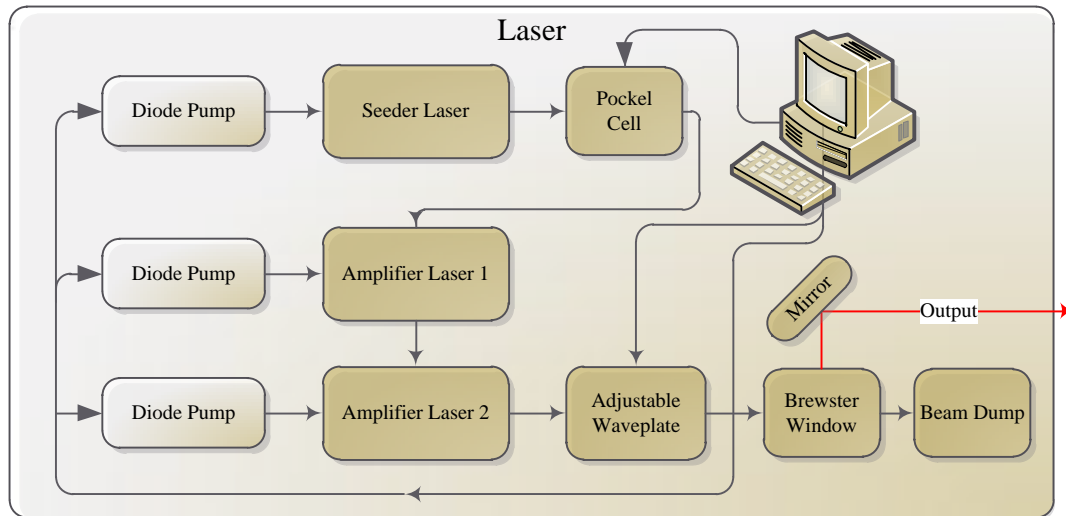
Figure 56 Operational schematic of the Lumera Laser System

5.1.2   Electro Optic Modulator System

An external electro-optic modulator (EOM) system is used to gate the picosecond laser system. The need for this is twofold. The first reason for the EOM is to control the first several laser pulses. Because of the two stage amplifier design of the laser, the first several pulses going through the amplifier chain are significantly higher than desired. To control this, the external EOM system is used as an electro optic shutter to block these pulses from reaching the eye. The EOM system also allows the laser to be firing continuously during surgery, while the system prepares the various other subsystems for surgery. An example of system preparation is the prepositioning of the galvanometer mirrors prior to photodisrupting the laser in the lens. Once a pattern is generated, the EOM is opened and laser pulses are focused into the eye. The electro optic modulator system consists of an electro optic (EO) crystal, Con Optic 360-40, in combination with a Newport 05BC15PH.9 polarizing beamsplitter cube and a Newport 10RP12-34 $\lambda/2$ waveplate. The $\lambda/2$ waveplate is used to tune the EOM for maximum attenuation when

put in combination with the polarizing beamsplitter. The EOM system is implemented to be in an off state until voltage is applied to the EO crystal. In the off state no light goes to the eye plane.

The electro optical crystal used for the EOM is Lithium Tantalate, LTA. The LTA electro-optic modulator has the ability to knock down the laser by a factor of approximately 300 to 1 with a ½ wave voltage of 400V. This contrast ratio is sufficient to extinguish the laser during normal operation. A table of other optical properties of the LTA crystal is given in Table 6 .

Table 6 Optical Characteristics of LTA

The Sellmeier 2 index coefficients	$n^2 = A + \dfrac{B}{\lambda^2 - C} + \dfrac{D\lambda}{\lambda^2 - E}$
A	4.52118266929
B	.0848939034985
C	.0397341352617
D	27.2917136782
E	1156.32081918
Pulse Elongation	232 fs
Aperture	2.7 mm
Crystal length	90 mm

5.1.3   Energy Control System

The energy control system (ECS) is used to control the amount of energy that goes to the eye. This subsystem consists of a Newport 10RP12-34 λ/2 waveplate in a computer controlled Newport PR50CC rotation mount in combination with a Newport 05BC15PH.9 polarizing beamsplitter cube, Newport PL15 beam dump, custom energy

monitor, and a Thorlabs SH05 shutter. The energy monitor was used to set the laser

energy that went to the eye prior to treating the eye with the laser. The EOS tunes the

waveplate to meet the user defined energy at the eye. Once the desired energy is set, the

EOM is driven to minimize transmission and the SH05 is opened. The EOM then is

opened and laser pulses are focused at the desired location.

5.1.4   Axial, z, Scanning Device

The axial focus control of the system was accomplished using a Scanlabs

VarioSCAN 20i system. This system puts a prescribed amount of defocus in the input

beam going into fθ lens of the system. The defocus changes the position of the best focus

for the laser at the target plane allowing for the depth of the photodisruption to be

adjusted. An image and the general mechanical characteristics are given in Figure 57.

The typical performance characteristics of the VarioSCAN 20i are shown in Table 7.

The system implementation of the VarioSCAN 20i in a three dimensional scanning

system is to place it in front of the galvanometer mirrors at a vendor prescribed distance.
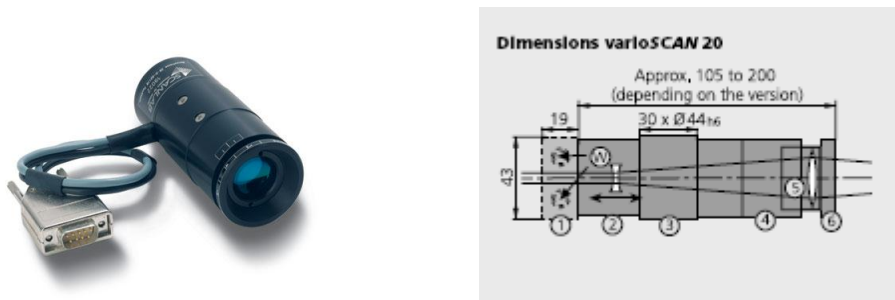
Figure 57 Picture and mechanical characteristics of the VarioSCAN 20

Table 7 Characteristics of the VarioSCAN 20

Optical Characteristics	
Design Wavelength	1064 nm
Beam Input Aperture up to max.	8 mm
Output Aperture up to max.	20 mm
Dynamic Performance	
Tracking error	1.0 ms
Typical processing speed	8 rad/s
Typical positioning speed	18 rad/s

5.1.5   X-Y Scanning Device

The X-Y positional placement of the laser beam was accomplished by the deflection of the input laser beam by two galvanometer mirrors. These mirrors reflect the laser allowing different positions to be selected when combined with the Fθ lens. A generalized schematic of this is shown in Figure 58. The incident beam intersects the first mirror that deflects the beam to the second mirror that is larger than the first mirror. The net angle between the two mirrors then exits the scan head. The galvanometer system used in this set up is an IntelliSCAN 14 built by Scan Lab. The technical specifications of the IntelliSCAN 14 are given in Table 8.
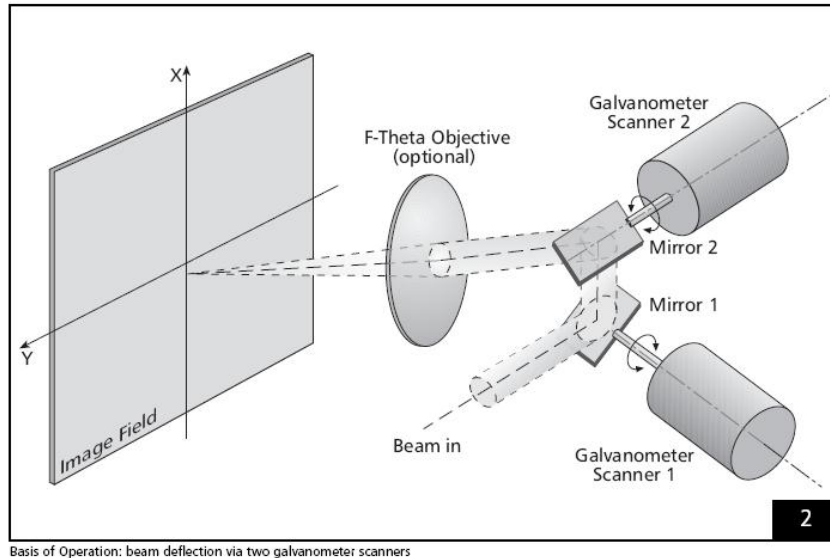
Figure 58 Galvanometer X-Y Scanning system (117)

Table 8 Performance Characteristics of the IntelliSCAN 14

Dynamic Performance (after warm-up)	
Repeatability	< 22 µrad
Long-term drift over 8 hours	< 0.6 mrad
Optical Performance	
Scan Rate	42 rad/s
Typical Scan angle	±0.35 rad
Gain Error	< 5 mrad
Zero Offset	< 5 mrad
Nonlinearity	< 3.5 mrad

5.1.6   F Theta Lens

The mechanical specification of the Fθ lens used in the system is shown in Figure 59. The Fθ lens used in combination with the galvanometer mirror system is a Sill Optic S4 LFT 0055/126. This lens is designed for 1064nm and has a focal length of 59.69mm. The lens has a working field of 19 mm. The lens is also designed to have a back focal

length of 66.21. Because of the 14mm aperture in combination with this lens, the focal

spot of the laser is expected to be approximately 11 microns FW1/e^2.
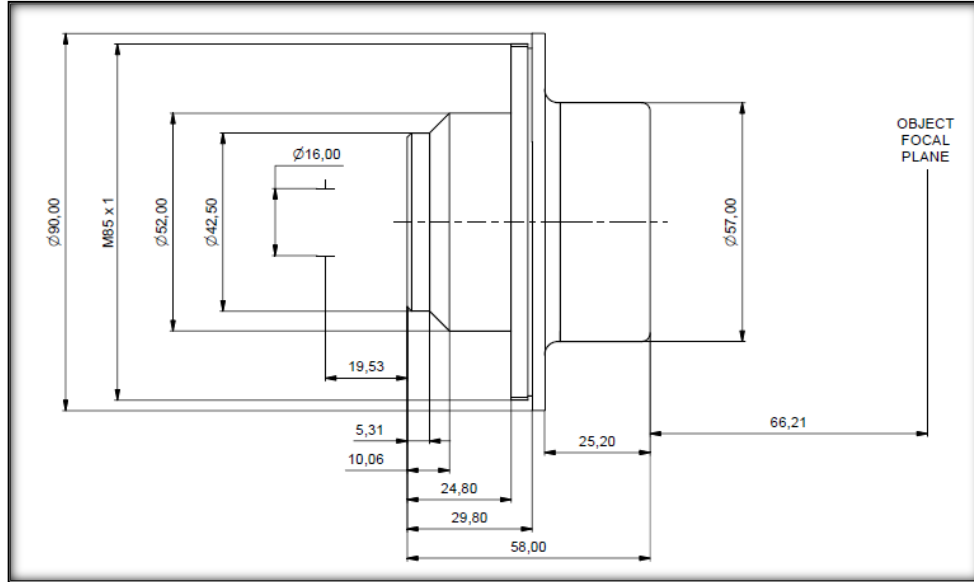
Figure 59 Sill Optic S4 LFT 0055/126

5.2   Surgical Camera System

A coaxial camera system is used to periodically monitor the progression of the

laser surgery. This camera consists of an imaging optic with a 1X afocal that is used to

relay the stop of the f-theta lens to the stop of the camera system. The camera used in the

system is an Adimec 1000m camera with a 25mm fixed focus lens, Edmund Optic NT56-

529, with a custom afocal. The afocal is designed to relay the stop of the Sill Optic to the

stop of the camera lens.

5.3   Beam Directing System

Focusing a laser into the eye accurately, presents a challenge. As reported in

Chapter 2, the anterior segment of the eye is different from eye to eye. To overcome this

problem a calibrated off axis camera\slit laser system was developed. The components

making up this system are an off axis slit laser, Schäfter + Kirchhoff 13LTM-250-41-

90CM-M60-780-9-H06-C-1, a camera system composed of a Navitar 100 lens and

Adimec 1000m camera, a Newport 426 linear stage, a computer controlled ESP 300, a

Newport HS-LTA actuator, and several mirrors (118). This system is based around a slit

laser scanning across the eye, using the mechanized stage, while the off axis camera

collects images of the eye. Prior to conducting a scan, the image volume and the slit laser

angle are determined. To determine the imaging volume, an array of points is moved

along the laser axis. The points where each dot comes from is mapped into the camera

system software. This allows z position in the field to be determined from looking at an

image.   The system does this by ray tracing from the point of interest to sensor. Because
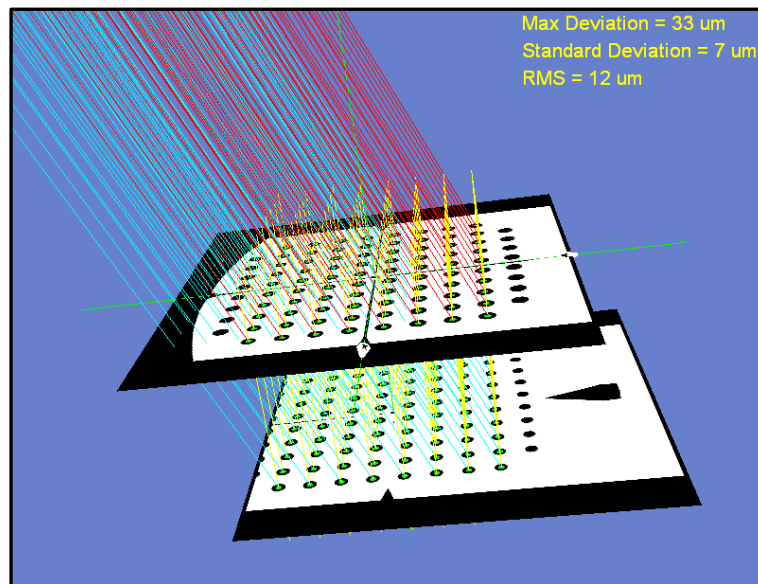
Figure 60 Calibration Image for Slit Laser Camera System

the effective axial position is known from the calibration image, the z position of an

object in the field can be determined. Assuming that one plane at a time is considered.

The slit laser is used to illuminate a cross section of the eye. A typical image of a porcine

eye taken by the combination of slit laser and camera system is shown in Figure 61 (a).

Here the indicator marks are shown marking the anterior lens and the reference glass.

The index of refraction is known to first order for the reference glass, cornea and anterior

chamber. The location of the lens radius of curvature and axial depth can be located by

ray tracing from the lens to where the slit laser crosses the reference glass. By taking

several images across the eye, a three dimension map of lens location can be generated as

shown in Figure 61 (b) (118). This three dimensional information can be used to direct

where the main laser targets. This ensures the effectiveness of the laser in treating the

lens.
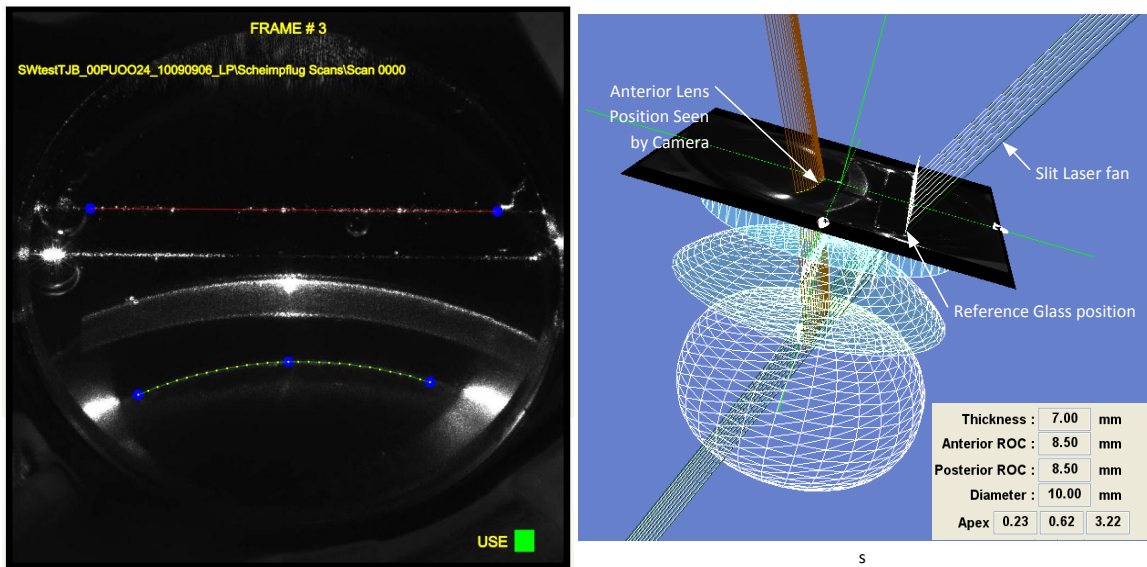
Figure 61 (a) Typical scanned image from slit laser camera system. (b) Reconstruction of depth of the lens from bottom of reference glass.

5.4 System Performance

The overall system is necessary to be able to accurately place laser pulses across the boundary of the anterior lens. This requires the components outlined in the previous section. For the system to work, the accuracy of each of the various subsystems must be high. The errors introduced by each subsystem will affect the efficiency of the laser system when treating the capsule and lens. In the next sections, the accuracy of each of the subsystems and the system as whole are reviewed.

5.4.1 Main Laser System

The main laser system is used to cut the lens. It is important for the various attributes of the laser to be known. The parameters that are reported here are the laser spot at focus, the Z placement accuracy using the VarioSCAN20i, the focal spot to focal spot placement and the line to line placement of the focal spot.

5.4.1.1 Laser Focus

Laser focus was found by focusing the laser onto a piece of functional glass that was imaged using a microscope system. A piece of Sumita's YAG glass was placed at the focus of the main laser system. This glass converts the 1064nm to 550nm. A CVI\Melles Griot 10x objective, PN 04 OAI 001, was focused on the laser incident side of the YAG Glass marked focal plan in Figure 62**.** The converted light acts like a source which is imaged to the calibrated CCD Camera, Ophir\Spiricon 620U camera system. This image is controlled by the Ophir\Spiricon LBA-USB software, version 4.88. The camera software was used to collect an image of the laser spot. The FWHM diameter of the beam was measured to be 55 microns as shown in Figure 63. When the magnification

of the microscope system, 9.32x, is taken into account the FWHM beam diameter is 5.901 μm. The corresponding $1/e^2$ diameter is 10.024 μm. This value corresponds to a system F # of approximately 3.9. This low value can be attributed to the overfill of the VarioSCAN20i by 0.5mm
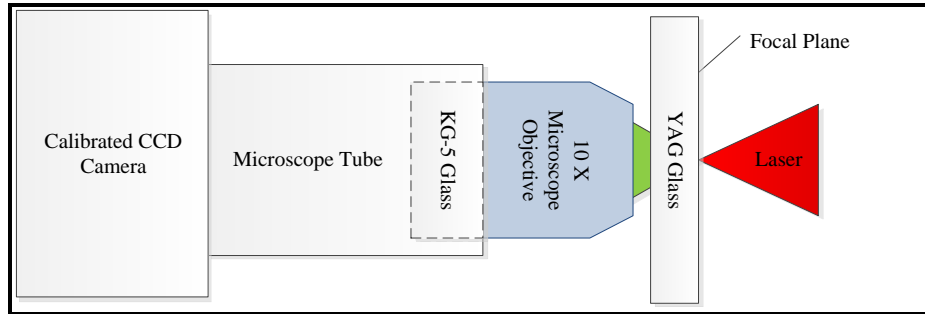
Figure 62 Tool used to measure laser focus
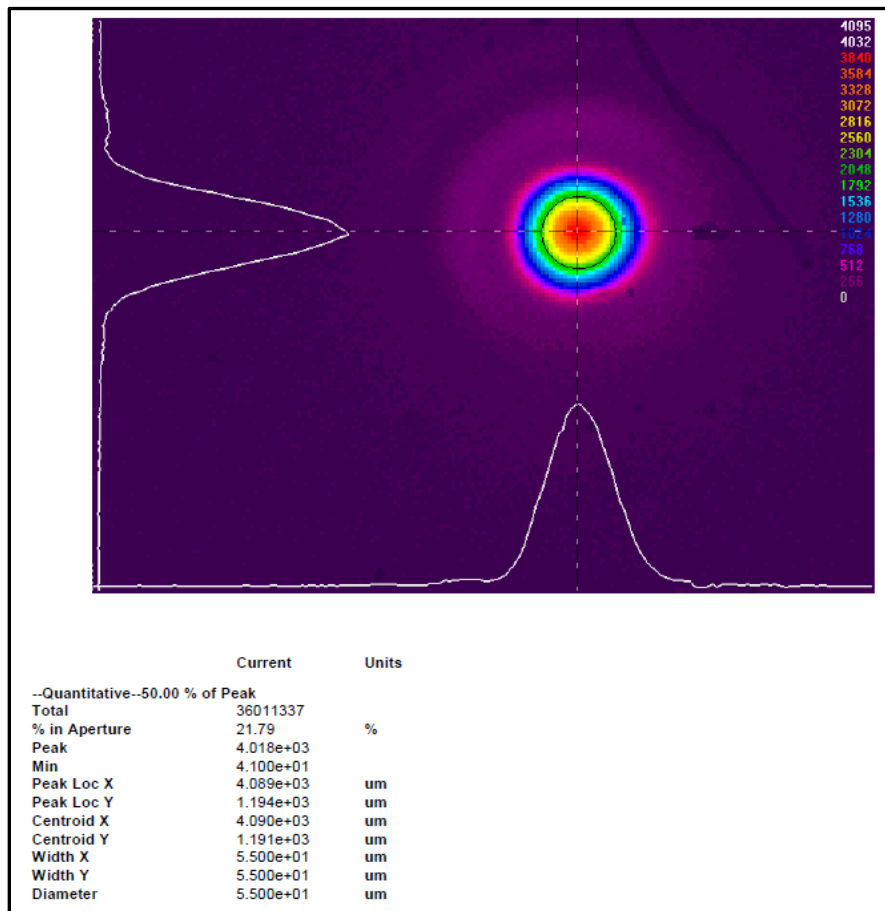
Figure 63 Measured system focus spot measured using a 9.32x magnification system.

5.4.2 Axial focus placement by VarioSCAN20i

The VarioSCAN20i was tested using the focus tool of Figure 62 in combination with a Newport 426 linear stage and a computer controlled Newport LTA-HS micrometer. The focus tool was positioned to find the laser focus for a given focus position command. The range examined was from nominal focus to a position 2.5mm above focus, towards the f-theta lens, and down 4 mm, away from the f theta lens. The performance of the varioSCAN20i is presented in Figure 64. Figure 64(a) is the commanded focal position versus measured focal position. The focal position was determined adjusting the laser focus tool to determine best focus for a commanded focal position. The error in position is shown in Figure 64 (b). The varioSCAN20i had a focal positional error that is less than 10 microns.
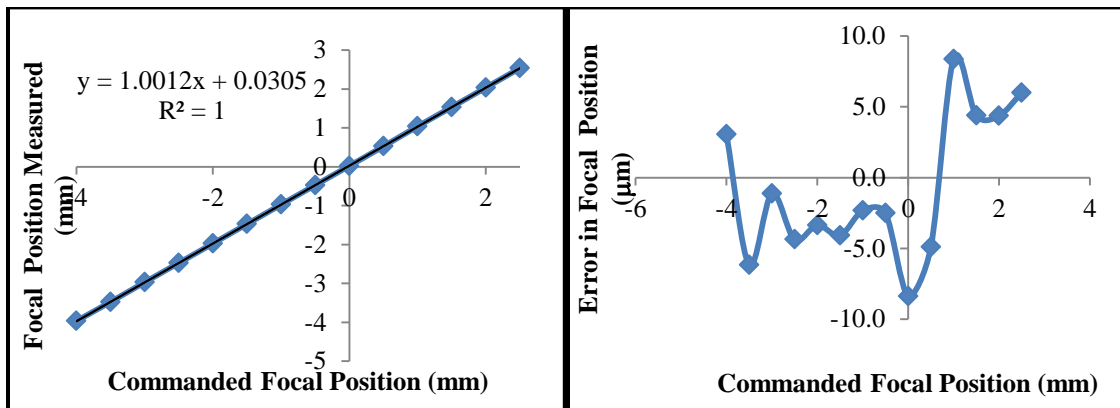
Figure 64 VarioSCAN20i Commanded versus Measured Focal Position. (b) Error in Focal Position

5.4.3 X-Y placement of laser pulses

To determine the focal spot to focal spot placement accuracy and the line to line spacing accuracy, plastic acrylic blocks were used. A series of radial rings we photodisrupted into the acrylic at approximately 5.07 J/cm^2. A magnified image of the

photodisrupted spots in the acrylic block was taken using microscope.   20 successive

photodisruption points were selected in the image collected. The centroids of each of

these photodisruption points were then determined using an image processing algorithm

in MATLAB as shown in Figure 65. The MATLAB algorithm applied a user defined

threshold condition to determine where the spots resided in the image. Prior to collecting

the images, the scaling constant for the magnified image was determined. It was found to

be 0.351 μm/pixel. The pixel centroid location in the image was converted into

measurement centroid location. The distance between successive focal spots was then

determined. The average distance for a 25 μm commanded focal spot separation was

found to be 24.74 μm with a standard deviation of 0.79 microns. This data represents the

limit for accurate focal shot placement for the laser system.
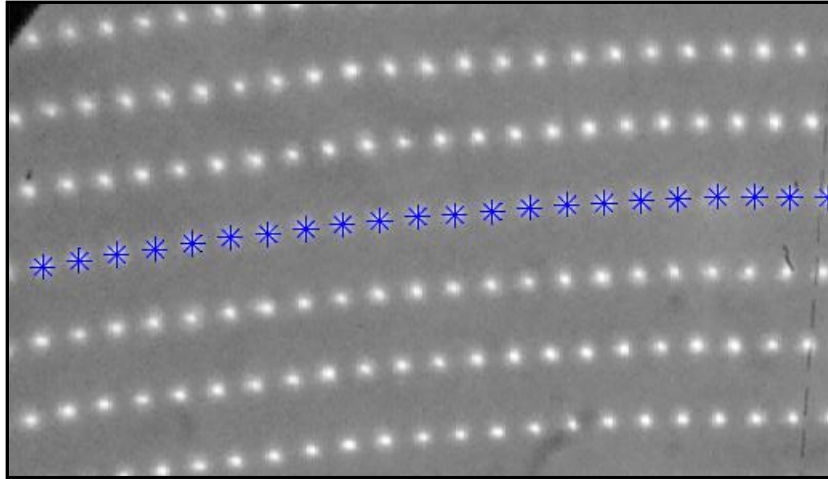
Figure 65 Focal spot to focal spot spacing in acrylic. Commanded focal spot spacing
was 25 microns average focal spot spacing measured was 24.74 microns.

To determine the line to line spacing a similar algorithm was used to find the

location of the individual focal spots on a line. This was done for 15 lines shown in

Figure 66. For each line, a least squares fit circle was determined based on the centroid

locations. The difference between the radii of successive circles was then calculated. For a commanded 50 μm line separation, a measured average of 50.53 μm line separation was found. The standard deviation for this average was 0.92 microns. The results these measurements represent the limit of accurate feature placement for the laser system. Based on the data collected the laser focal spot location is expected to be within a few microns of the intended location.
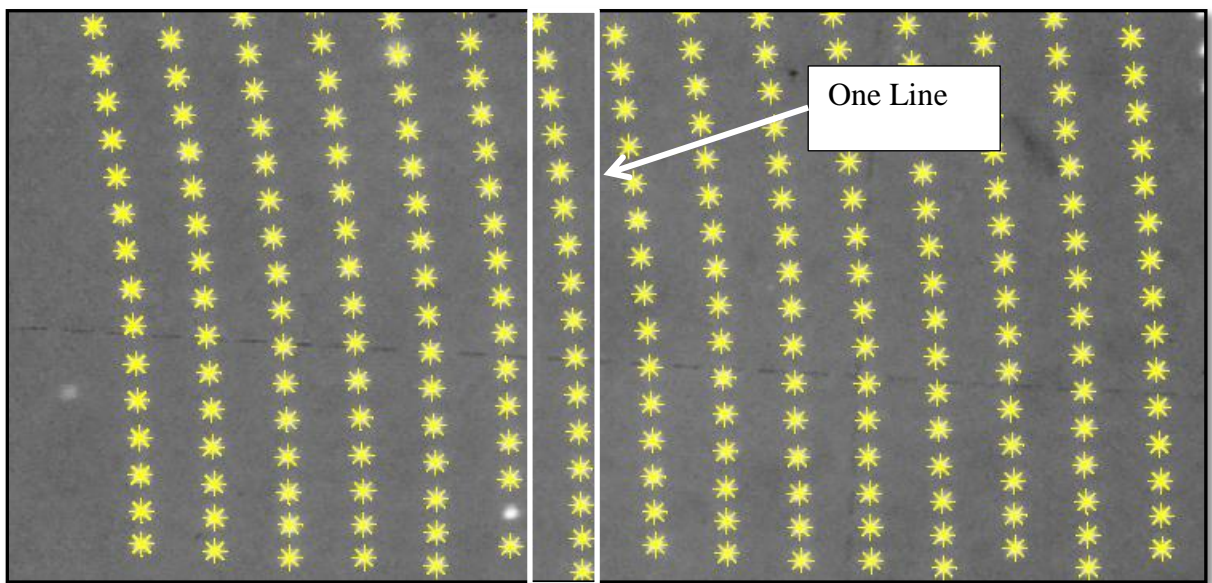
Figure 66 Line Spacing Image in acrylic. Commanded shot spacing was 50 microns average shot spacing measured was 50.53 microns

5.4.4   Accuracy of Slit laser Camera Measurements

To determine the accuracy of the slit laser camera system, a plano-convex lens was used. The lens was Edmund Optics' 45-083. The 45-083 has a radius of curvature of 9.34mm. The lens was placed under the slit laser camera system and scanned at various positions. Once the scans were completed, the location of the lens was determined by the system using a 3D reconstruction algorithm. The positions that were measured are given in Table 9labeled micrometer set position.

117

The testing process initially put the lens in contact with the reference glass and then slowly moved the lens away. Once the lens was 3mm away from the reference glass, the lens would be measured for different displacements about the center position. A typical displacement pattern is shown in Figure 67 for the -4.00 mm position. Once scanned, the system determined the 3D position of the apex of the lens under the system. This was the position of the lens that was closest to the system. The micrometer set position minus the system reconstructed position was calculated to determine the error in the measured lens position. Table 9 shows the results of these measurements. The table indicates that the error in the y axis is much greater than the error in the x axis. This is because the slit laser travels across the lens on the y axis. There are fewer data points to fit in this axis than are available in the x axis. The positional error data for the slit laser/camera shows the limit to which the lens position is known with respect to the system.
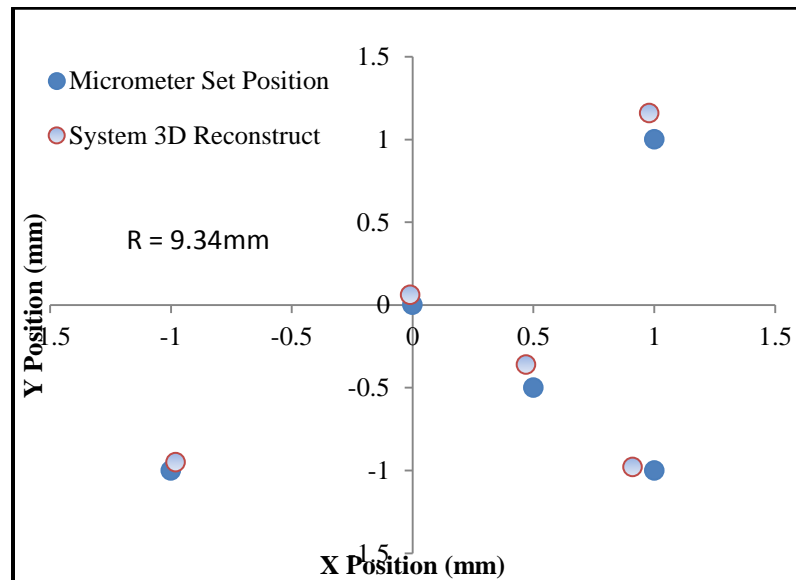
Figure 67 Measured versus Set position at -4mm below reference glass for a lens with radius of curvature of 9.34mm

Table 9 Error is measurement for X, Y, Z, and Radius of Curvature of a 9.34mm lens

Micrometer Set Position			System 3D Reconstruct				Difference			
(mm)			(mm)				(mm)			
x	y	z	x	y	z	R	Δx_{m3D}	Δy_{m3D}	Δz_{m3D}	ΔR_{m3D}
0	0.00	0.00	0.00	0.07	0.02	9.58	0.00	-0.07	-0.02	9.58
0	0.00	1.00	-0.03	-0.03	0.97	9.31	0.03	0.03	0.03	9.31
0	0.00	2.00	0.00	-0.06	1.99	9.43	0.00	0.06	0.01	9.43
0	0.00	3.00	0.00	-0.50	2.98	9.52	0.00	0.50	0.02	9.52
-1	0.00	3.00	-1.01	-0.01	2.98	9.49	0.01	0.01	0.02	9.49
-1	-1.00	3.00	-1.02	-0.93	2.97	9.74	0.02	-0.07	0.03	9.74
0.5	-0.50	3.00	0.43	-0.48	2.97	9.19	0.07	-0.02	0.03	9.19
1	-1.00	3.00	0.97	-1.06	2.95	9.40	0.03	0.06	0.05	9.40
0	0.00	4.00	-0.01	-0.04	3.96	9.24	0.01	0.04	0.04	9.24
-1	-1.00	4.00	-0.98	-1.15	3.94	9.10	-0.02	0.15	0.06	9.10
1	1.00	4.00	0.98	0.82	3.97	9.19	0.02	0.18	0.03	9.19
0.5	-0.50	4.00	0.47	-0.60	3.94	9.15	0.03	0.10	0.06	9.15
1	-1.00	4.00	0.91	-1.12	3.91	9.09	0.09	0.12	0.09	9.09
-1	-1.00	5.00	-1.05	-0.88	5.00	9.53	0.05	-0.12	0.00	9.53
1	1.00	5.00	0.91	0.82	4.99	8.96	0.09	0.18	0.01	8.96
0.5	-0.50	5.00	0.43	-0.28	4.97	9.05	0.07	-0.22	0.03	9.05
1	-1.00	5.00	0.92	-1.00	4.94	9.35	0.08	0.00	0.06	9.35
Lens Radius of Curvature			9.34	mm	Average Err		0.03	0.05	0.03	0.04
					Stdev		0.03	0.16	0.03	0.22

5.4.5   Overall System Performance

To validate the entire system, a test shot pattern shown in Figure 68 was

photodisrupted in porcine eyes. The lens was then dissected out of the porcine eye and

the position of the pattern was tested using an E-Technologies MHF-1 B-Scan system.

119

The relative position of the photodisruption pattern was measured using the B scan, (Figure 68(b)). From these experiments it was determined that the focal spot placement was within 100 microns of the desired location in the lens. The accuracy of the B-Scan limits accuracy of the measurement to 100 microns. This is adequate for experiments that were conducted and documented in the next chapters.
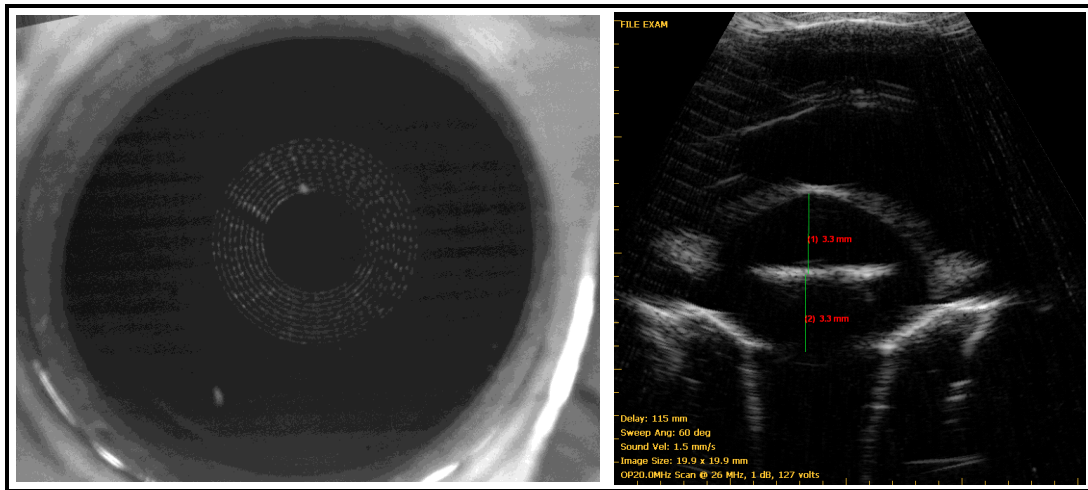
Figure 68 (a) Sample pattern created in a porcine eye. (b) Ring pattern location in lens.

5.5   Summary and Conclusions

In this chapter, the laser system that is necessary to process the lens was presented. The requirements for this laser system were driven by variability in potential patient eyes. The laser system was defined as needing to move over a 3 dimensional volume. The laser system also needed to be able to position the laser based upon data from a beam directing system.

It was found that the standard deviation in error of the focal spot to focal spot placement of the laser was 0.79 microns whereas the line spacing standard deviation in error was approximately 0.92 microns. The maximum error in the z axis was less than 10

microns. The largest subsystem that contributes to the system error was the scanning slit laser\ camera system. The z average error in position was 30 microns for the 9.34 mm lens with a standard deviation of 30 microns. This requires treatment with at least a 200 micron of length to treat 95% of all eyes just for the z error component. This is complicated by the uncertainty in the positional placement of the eye and any tilt that the eye may have, docked with the system. Table 8 shows that the standard deviation of the y positional area was 160 microns. Three times this number is the 95th percentile for the error in the y axis measurement. This corresponds to a positional error in laser placement of 480 microns. Any positional error (Figure 69) results in the need for an edge height for the treatment laser. The edge height required depends on the radius of curvature of the lens. The nominal pig eye has a radius of curvature of 7 to 9mm. Table 10 shows the treatment height required for different x-y positional errors. From inspection of Table 10, the edge height required for treatment, if not adjusted for every eye, needs to be a millimeter or more. This will ensure that the laser interacts with the capsule for each treatment.

In summary, the accuracy of the various subsystems limits the minimum interaction that the laser can have with the lens and be effective treating it. It was determined that the biggest contributor to the error in laser beam placement was the Beam Directing System. This system was limited by the way that the y axis data is collected.
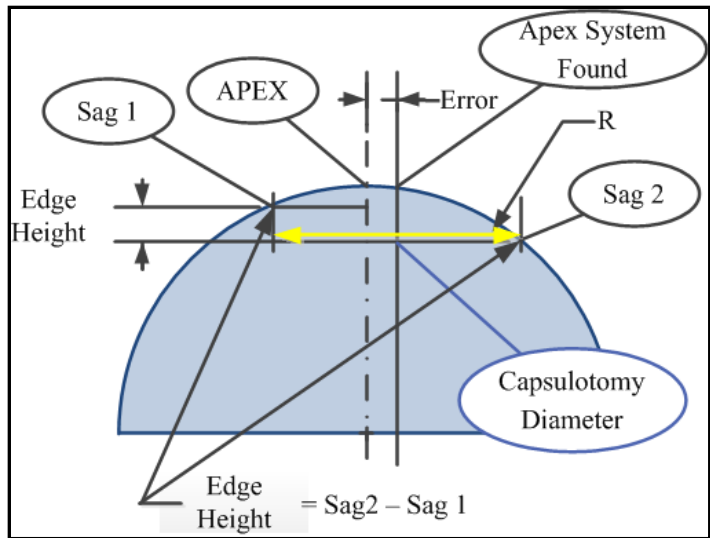
Figure 69 Edge Height results from positional error in apex location.

Table 10 Axial treatment length versus lateral radial error in position

Capsulotomy Parameter			Color Bar Flex Points				Green	Yellow	Red
					Less than	50%	99%	100 %
Diameter	5.3	mm							
Edge Height	1	mm							

Lens Radius (mm)	7	7.2	7.4	7.6	7.8	8	8.2	8.4	8.6	8.8	9
Radial Distance Error (mm)	Sag Difference (Min Thickness needed to be treated) (mm)										
0	0.00	0.00	0.00	0.00	0.00	0.00	0.00	0.00	0.00	0.00	0.00
0.1	0.23	0.21	0.20	0.19	0.18	0.17	0.17	0.16	0.15	0.15	0.14
0.2	0.45	0.43	0.40	0.38	0.36	0.35	0.33	0.32	0.31	0.30	0.29
0.3	0.68	0.64	0.61	0.57	0.55	0.52	0.50	0.48	0.46	0.45	0.43
0.4	0.92	0.86	0.81	0.77	0.73	0.70	0.67	0.64	0.62	0.60	0.58
0.5	1.15	1.08	1.02	0.96	0.92	0.88	0.84	0.80	0.77	0.75	0.72
0.6	1.39	1.30	1.22	1.16	1.10	1.05	1.01	0.97	0.93	0.90	0.87
0.7	1.63	1.53	1.44	1.36	1.29	1.23	1.18	1.13	1.09	1.05	1.01

CHAPTER 6 STUDY OF PHOTODISRUPTION IN WATER AND GELATIN

In Chapter 2, the anterior chamber of the eye was described as being filled with a fluid, the aqueous humor. The aqueous humor is physiologically balanced electrolyte solution. The lens is well defined with a high degree of regularity to the architectural arrangement of the fibrils surrounded by an epithelium on the anterior surface and a thin collagenous capsule. These two regions, the aqueous humor and the transparent cell mass of the lens, represent two distinctly different transparent materials which are in close proximity to each other and separated by the lens capsule. The fluid of the aqueous humor is free to flow throughout the anterior chamber. When a photodisruption event occurs in the anterior chamber, the oxygen bubble that forms from the breakdown of the fluid can move away from the photodisruption site. A photodisruption events occurring in the lens are different because of the lens architecture. A localized photodisruption produces a bubble that remains trapped at the site of the event within in the lens. In this chapter, two materials are examined that were used to model the expected behavior of photodisruption near and at the anterior of the lens. The first model material was water. This model was used to study the expected behavior of photodisruption in the anterior chamber. The second model material was gelatin. This model was used to study the effects of photodisruption in the lens.

6.1   The use of Gelatin as a Model for the Lens

Gelatin is a protein that is produced out of the partial hydrolysis of collagen. It is extracted from the connective tissues of animals such as bone and skin (119). Gelatin is composed of Type I collagen with trace amounts of Type II collagen. When mixed with water gelatin forms a colloid gel. Gelatin has a chemical composition similar to collagen (120). Gelatin contains 14% hydroxyproline, 16 % proline and 26 % glycine. This is very similar to its parent protein, collagen (121). For this reason, gelatin is a good surrogate proteinaceous material to model the lens. Although the exact structure is not the same as the lens, the constituents making up the gel are similar to the material of the eye. The nominal index of refraction of gelatin is 1.39, which is similar to the lens. The behavior of the gelatin when a photodisruption event occurs provides a response similar to the fibrous mass of the lens.

6.2   Goals of the Experiments

The goal of these studies was to study the effect of photodisruption in the model materials of the eye. These materials represent the anterior chamber and the lens. The study of the photodisruption process was used to guide the selection of laser parameters for *ex vivo* testing porcine eyes. The phenomena studied in water and gelatin included the variation of photodisruption length and the width of the photodisruption with fluence level, and the radius of the shock wave with fluence level. Additionally, in gelatin the evolution of the photodisruption bubble was studied. Since the latter is trapped in the gelatin, its evolution over longer periods of time can be examined.

6.3   Experimental Method

The principal method of study of the interaction was the use of high speed time-resolved, high resolution optical imaging with a synchronized visible backlighting laser beam. The backlighting laser beam generated from the output of the photodisruption laser had a delay of 9.7 ns from the main laser pulse. By controlling the X-Y scanner of the laser system an extended period of time could be evaluated. The laser and the two dimensional (x-y) scanning system used are described in Chapter 5. Figure 57 in Chapter 5 shows the details of the irradiation system.

To study the evolution of the laser interaction with water or gelatin, an experiment was setup that backlit the photodisruption in a cuvette filled with either water or gelatin. The X-Y scanning capabilities of the laser system discussed in Chapter 5 were used to place a series of laser pulses into a filled cuvette. The cuvette contained either gelatin or water. The laser was focused into the cuvette from above. The laser system was modified to include an optically delayed frequency doubled path that backlit the laser interaction approximately 9.7 ns after the laser pulse was focused in the test cuvette. Figure 70 shows the experimental set up. The camera system was timed to be triggered when the back light pulse illuminated the test cuvette.

This process was done for multiple laser fluence levels focused in the cuvette. The galvanometer mirrors were scanned to place the laser pulses approximate 50 to 100 microns apart depending on the laser fluence. Their speed was adjusted depending on the frequency of the experiment. The laser fluence levels uses to study the interactions ranged from 5.1 J/cm^2 to 57.0 J/cm^2. To study the length and width of the photodisruption and shock wave, an electronic delay that triggered off of a laser pulse

was used. To study the evolution of the characteristic photodisruption bubble, 10 pulses were used at frequency of 100 kHz. This allowed the evolution of the gas bubble to be examined. This spans a large range of possible laser frequencies that could be used for capsulotomy. In the next sections, more details of the experiment are discussed..
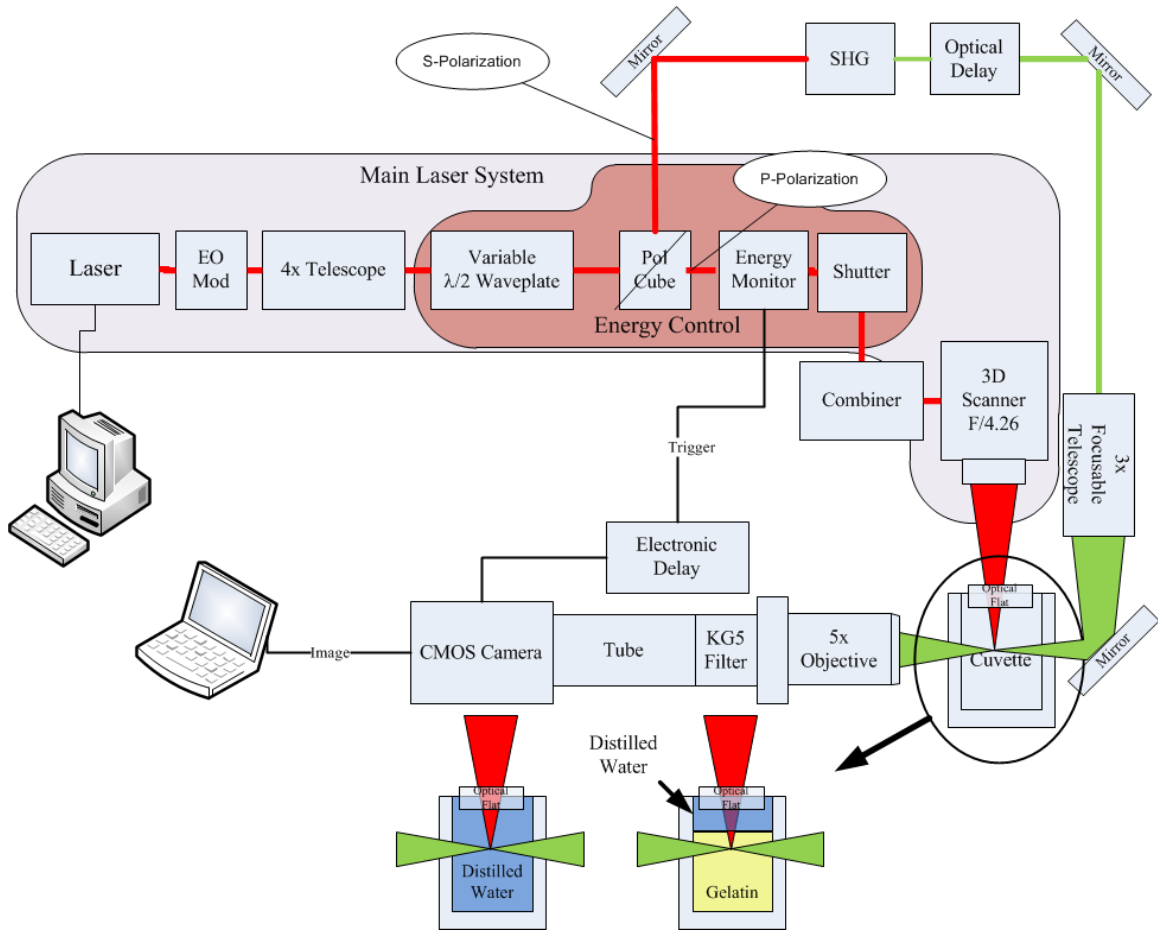
Figure 70 Experimental set up used to collect the photodisruption imagery.

6.3.1 Sample Preparation

Samples were prepared by either filling the test cuvettes, Starna Cell 96F-G-20, with distilled water or gelatin. The gelatin samples were made using Knox unflavored gelatin. The samples were prepared in a beaker following the instructions on the package 7 g of Knox gelatin was mixed with 100 ml of boiling water. This was then combined

with 150 ml of 25°C water. Once the gelatin was combined, it was poured into cuvettes and allowed to cure overnight at room temperature. Prior to pouring the gelatin into the cuvettes, the cuvettes were treated with rain-x glass treatment (122) to reduce the surface tension between the gelatin and glass of the cuvette. This allowed the samples to cure with a flatter central zone than untreated cells. To minimize the effects of any residual curvature of on surface of the gelatin, distilled water was placed on top of the gelatin as shown in Figure 71. A fuse silica window was placed into the water bath to provide an optically flat surface for the laser.
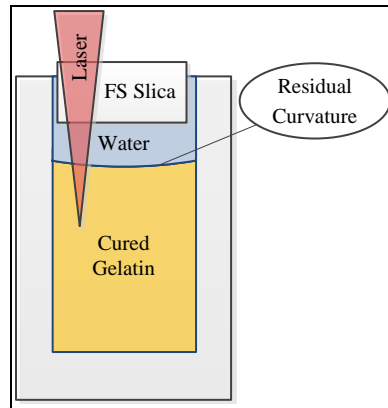
Figure 71 Interface technique for putting laser pulses in gelatin

6.3.2   Optically Backlighting Illumination

To illuminate the laser pulse interaction in the sample, an optically delayed frequency doubled second harmonic generated (SHG) pulse was generated from the s-polarization beam of the laser system shown in Figure 70. This beam is the complement of the main laser beam that treats the eye.   This was done by removing the beam dump of the laser and folding the beam into the SHG Crystal. The intensity of the SHG beam varied corresponding to the laser fluence set point for primary channel of the laser used to cause photodisruptions in the eye. The SHG Crystal is an 8x8x10 mm KTP second

127

harmonic crystal from Quantum Technology Incorporated. This crystal has a conversion

efficiency of 60%. The SHG beam was directed to a focusable 3x telescope (Newport

T81-3x) and focused into the test cell. The intensity of the SHG changes as a function of

laser set point. The intensity varied from 40 to 14 W/cm^2. To compensate for the change

in illumination of the test cell, the location of focus of the 3x telescope was adjusted to

control the intensity on the Pixel Link 741 Camera to not saturate the detector. The

absolute intensity was not critical because of the sensitivity of the camera. The SHG

beam was designed to be perpendicular to the laser pulse coming into the test cuvette.

Figure 72 shows a sample being illuminated from the SHG beam. The laser pulse

causing the photodisruption is incident from above the test cuvette. The sample is

illuminated by the SHG path.
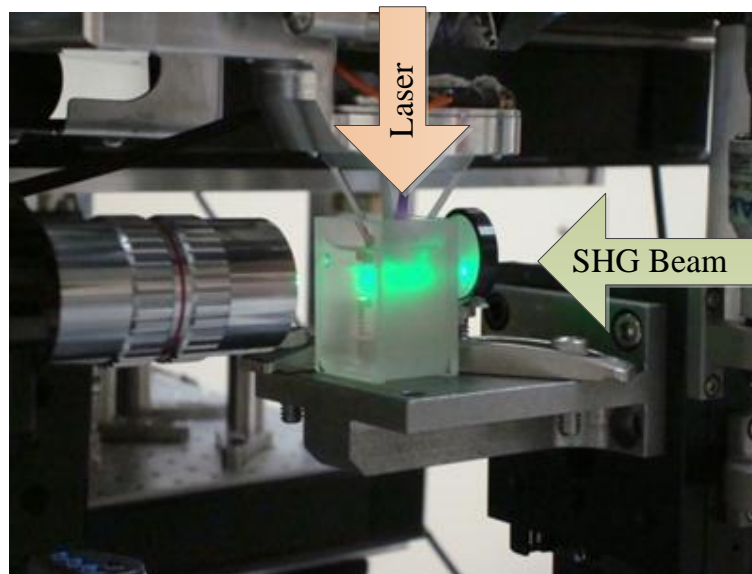
Figure 72 Image of the Gelatin cell being illuminated by the SHG green beam.

6.3.3   Imaging System

To image the photodisruption, a long working distance microscope system was

used. The system consisted of a CMOS camera (Pixelink B741) integrated with an

infinity microscope tube system (Edmund Optics 54-590) and 5x infinity corrected

objective (Edmund Optics 59-876) and a KG5 Filter (Edmund Optics 45-646). The KG5

filter eliminated any residual 1064 nm energy that was transmitted through the optically

backlit path. The system had a field of view of 1.76mm x 1.32mm and an optical

resolution of 2.68 microns.

6.3.4   Camera Timing

To collect images of the photodisruption interaction with the water, a delay circuit

was used consisting of a Stanford Research Systems DG645 electronic delay generator

and the energy monitor in the main laser path. The energy monitor described in Chapter

5 was used to supply a trigger source to delay line. The laser trigger was not used because

the EO modulator in the system blocks the first few high energy pulses prior to allowing

pulses to propagate to the target. The energy monitor would sense the first pulse and

trigger the electronic delay generator as shown schematically in Figure 73. The

electronic delay generator would wait for the desired time delay that corresponded to a

set number of pulses. The delay was 75 μs for the 20 kHz tests and 80μs for the 100 kHz

tests. It then would start the integration of Pixelink B741 camera by outputting a TTL

high signal. The camera would integrate until after the SHG pulse passed. The

integration period was set to 25 μs. At the end of the desired integration period, the

electronic delay would send a TTL low signal to command the camera to stop integrating.
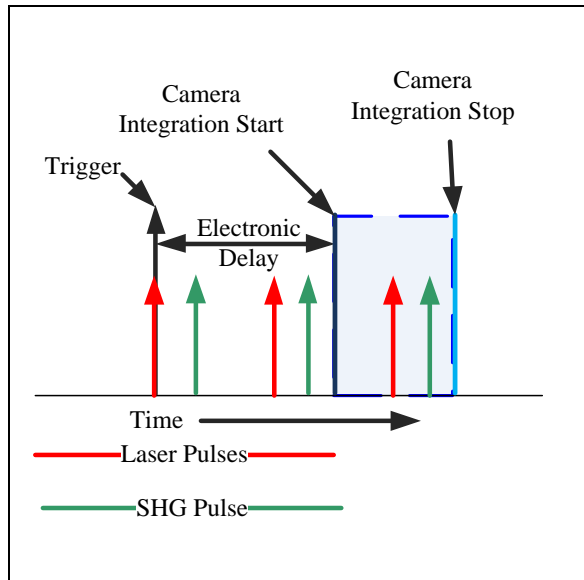
Figure 73 Schematic of the timing technique used to control the integration of the camera

6.3.5   Image Analysis

The images collected by the camera system were analyzed to determine the characteristics of the photodisruption interaction with the material. The images were first imported into Microsoft Visio where the length of the laser interaction column was measured. The images were scaled using the distance between the two photodisruption sites observed in the gelatin. The focused positional accuracy of the pulse placement of the system was within a micron of intended beam placement. . A sample measurement is shown in Figure 74. For water, a target with 100 micron graduations was placed in the cuvette of water and imaged using the camera system described in 6.3.3 Imaging System. The midpoint of the column was then selected and measured to determine the width of the laser interaction. The width of the shock wave was then measured at the midpoint of the laser interaction. From this measurement the radius was determined.
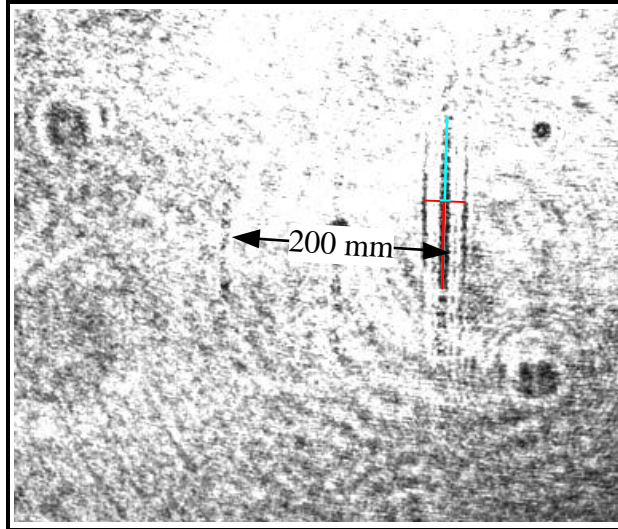
Figure 74 Method of Image Analysis of Laser Interaction

6.4   10ps Laser Interaction for various fluence levels in water

In this section, laser system interaction with water is reported. The length, width,

and shockwave generated by the laser interaction was observed and measured. A cuvette

was filled with the water and placed under the laser system. Interfacing with water in the

cuvette was an optically flat piece of fused silica with refractive index of 1.45. This was

done to ensure that an optically flat interface was made with the water. A series of three

pulses were then focused into the cuvette. Each pulse was separated spatially from the

previous pulse laterally in the x direction. Figure 75 shows this configuration. After

each experiment, the reference glass was raised and lowered in and out of the water to

remove any build-up of oxygen bubbles that deposited on the glass interface as a result of

the laser interaction. The position of the glass was controlled using a micrometer to

ensure consistent placement of the glass interface to the water. The laser interaction was

optically backlit 9.7 ns after the laser pulse focused in the water. As seen in Figure 76

this point in time corresponds to the end of the plasma formation and is in the middle of

the shock wave time period for a photodisruptive pulse.
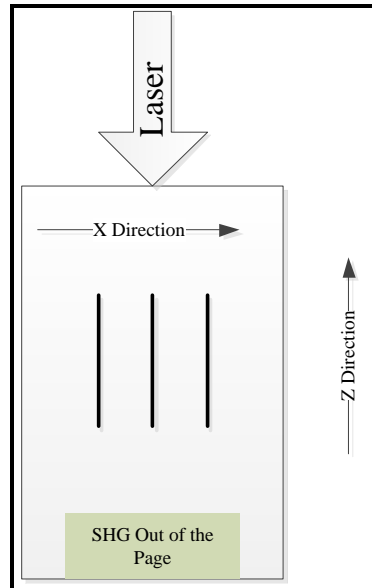
Figure 75 Schematic of three pulses being shot into the cuvette
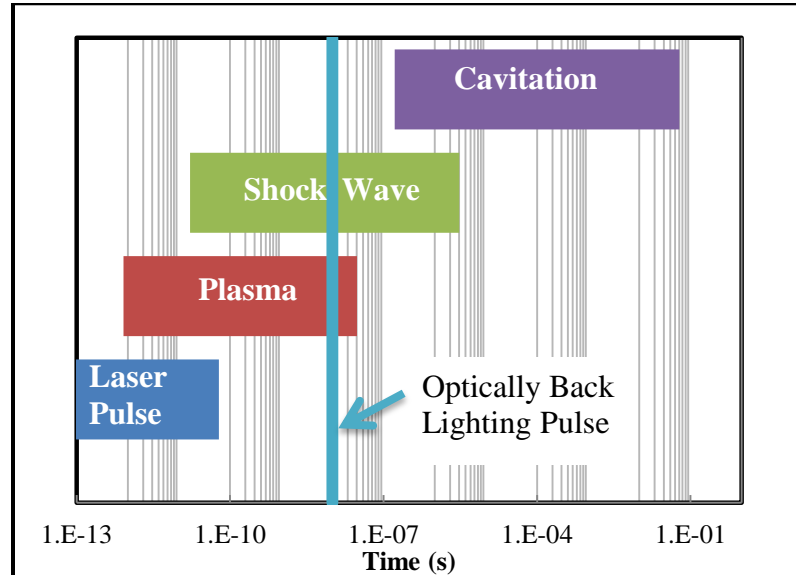
Figure 76 Time point where laser interaction was backlit using the SHG beam. (Adapted from Niemz time evolution of photodisruption (7))

6.5   Threshold of Water

It is important to define some physical parameters that define the onset of disruption in the medium. Ideally it is the point at which the plasma starts. However from a practical point of view, this point cannot be observed with the experimental setup. The most sensitive observation in this study is the irreversible visualization of the photodisruption column. This event is used to define threshold in the medium. This definition is appropriate when considering a laser beam to dissect materials. A beam that does not show evidence of a complete column would not be unacceptable for dissecting the capsule because of the uncertainty in producing a complete cut. Threshold fluence for water was found to be 8.55 J/cm^2. Although evidence of laser interactions are seen at both 8.11 J/cm^2 and 8.23 J/cm^2, at this point the disruption is not considered threshold for cutting because the interaction observed was not consistent with repetition. The peak power of the threshold pulse was 0.594 MW, which is below the self-focusing threshold power reported in Chapter 3, Section 3.2.2 of 2.4 MW. Figure 77 shows images of the laser interaction for these fluence levels. In Figure 77 (c), where threshold has been defined, the interaction length of the photodisruption column is approximately 82 μm.

8.11 J/cm^2
(6.4 µJ)

8.24 J/cm^2
(6.5 µJ)

8.55 J/cm^2
(6.75 µJ)

50 µm
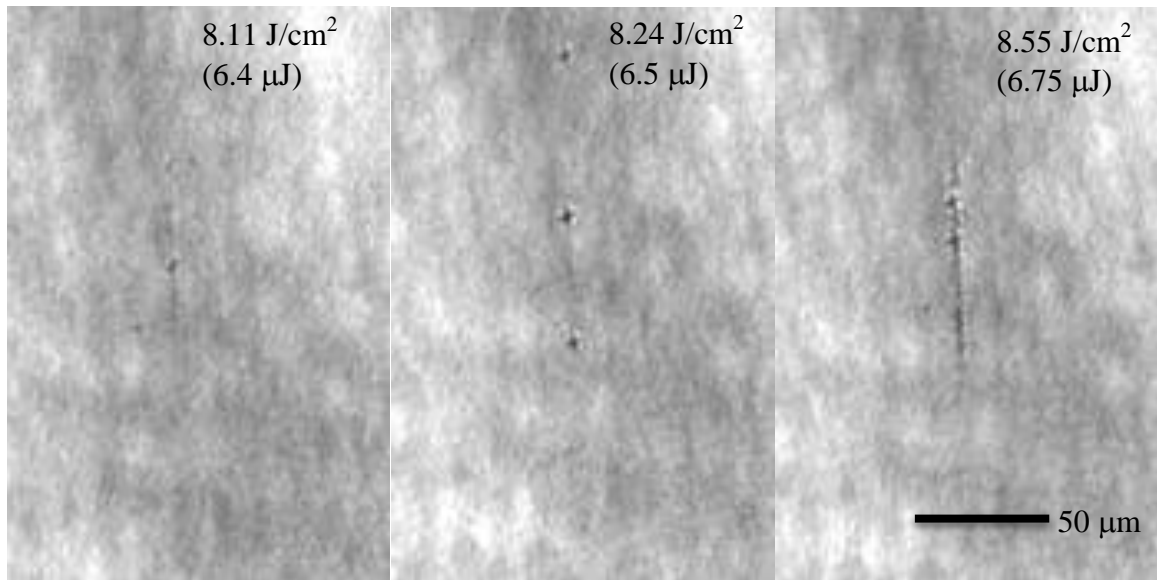
Figure 77 Threshold measurements for 10ps laser system in water measured 9.75 ns after the laser pulse. Threshold is defined in image (c) where a column indicating where the laser has interacted with the water is clearly observed. (a) Shows indications of slight interaction in the water bath and (b) shows the increase of the interaction. The scale for each image is the same.

6.5.1   Effects of increasing fluence in water

To understand the effects of increasing the laser fluence levels above threshold, a study was done to observe the effects of laser pulses of various fluence levels in water. Understanding the effects of increasing fluence levels is important to define the interaction effects in media. In the case of cataracts, the fluence levels necessary to penetrate and cause photodisruption in the lens need to account for losses during the z transit to the focal site of the intended photodisruption. The laser pulses will be attenuated differently for each different grade or type of cataract. This results in a degree of uncertainty in determining the pulse fluence at the photodisruption site in the lens. It is therefore necessary to study a range of fluence levels to ensure that the interaction is well understood. In the case of the capsule being disrupted, the effects of increasing the fluence can reduce the requirement on targeting in the eye or may increase the

requirements depending on the effect of interaction. The effects of generating a shock wave at various fluence levels must be understood to ensure that the cutting of the capsule is effective and does not result in additional unwanted interaction with the capsule. Figure 78 through Figure 80 shows the progression of the laser interaction for various fluence levels, moving to higher fluence levels. From approximately 8.11 J/cm^2 to 8.87 J/cm^2, no shock wave was associated with the laser interaction, this is considered to be the region of plasma-induced ablation as defined by Niemz (7). During the transition from 8.87 J/cm^2 to 10.14 J/cm^2 the first evidence of a structured shock wave was observed. The laser interaction grows as the laser fluence increases as seen in the successive images. As the laser fluence increases the shock wave slowly forms a dome encapsulating the top of the laser interaction forming a bell over the main laser interaction. During the transition from 31.68 J/cm^2 to 38.01 J/cm^2, shown in Figure 80, the bell of the shock wave at the top of the laser interaction is pierced by the main column generated from the plasma. This is due to the onset of self-focusing in the beam. In successive images of the laser interaction for 44.35 J/cm^2 and 50.68 J/cm^2, the shock wave is affected by this phenomenon. A plot of the growth of the laser interaction column is shown in Figure 81. In continuous media the photodisruption main column height can be considered to be the effective treatment length of the laser for various fluence levels. In the plot, the interaction is broken into 3 regions of interest. In the first region on Figure 81, is the region where no shock was observed. In this first set of recorded interactions, the column length was measured to be in the range of 80 μm to 100 μm. In the second region, denoted by the presence of a shock wave radiating radially from the photodisruption column, the laser interaction grew from approximately 170 to

135

400 microns. In the final region where the self-focusing in the photodisruption column pierced the shock wave at the top of the laser interaction, the length grew from 470 to 520 microns. The final measurement, of approximately 520 μm, was at laser pulse fluence of 57.02 J/cm^2. Although the length of the laser interaction grew axially six fold, the width of the main laser interaction and the shock wave generated from the laser interaction did not grow proportionally. The FWHM of the main interaction column measured at threshold was approximately 3.5 μm. When the first shock wave was observed the photodisruption column width grew to approximately 6 microns. The photodisruption column continued to grow until the laser fluence reached about 21.54 J/cm^2. Once this fluence level was reached the width of the FWHM of the photodisruption column maintained a value of approximately 10.5 μm. A plot of the photodisruption column width vs. fluence level is shown in Figure 82. Here the laser pulses, where no shock wave was observed, are shown by diamond shapes. The region where a shock was observed is plotted using circles. Because the pulse width appeared to be approaching 11 microns asymptotically, there was no discrimination between the pulses where a bell was present and the pulses where the bell of the shock wave was pierced by the main interaction column. The shockwave observed was measured for each image. A plot of the shockwave radius is plotted in Figure 83. In the initial images of the laser interaction with water there was no shock wave observed. The shockwave radius grew slowly until it reached the point where the plasma column pierced the bell of the shockwave. Once this point was reached the shockwave radius remained relatively constant, reaching a radius of 20 microns. This corresponds to shockwave velocity of approximately 2100

m/s which is in good agreement with the model describe in Chapter 3 that predicts 2101 m/s at 57.02 J/cm^2.

In summary we have identified three separate regions of laser interaction in water. When disruption first takes place in water there is no observation of a shock wave associated with the disruption. In this region, disruption is caused by the ionization of plasma itself (7). In the second region photodisruption takes place. In this region, optical breakdown is associated with plasma formation and shockwave generation. The third region shows the effects of self-focusing in the beam, and the top of the shock wave is disrupted by the effects of self-focusing.
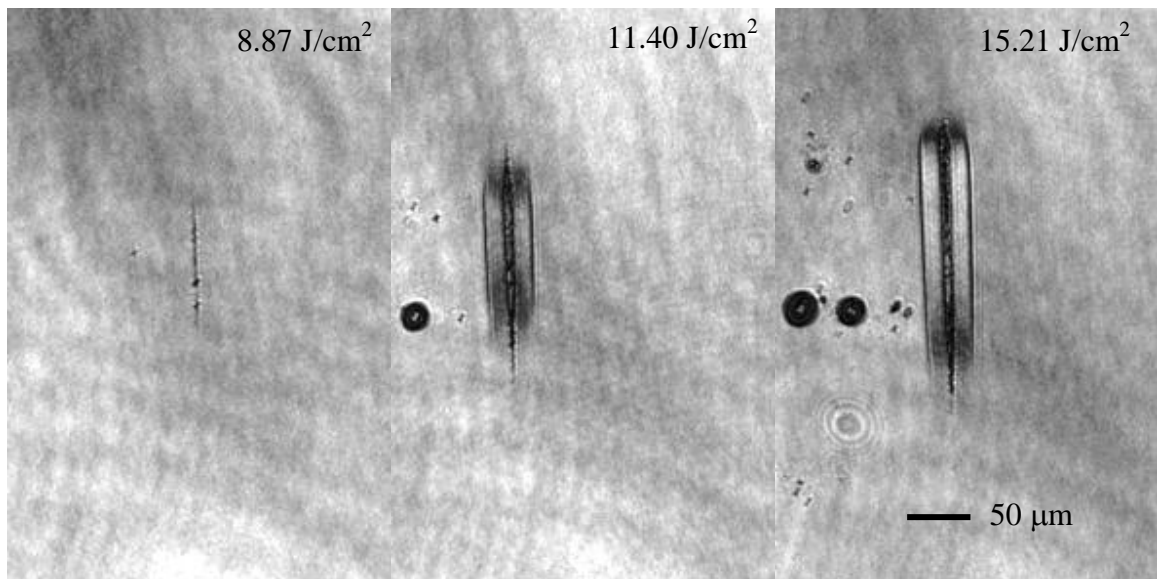
Figure 78 Photodisruption in water for fluence levels of 8.87 J/cm^2 to 15.21 J/cm^2.
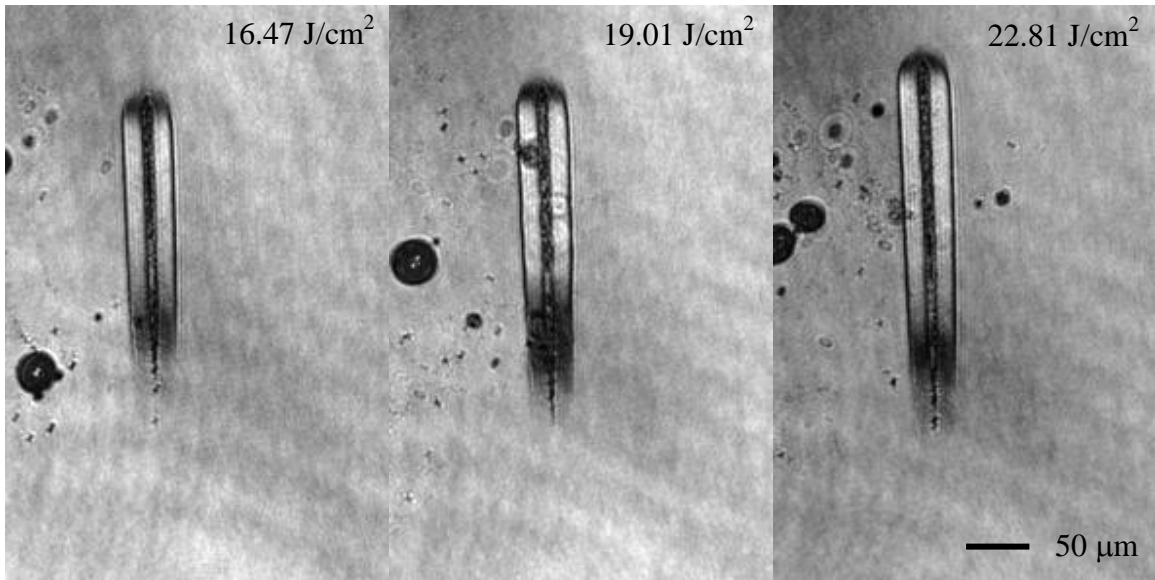
Figure 79 Photodisruption in water for fluence levels of 16.47 J/cm^2 to 22.81 J/cm^2.
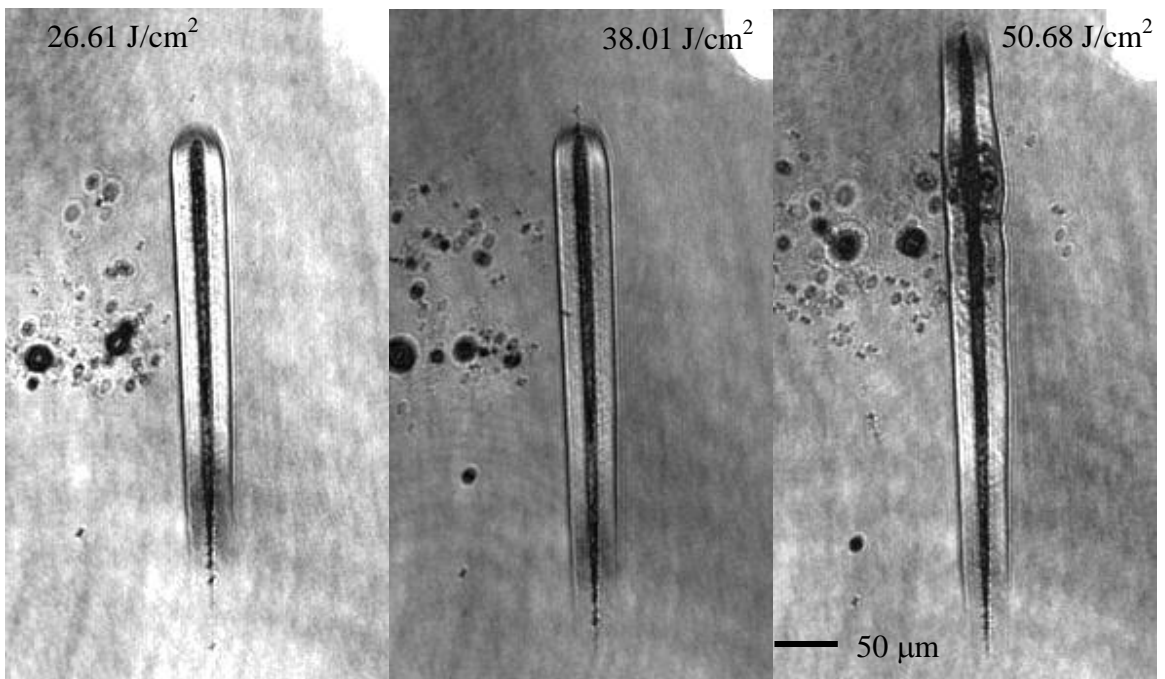
Figure 80 Photodisruption in water for fluence levels of 26.61 J/cm^2 to 50.68 J/cm^2.
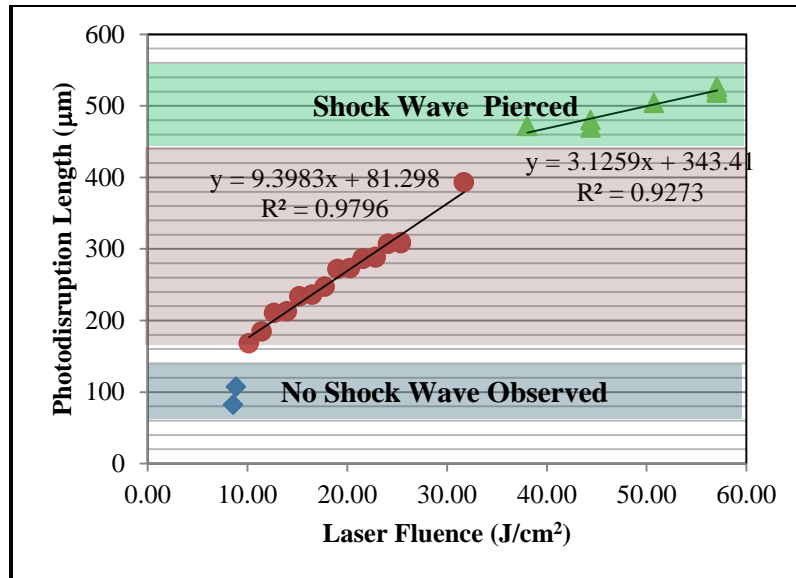
Figure 81 Photodisruption column length in water vs. laser fluence in the three regions observed during experimentation, 9.7 ns after photodisruptive laser pulse.
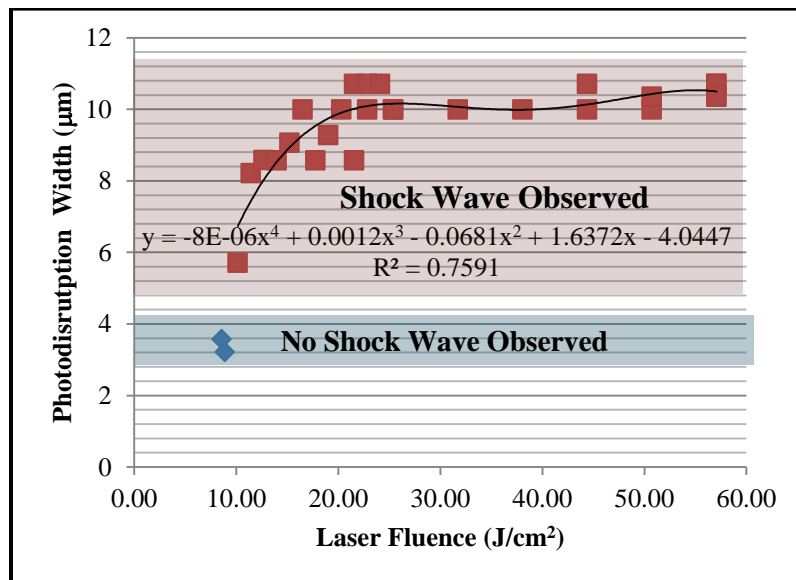
Figure 82 Photodisruption width in water vs. incident laser fluence, 9.7 ns after the photodisruptive laser pulse.

139
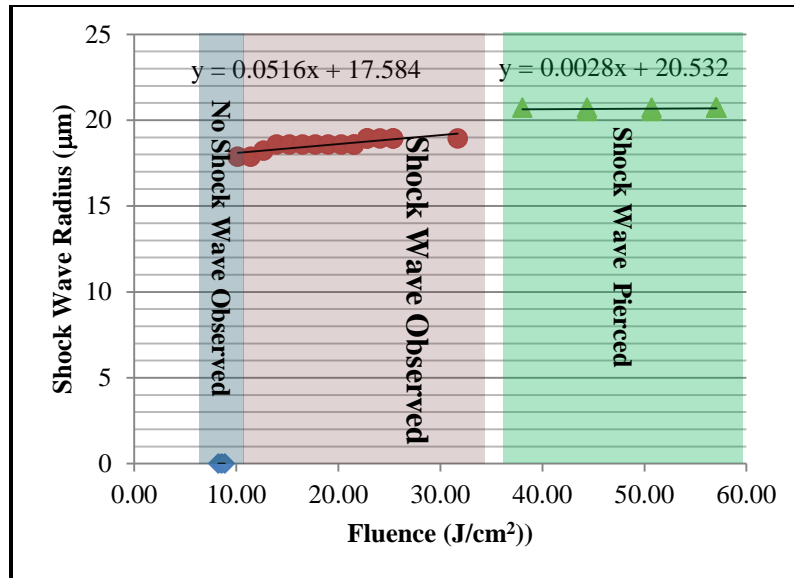
Figure 83 Shockwave radius in water vs. laser fluence at 9.7 ns after the laser pulse.

6.6   10ps Laser interaction in gelatin

In In this section, the 10ps laser interactions in gelatin are reported. This was representative of the laser being focused into the fibrous mass of the lens. In confined media, the impact of successive laser pulses do not dissipate and may possibly affect the successive laser pulses as the gasses from the photodisruption are confined to the region of the previous pulse. Depending on fluence and focal spot spacing these effects may adversely impact successive pulses to the same targeted area, reducing the effectiveness of the laser interaction. During the photodisruption process in water, a bubble of oxygen gas is generated. This bubble is free to move away from the focal volume. This is not true for structured media. In structured media, the gas generated by the photodisruption of the material does not move out of the interaction volume. In this study, structured media which allows for the time evolution of the laser interaction was investigated. Initially the interaction of the laser with gelatin for various fluence levels was studied.

140

The characteristics of the laser interaction were measured. This was followed by an

investigation of the evolution of the laser interaction over a 90 μs period.

6.6.1   Laser interaction for increasing fluence levels in gelatin

        In this experiment, the camera system was flashed the same as in Figure 76. The

only exception to this experimental set up was that the cuvette that was filled with water

was filled with gelatin with a thin layer of water on top. The laser was focused into the

gelatin and pulsed at a 10 kHz. The focal spot to focal spot separation of the pulses was

100 μm. Of interest in Figure 84 through Figure 86, is that the interaction does not show

some of the characteristics shown in the water study. There is no region that was

explored where a shock wave is not observed. Additionally, the bell that was seen that

grows over the photodisruption volume in water until approximately 38.01 J/cm^2 is not

present in the gelatin. Instead of the bell on top of the photodisruption column, the

volume seems to taper off for all fluence levels investigated. A plot of the length of the

interaction vs. the pulse fluence is presented in Figure 87. The data was fit using an

ablation model, but this did not model the knee of the interaction well. A three piecewise

linear model was utilized providing a better representative description of the data. A plot

of the FWHM value of the photodisruption column width with fluence is shown in Figure

88. The width measured is significantly different than the widths measured in water.

The shockwave radius is plotted in Figure 89 for various fluence levels. This shockwave

radius appears to be approximately 19 microns in diameter. This corresponds to a

velocity of 1966 m/s in gelatin.
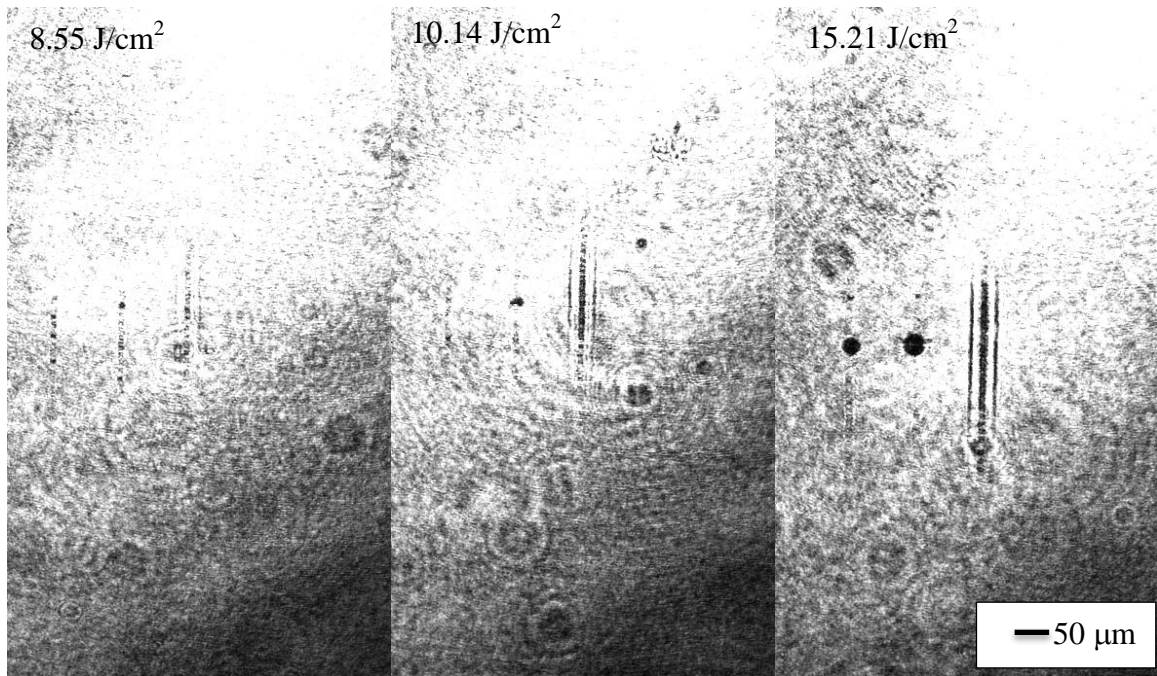
Figure 84 Photodisruption in Gelatin laser fluence levels from 8.55 J/cm^2 to 15.21
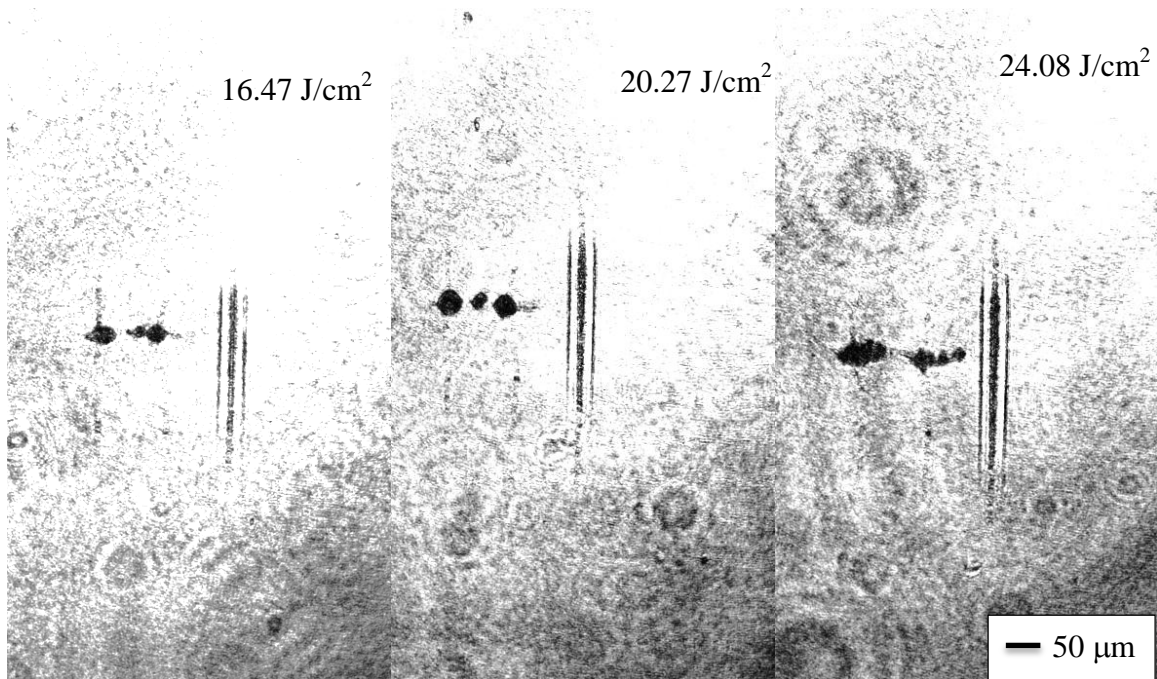
Figure 85 Photodisruption in gelatin for laser fluence levels from 16.47 J/cm^2 to 24.08 J/cm^2
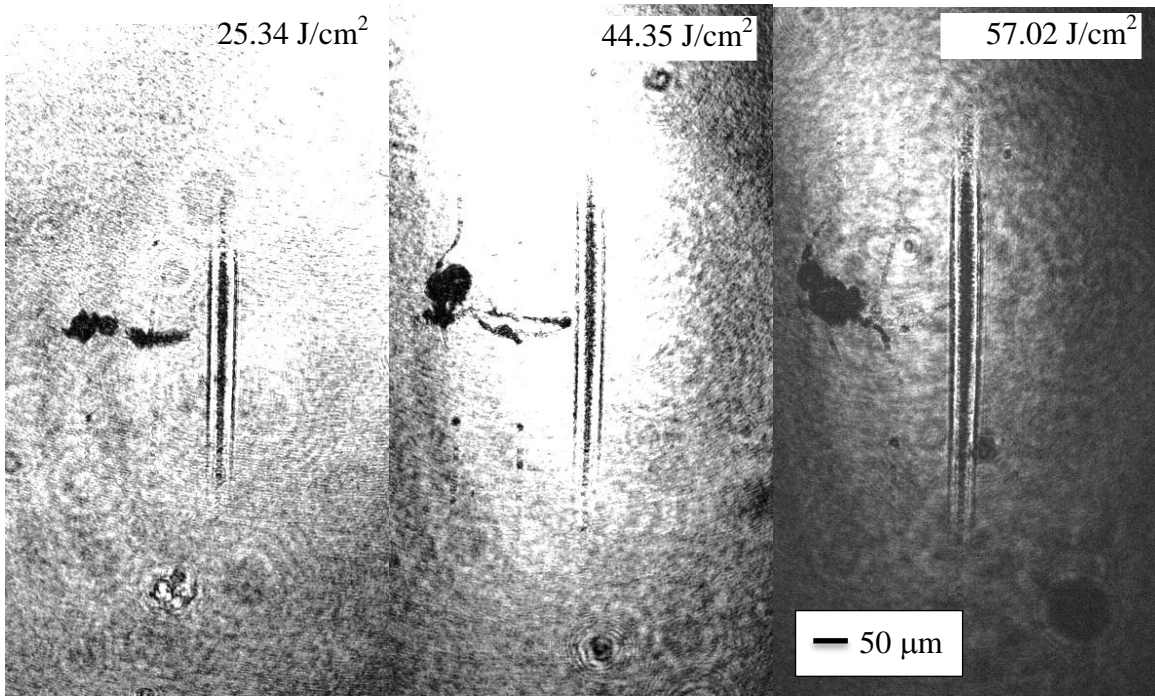
Figure 86 Photodisruption in gelatin for laser fluence levels from 25.34 J/cm^2 to 57.02 J/cm^2
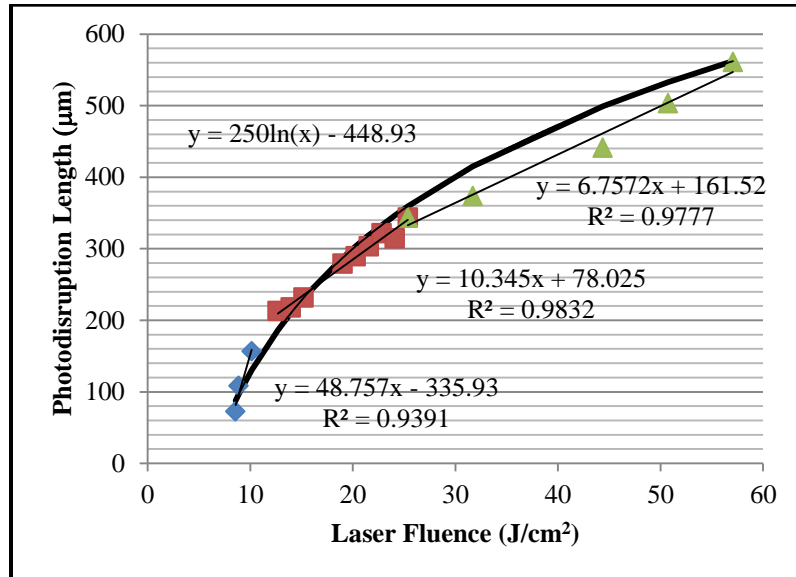
Figure 87 Photodisruption column length vs. laser fluence for gelatin measured 9.7ns after the laser pulse.
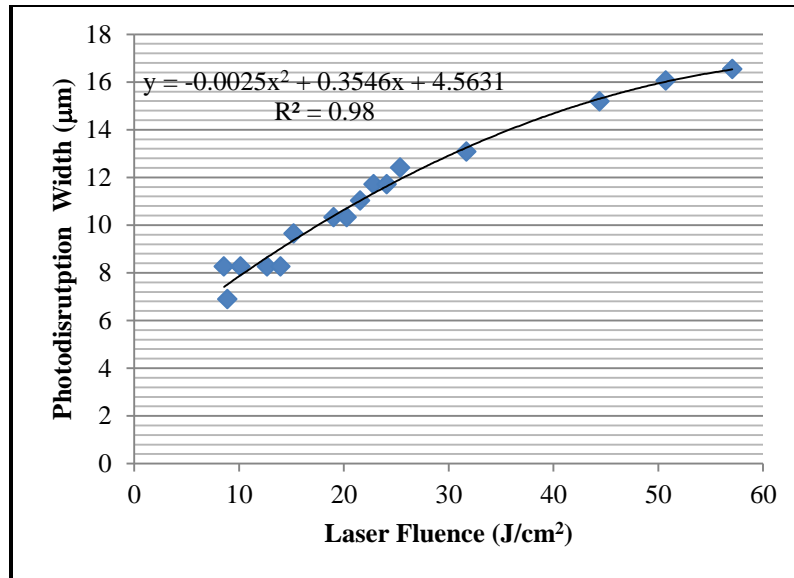
Figure 88 Width of photodisruption column for gelatin vs. laser fluence measured 9.7ns after laser pulse.

The plot is annotated with $y = -0.0025x^2 + 0.3546x + 4.5631$ and $R^2 = 0.98$.
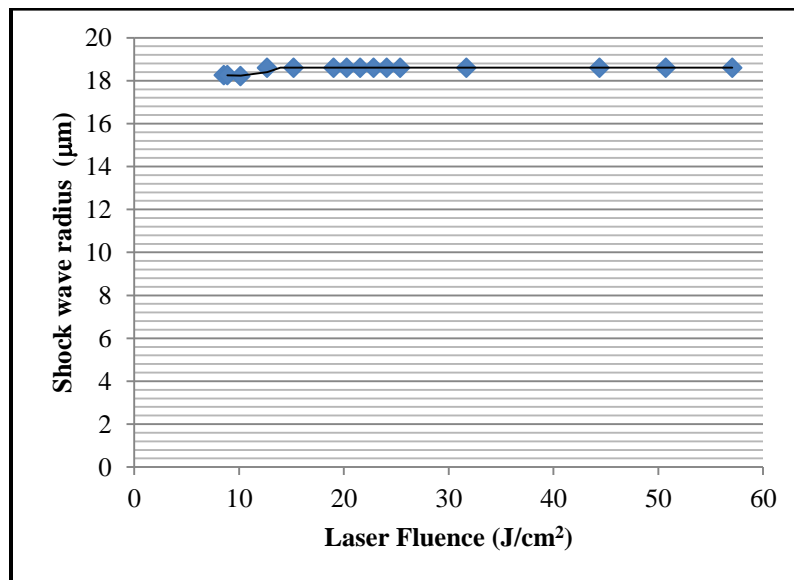
Figure 89 Shockwave radius in gelatin as a function of laser fluence measured 9.7ns after laser pulse.

6.7   Evolution of photodisruption

The time between pulses affects the spacing that can be achieved without interference from the previous photodisruptions. Successive laser pulses may experience different conditions depending upon the frequency of the laser. The evolution of the

144

photodisruption bubble will affect the successive pulses differently depending upon the time delay between pulses. In this section the evolution of 12.67 J/cm^2 10ps laser interaction with gelatin over a period 90 μs is reported. The goal of the experiment was to determine how long it would take for a 12.67 J/cm^2 photodisruption bubble to evolve to a semi steady state. By adjusting the electronic delay described in Section 6.4.4, the period of time that the camera is able visualize events can be controlled so that several pulses can be observed. The frequency of the laser determines the time between each pulse seen in the imagery. This allows for the evolution of the laser pulse in media to be studied. Figure 73 shows a schematic of this process. The distance between each pulse represents a time delay from the previous pulse that is dependent on the laser frequency. When the last laser pulse of the series of laser pulses is backlit with the SHG beam, a time stamp of the laser interaction can be collected for an extended period of time. Looking at the evolution of the photodisruption process defines the environmental effects of successive pulses have as they interact with the material. In particular, as the time delay between successive pulses is lengthened or shortened when making clinical applications of the laser to the eye, the laser pulse following a laser pulse will be affected to varying degrees by the impact of the previous laser pulse depending on the period of time from the previous pulse. In this case 10 pulses at a 100 kHz frequency represents the time between 2 pulses at 10 kHz. This is important for laser interactions with tissue, irregular effects can occur if consideration is not given to the timing since the preceding laser pulse and successive time lags. If the interaction desired is to dissect tissue, tags of untreated tissue may result from photodisruption not occurring in the eye as programmed. In Figure 86 the pulses that occur before the final pulse in the series had complex

interaction with earlier laser pulse interactions region in the gelatin of approximately 50 microns or more.

Figure 90 shows the evolution of a series of ten 12.67 J/cm^2 pulses. The last laser pulse was captured 9.7 ns after the laser pulse. Each successive pulse moving to the left in the image is 10 μs earlier in time. The total image represents 90 μs of laser interaction evolution. As soon as 20 μs after the laser pulse, a bubble of approximately 30 μm has formed that might affect laser shot spacing closer than 15 μm for a 50 kHz laser pulse rate. Depending on the pulse rate of the laser the effective interaction measured on that time scale should be considered when determining the parameters for the geometry and spacing of the laser pulses in the material of interest.
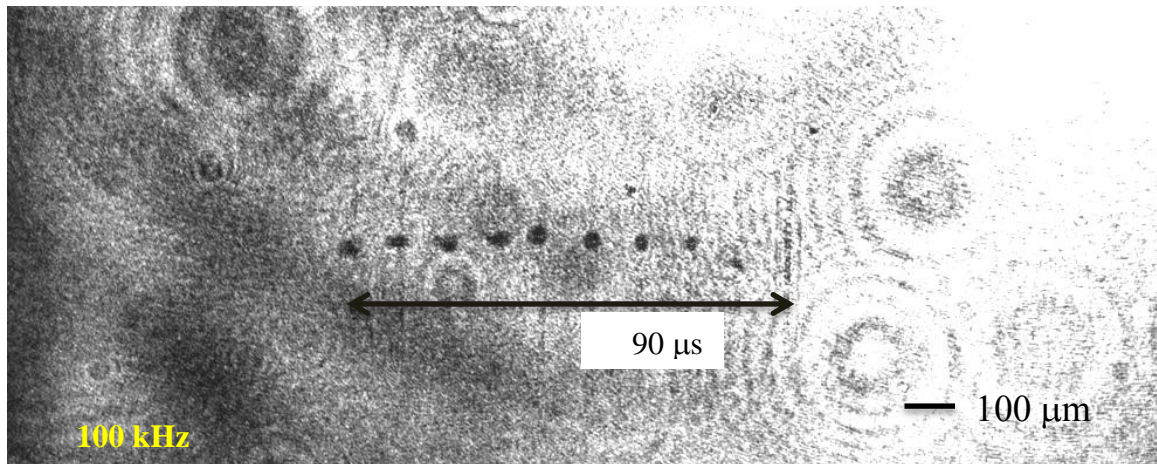
Figure 90 The evolution of the photodisruption bubble over 90 μs.
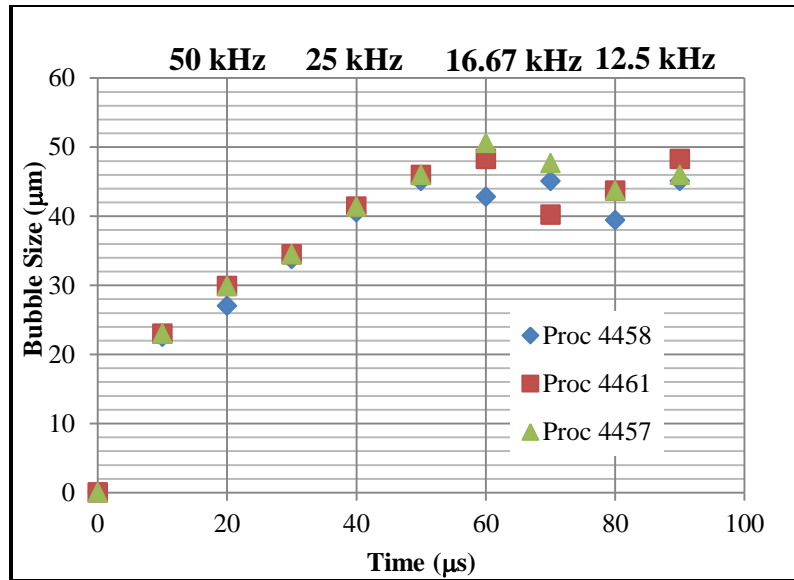
Figure 91 Photodisruption Bubble growth over time for a series of $12.67\ \text{J/cm}^2$ pulses 100 μm apart in gelatin.

6.8   Summary and Conclusions

The effects of laser interaction in water and gelatin have been examined. A comparison between the lengths of the laser interaction for gelatin and water are shown in Figure 93. The plot shows that the photodisruption lengths for each of the materials are comparable. The width of the interaction in water asymptotically approaches 11 microns whereas the width of photodisruption column in the gelatin continues to expand as the fluence increases. The cylindrically expanding shockwave radius measured for the two materials were within a micron of each other.
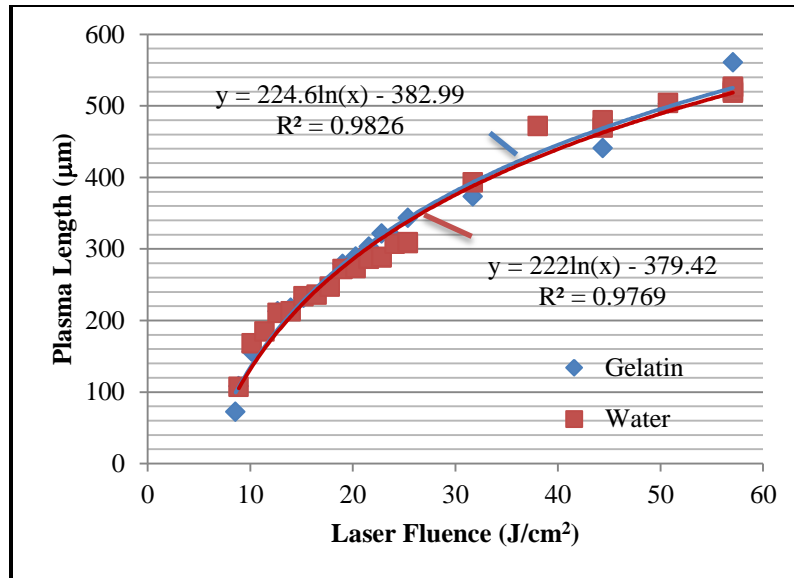
Figure 92 Comparison of photodisruption column widths between gelatin and water 9.7 ns after the laser pulse.

The evolution of a pulse plays an important role in determining shot spacing and the effectiveness of a disruption pattern in the eye. As the laser fluence goes up, local impact from a laser pulse increases. As seen in Figure 85 and Figure 86 higher fluence levels affect a larger region around the photodisruption. This is evident by the shape of the trapped gas around the pulse. Higher energies may be useful in the treatment of cataracts requiring fewer pulses to break apart the fibrous mass.   At low fluence levels as shown in water in Figure 78 the fluence levels where a plasma column is formed and no shock wave is present can be used to process materials. At these fluence levels, closer shot spacing is required if tissue dissection is desired.

In the case of the lens capsule, each of the elements explored plays a role in determining

how to treat the capsule effectively. The capsule sits on a boundary between the anterior
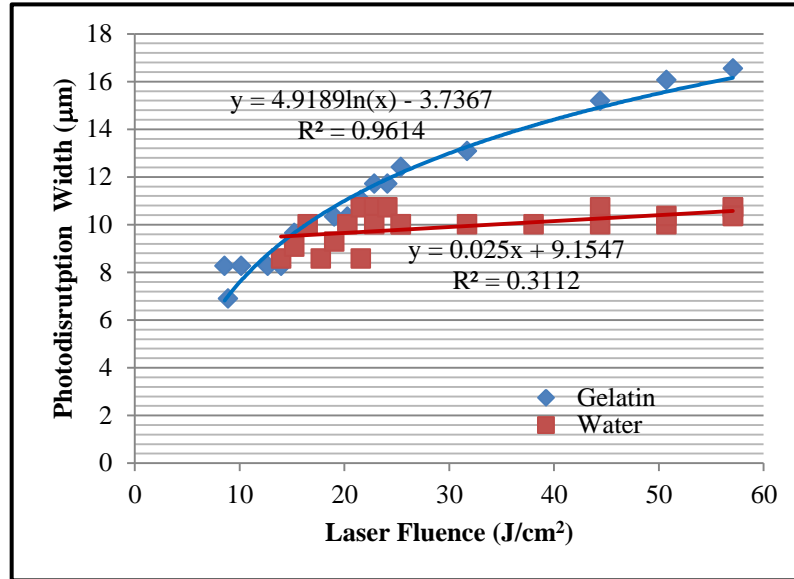
Figure 93 Comparison plot between photodisruption widths shot in gelatin and water measured 9.7 ns after laser pulse.

chamber and the fibrous mass of the lens. When the capsule is treated with the laser, the

photodisruption process starts in the fibrous mass and moves up across the capsule into

the anterior chamber. Photodisruptive pulses in the fibrous mass generate gas. This gas

may change the location of the capsule as it is being processed. This will result in the

need to treat a longer distance to ensure that the capsule is dissected. To reduce this

effect, lower laser fluence levels are desirable.

Bubble formation in the anterior chamber can also interfere with effectively

dissection of the capsule. The bubbles formed from earlier pulses could affect dissection

by interfering with a laser pulse causing it to not dissect the lens capsule. This issue also

points toward using less fluence and higher frequencies to dissect the capsule. For

frequencies in excess of 100 kHz, the effects appear to be minimized for fluence levels less than 12.67 J/cm^2. There is concern about damage to the retina at an average power of 1W. In future studies this should be examined more closely.

In conclusion, this study explains the behavior of laser induced photodisruption in surrogate materials for the anterior chamber and the fibrous mass. It defined expectations on the photodisruption dimensions and affects. These properties can be applied to the study laser interactions in the eye. The effect of the laser in water builds an understanding of the laser interaction in a biological environment. Photodisruption interaction effects such as interaction length, width, and shockwave radius were examined. The use of water as a model media for laser photodisruption does not apply to the study of photodisruption in structured media such as gelatin. The evolution of photodisruption in stratified media can affect the processing of material resulting in undesired effects as seen by examining photodisruption in gelatin. Photodisruption lengths generated in water and gelatin are similar but the accumulation of trapped bubbles in gelatin or other structured media can affect laser photodisruption at a defined location.

CHAPTER 7 STUDY OF PHOTODISRUPTION IN A PORCINE EYE

This chapter reports the results of the experimental investigation conducted using *ex vivo* porcine eyes as a model for human eyes. The purpose was to evaluate photodisruption near and at the boundary between the anterior chamber and the crystalline lens. One goal of these experiments was to determine the photodisruption threshold of the capsule and the fibrous mass of the lens, as described in Chapter 2. This was accomplished by studying the effects of increasing laser fluence level on the capsule for different axial focus spot separations. In the fibrous mass it was not possible to examine the photodisruption event to the same fidelity as was done in gelatin in Chapter 6. Instead the event was observed within the means of the experimental apparatus, which included examining the formation of gas bubbles in the lens when a photodisruption event occurred. Thus when threshold in the fibrous mass was studied, two criteria were used when determining when a successful photodisruption had occurred: 1) gas bubbles were observed in the lens following a laser pulse; and 2) the axial focus spot spacing between laser pulses is greater or equal to the photodisruption length for the fluence found in water.   The threshold of the capsule was defined as the fluence level required to pierce the capsule using photodisruption from one pulse. The other objective of this study was to examine the laser interaction characteristics across the capsule as laser fluence levels were increased. By examining the effects of axial focal spot spacing, laser interaction accumulation can be studied. This information will help guide the selection of axial focus spot spacing for clinical applications. Damage to surrounding tissue due to

heat production or strong shockwaves caused by excessive laser fluence may weaken the capsule, which may lead to surgical complications such as tearing of the capsule. After laser capsulotomy surgery, the excised capsule was inspected using microscopy to visualize the laser interaction area. The porcine eyes available for use in these studies were a poor model for an aged, cataractous eye because of the soft lens. To be able to compare the effects of laser interaction in the lens with the current standard of care for cataract treatment, a phacoemulsification device would have been needed. This would have allowed the accumulated energy necessary to remove the fibrous mass from the capsule to be measured for both the laser and phacoemulsification device. Young porcine eyes do not require any phaco energy to remove the fibrous mass, thus these experiments were not performed.

7.1 Experimental Process

Fresh porcine eyes were secured to the laser system, as described in Chapter 5, and capsulotomy patterns with a focus spot spacing of 25 microns and variable axial, z, spacing were incised. A sketch of a capsulotomy pattern process is shown in Figure 94.
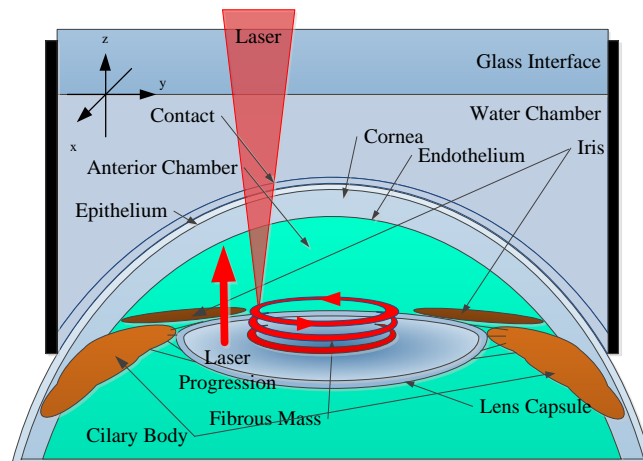
Figure 94 Schematic of the test pattern cut on pig lenses. Successive capsulotomy diameters change the axial distance between the

The capsulotomy pattern was created using a ring pattern that is repeated at the same diameter multiple times at different axial depths. The capsulotomy pattern was used because it compensates for the sag of the lens. This puts the laser focus at the same relative position to the capsule for each experiment. On each porcine eye, several capsulotomies with varying diameters were created using different axial spacing for each varied diameter. The smallest diameter ring was generated at an axial spacing that is 10% of the photodisruption length measured in water. For successively increasing capsulotomy diameters, the axial distance between pulses was varied as listed in Table 11. Figure 95 shows a schematic illustrating the differences between successive rings, with the percentages corresponding to the percent of the photodisruption length for a given fluence measured in water in Chapter 6. The diameter of each successive ring was set to 0.35mm larger than the previous ring with a minimum diameter of 1.0mm. The frequency of the laser was set at 20 kHz, which is near the limit of eye safe operation for the laser system described in Chapter 5 at the highest fluence level tested. The lateral focus spot separation was 25 μm. The laser fluence levels tested are also outlined in Table 11. The laser fluence levels investigated went from 6.34 J/cm^2 to 25.34 J/cm^2 and were chosen such that the relative peak power at each fluence level was less than the self-focusing threshold. The axial, z, spacing went from 7 microns to 515 microns depending on the fluence level. When the axial spacing was less than the photodisruption length the accumulation of laser interaction area on the capsule was examined, while axial spacing that was greater than the photodisruption length was used to determine threshold in the fibrous mass. Axial spacing greater than the photodisruption length was also used to determine the photodisruption puncture size in the capsule. After lasing each eye, the

anterior portion of the capsule was removed and examined for evidence of laser

interaction using a microscope. Images were collected for each eye then analyzed to

determine laser interaction area and/or puncture size for a single pulse going through the
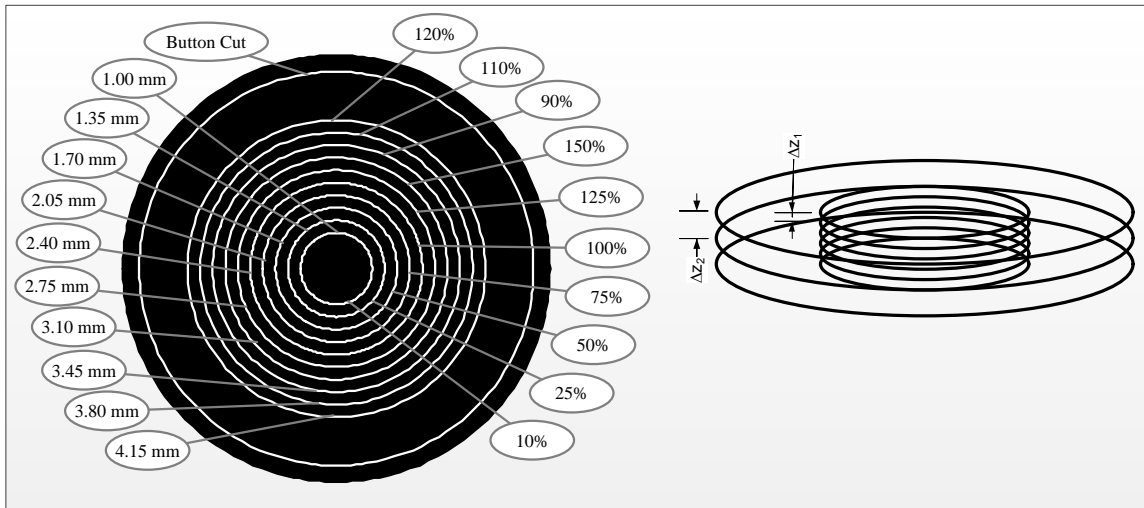
capsule.

Figure 95 Schematic of the test pattern generated on pig lenses. Successive capsulotomy
diameters change the axial distance between the laser focus positions

Table 11 Table of laser parameters used to determine whether the photodisruption column causes photodisruption in the pig capsule and fibrous mass.

Test Matrix											
	Eye	1	2	3	4	5	6	8	9	10	11
	Fluence (J/cm^2)	8.55	6.34	7.60	8.87	10.14	12.67	15.21	20.27	22.81	25.34
	Energy (µJ)	6.75	5	6	7	8	10	12	16	18	20
Diam. (mm)	Relative Photodisruption Length (%)					Δz (µm)					
1	10%	7	7	7	11	16	21	23	29	32	34
1.35	25%	18	18	18	27	39	53	58	72	80	86
1.7	50%	36	36	36	54	78	106	116	145	161	172
2.05	75%	54	54	54	81	117	160	174	217	241	257
2.4	100%	72	72	72	108	156	213	231	289	321	343
2.75	125%	90	90	90	135	196	266	289	362	402	429
3.1	150%	109	109	109	162	235	319	347	434	482	515
3.45	90%	65	65	65	97	141	*15*	208	260	289	309
3.8	110%	80	80	80	119	172	*30*	255	318	354	377
4.15	120%	87	87	87	130	188	*5*	278	347	386	412

7.2 Experiment

Fresh porcine eyes were obtained from a local abattoir within 12 hours of death. These eyes were transported to the laboratory in a dilute blood solution and were screened for damage such as cuts or edema in the cornea upon arrival. The eyes with brown iridial pigmentation were used, rejecting those with other pigmentation, to ensure that the eyes were as similar as possible. Slit laser scanning was performed and three images were then manually processed placing markers on the reference glass and lens surface. An image of this technique is shown in Chapter 5 Section 5.3 Figure 61(a). The beam directing system then processed the information to determine the positioning and radius of curvature of the lens. Successive capsulotomies were then generated in the sample as outlined in 7.1 Experimental Process. Each of the capsulotomies was designed to start approximately 0.5mm below the capsule, in fibrous mass of the lens, and progress 1.5 mm anteriorly in the axial direction. This process was repeated for several fluence levels up to 25.34 J/cm^2 on a total of 10 eyes. Figure 96 shows the images collected at the end of surgery on a porcine eye at a laser fluence of 25.34 J/cm^2. As seen in the first two images, (a) and (b), coalescence of gas in the fibrous mass may occur. The amount of coalescence depends on the laser fluence level. Each image shown in Figure 96 corresponds to the laser having reached the most anterior axial location of laser interaction placement.

Once the lasing was complete for laser interaction experiment, the cornea of each porcine eye was removed and the anterior capsule separated from the lens using utrata forceps. These forceps were expressly designed for surgical capsule manipulation. The capsule button was then fixed using a 2.5% glutaraldehyde, 0.1 Molar Cacodylic fixative to preserve the button. This fixative was designed to minimize changes in the lens (123). The sample preparation process

was repeated for all laser treated eyes prior to microscopic inspection. Once the capsule samples were preserved, they were examined under a Nikon BH-2 microscope system using a high-resolution camera. For each laser fluence level, several optical microscopy images were taken.

The capsule samples were analyzed to determine both the size of the puncture size and the total interaction area in the capsule that resulted from photodisruption. Figure 97 shows example measurements made on a capsule sample. To determine the average photodisruption puncture size, 10 photodisruption punctures on each ring that was produced using an axial focus spot spacing greater than the photodisruption length measured in water for that fluence measured in water was measured and averaged. Using rings with these parameters ensured that only one photodisruption event caused each individual effect in the capsule. Measurements were made using micrographs of the capsule samples and sizing software reticles to match the size of each of a series of ten photodisruption punctures. This is shown in Figure 97(a). Rings that had axial spacing less than the photodisruption length measured in water for the specific fluence used were measured to determine the total interaction area. A software reticle equal to the diameter of the interaction area was used to measure collateral tissue involvement by averaging the area within the reticles for 10 consecutive capsule defects, as shown in Figure 97(b). These measurements were used to examine the individual and accumulated pulse interaction effects of the capsule and laser.
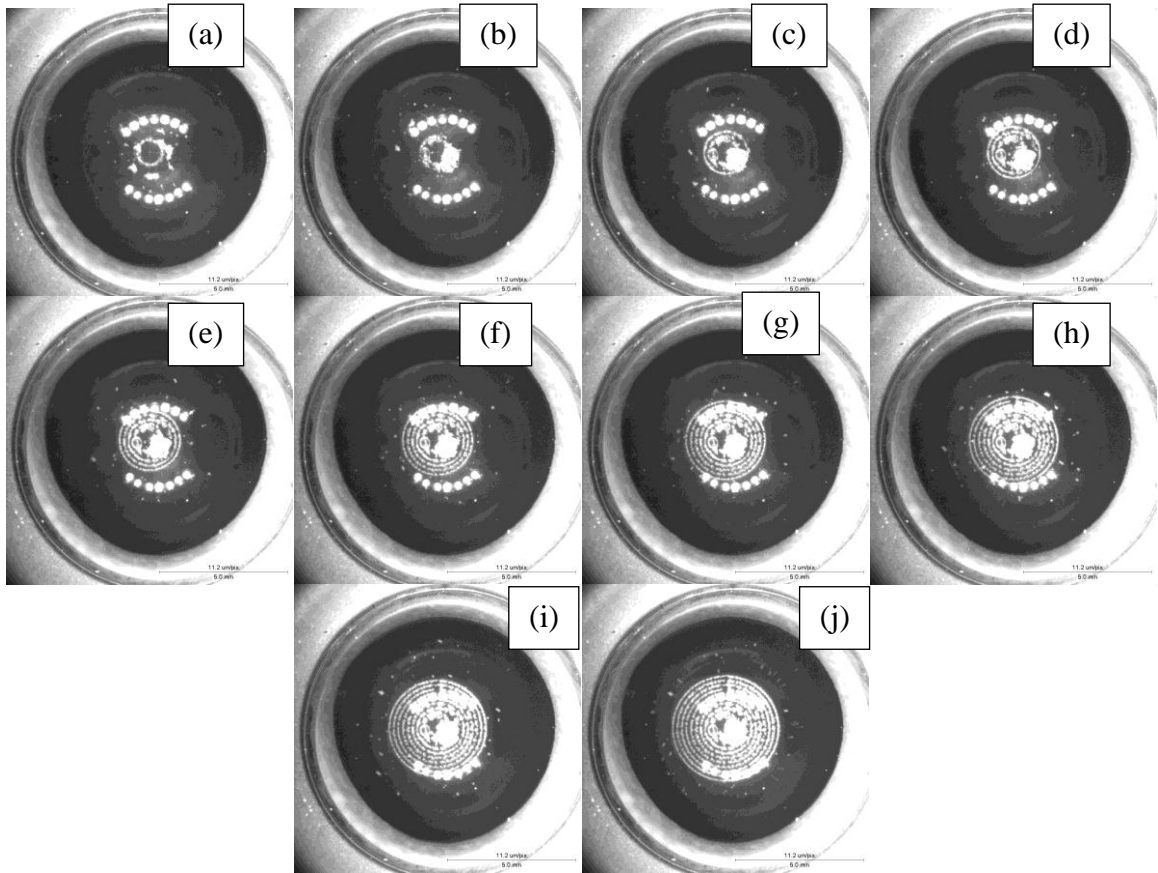
Figure 96 Successive Capsulotomy rings in a porcine eye (a) Δz = 10% photodisruption length (PL), (b) Δz = 25% PL, (c) Δz = 50% PL, (d) Δz = 75% PL, (e) Δz = 100% PL, (f) Δz = 125% PL, (g) Δz = 150% PL, (h) Δz = 90% PL, (i) Δz =110% PL, (j) Δz = 120% PL
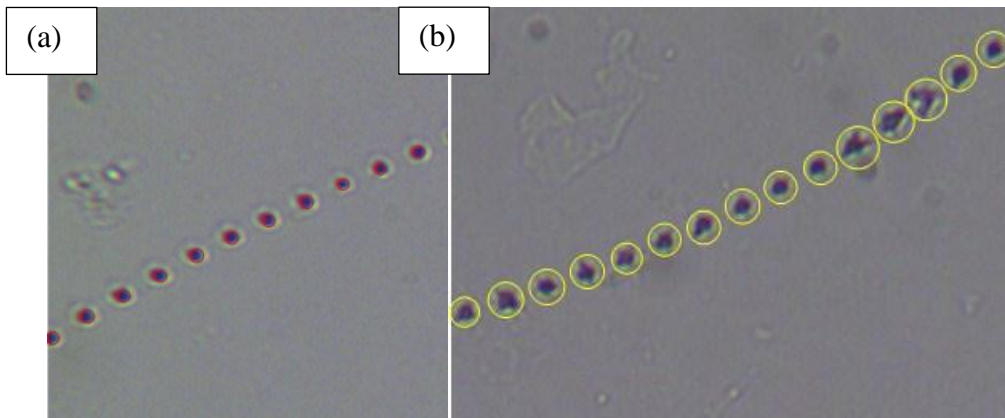
Figure 97 (a) Measurements of pulse interaction size (b) Measurement of laser interaction zone.

7.2.1 Analysis of 7.60 J/cm² interaction with a porcine eye
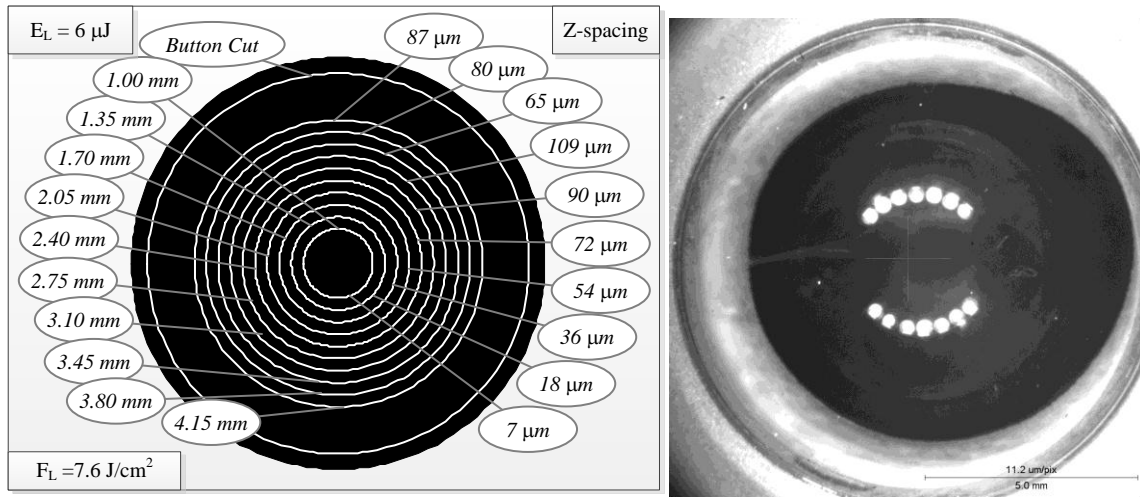
Figure 98 (a) Laser Pattern generated in the eye. (b) Surgery Image after last pattern was made for F_L = 7.60 J/cm².

Laser surgical patterns were performed at a fluence of 7.60 J/cm² at focus in the eye. The axial, z, spacings used for this surgery are shown in Figure 99 (b) is an image of the porcine eye after the test laser surgeries were completed. Figure 99 shows a composite micrograph of the capsule sample after preservation with fixative occurred. There were no defects observed in the capsule that would be indicative of laser photodisruption.
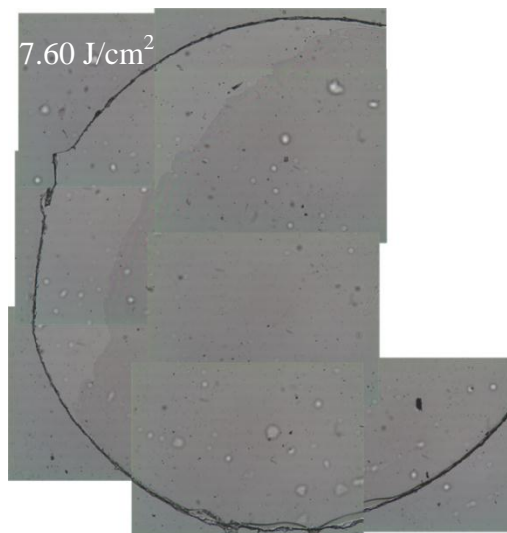
Figure 99 Composite porcine capsular microscopy for 7.60 J/cm² capsulotomies generated at different axial focus spot separation.

7.2.2 Analysis of 8.55 J/cm^2 capsular analysis

Figure 100 (a) Laser Pattern generated in the eye. (b) Surgery Image after last pattern was made for $F_L = 8.55$ J/cm^2.

Figure 100(a) illustrates axial, z, spacing for the capsulotomies performed at a fluence of 8.55 J/cm^2 at focus in the eye. The photodisruption length for the laser was expected to be 72 μm based on the photodisruption lengths measurement made in water for this fluence. Evidence of photodisruption within the lens was visible in the porcine eye after the last pattern was generated, as shown in Figure 100 (b). The only rings that were visible in the anterior capsule sample under microscopy, indicating laser interaction with the capsule, were at axial focal spot spacing of 7 μm and 27 μm, see Figure 101. The laser interaction for the ring with an axial spacing of 7 μm was only partial, much of the pattern was not apparent in the capsule. The average laser interaction area for individual puncture defects in the capsule for this spacing was 34 μm in diameter. For the 27 μm axial spacing surgical treatment ring, the average laser interaction diameter for individual capsular defects is 24 μm with a standard deviation of 6.1 μm, for areas where the capsule was punctured. Capsular defects were not observed in laser

160

treatment areas with axial focal spot spacing equal to or greater than the photodisruption length

of 72 microns, indicating the fluence level was below the threshold of the capsule.

Figure 101 Porcine Capsular microscopy for 8.55 J/cm^2 capsulotomies generated at different axial focal spot separation.

7.2.3   Analysis of 10.14 J/cm^2 laser interaction
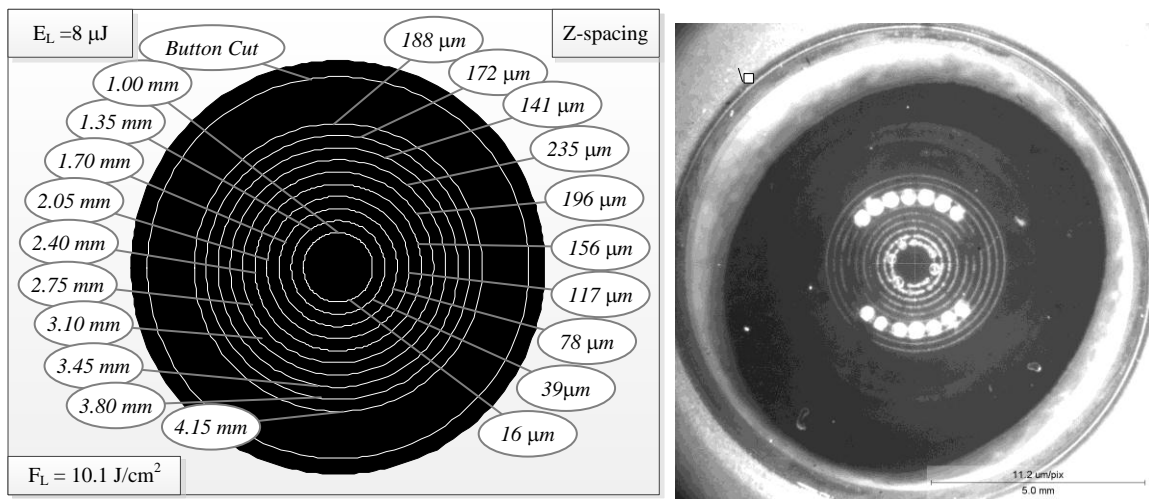
Figure 102 (a) Laser Pattern generated in the eye. (b) Surgery Image after last pattern was made for F_L = 10.14 J/cm^2.

The axial, z, spacing diagram is shown in Figure 102(a). The surgical patterns were performed at a laser fluence of 10.14 J/cm^2 at focus in the eye. The photodisruption length for the laser was expected to be 156 μm for this fluence, based on photodisruption length measurements made in water for this fluence. Figure 102(b) shows the porcine eye after the last pattern was generated. The rings that were visible in the capsule (Figure 103), indicating that laser interaction occurred with the capsule during the laser surgery process, were at axial focal spot spacings of 16 μm through 188 μm. None of the rings generated in the capsule showed evidence of photodisruption at every intended sight. The maximum laser interaction area observed was 25 μm in diameter for capsular puncture defects and occurred when a z spacing of 16 μm was used. The minimum laser interaction area was measured to be 8.6 μm in diameter when an axial spacing of 117 μm was used. A plot of laser interaction area versus z spacing is shown in Figure 104. . Based on the observation that a single pulse going through the capsule resulted in a 3.90 μm puncture defect in the capsule for axial focal spot spacing greater than the photodisruption length measured in water, $F_L = 10.14$ J/cm^2 appears to be threshold for the capsule.

Figure 103 Porcine capsular microscopy for 10.14 J/cm^2 capsulotomies generated at different axial focal spot separation.

Figure 104 Laser interaction size versus axial focal spot spacing for 10.14 J/cm^2 for photodisruption sites that punctured the capsule.

7.2.4 Analysis of 15.21J/cm^2 laser interaction
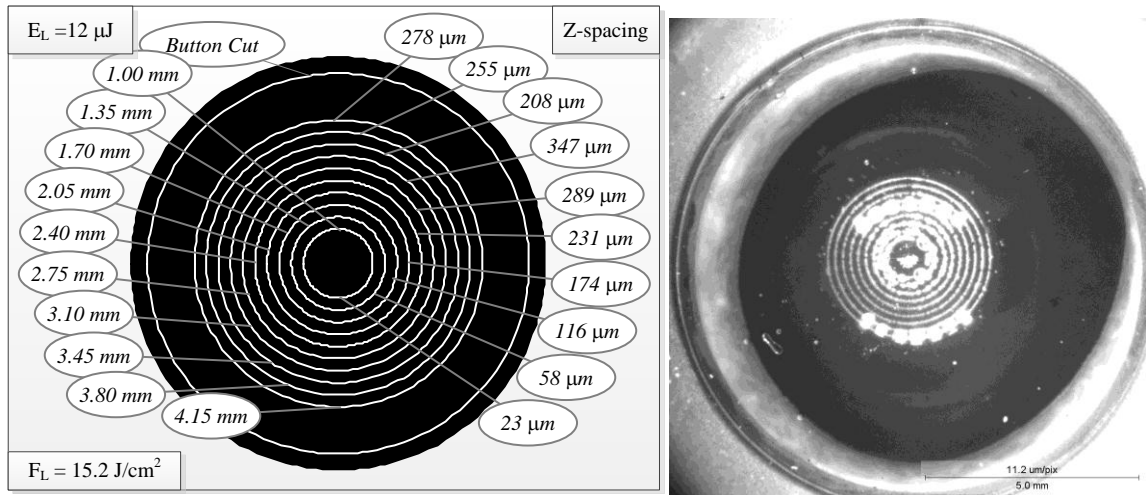
Figure 105   (a) Laser Pattern generated in the eye. (b) Surgery Image after last pattern was made for $E_L = 15.21$ J/cm^2.

     The axial, z, spacing diagram is shown in Figure 105(a). Surgical patterns were performed at a fluence of 15.21 J/cm^2 at focus in the eye. The photodisruption length for the laser was expected to be 231 μm for this fluence level, based on measurement of photodisruption length made in water for this fluence. Figure 105(b) shows the porcine eye as the last pattern was. The rings that were visible in the capsule, (Figure 106), indicating laser interaction occurred with the capsule during the laser surgery process, were at axial focal spot spacing of the 23 μm through 278 μm. None of the rings generated photodisruption punctures at every intended sight except for the inner ring. The maximum laser interaction area from the laser pulses came for a z spacing of 23 μm. The average laser interaction area for this spacing was diameter was 42.2 μm. The minimum laser interaction was measured at an axial spacing of 208 μm with laser interaction area of 14.9 μm. A plot of laser interaction versus z spacing is given in Figure 107. Based on observations , a single pulse going through the capsule resulted in a 4.3 μm puncture defect in the capsule.
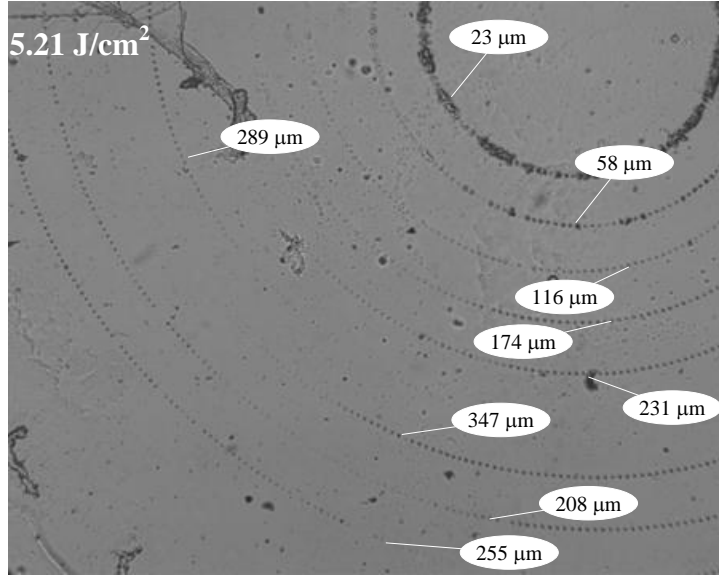
Figure 106 Porcine capsular microscopy for 15.21 J/cm^2 capsulotomies generated at different axial focal spot separation.
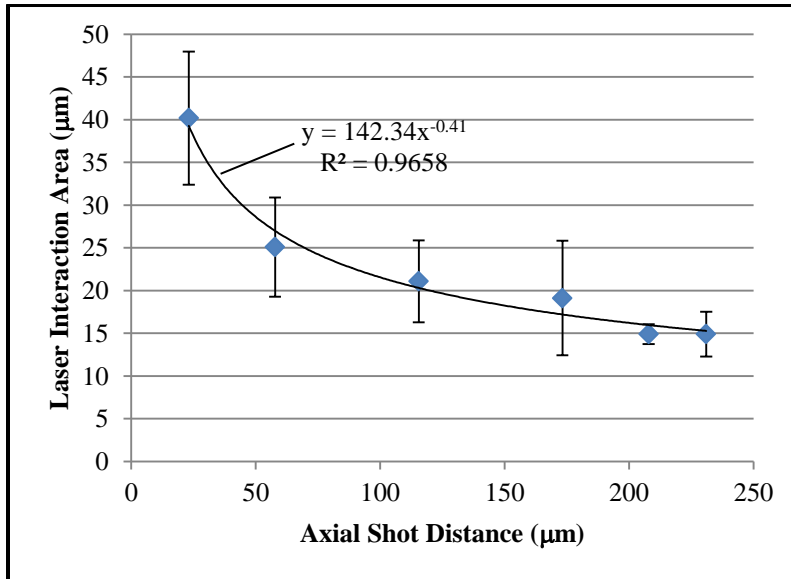
Figure 107 Laser interaction region size versus axial focal spot spacing for 15.21 J/cm^2 for photodisruptions that punctured the capsule.
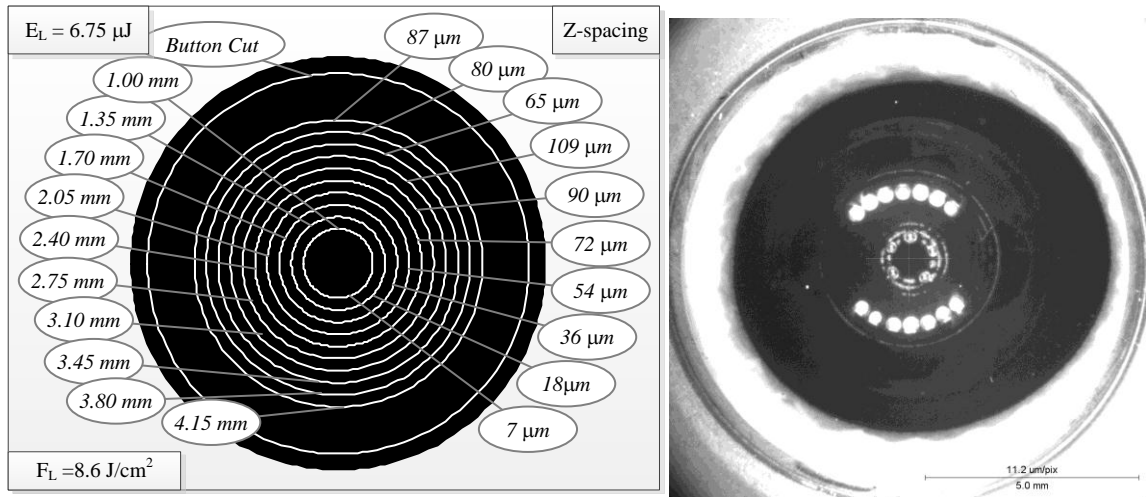
7.2.5 Analysis of 20.27 J/cm^2 laser interaction
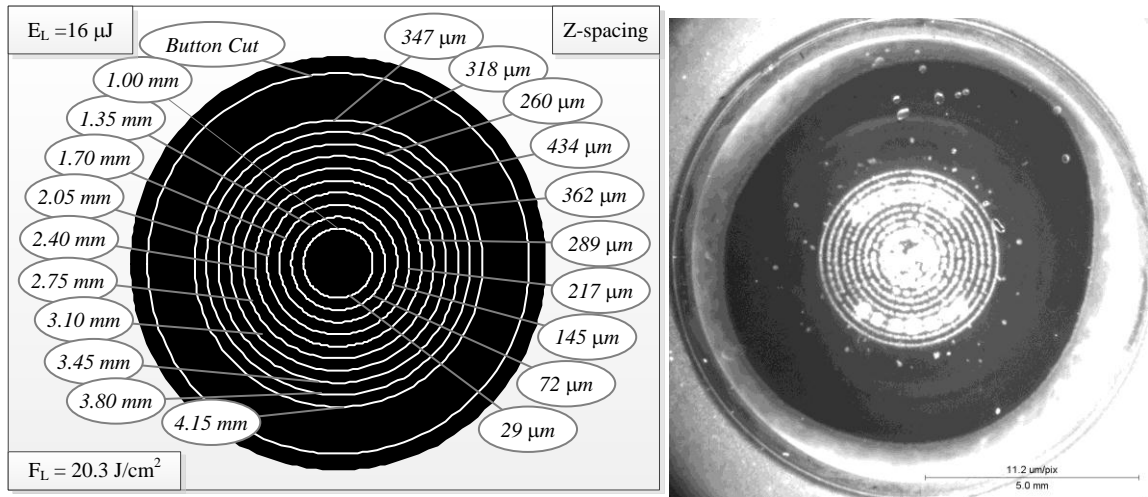
Figure 108   (a) Laser Pattern generated in the eye. (b) Surgery Image after last pattern was made for $F_L = 20.27$ J/cm^2.

The axial, z, spacing diagram for this surgery is shown in Figure 108(a). The surgical patterns were performed at a fluence of 20.27 J/cm^2 at focus in the eye. The photodisruption length for the laser was expected to be 289 µm for this fluence level, based on the photodisruption length measurement made in water. Figure 108(b) shows the porcine eye after the pattern was generated. The rings that were visible, indicating laser interaction in the capsule, (Figure 109), were at axial focal spot spacing of the 16 µm through 289 µm. Except for the central rings, none of the other rings generated showed evidence of photodisruption at every intended sight. The maximum laser interaction area was observed for an axial spacing of 29 µm. The average laser interaction area for this spacing was diameter was 46 µm.   The minimum laser interaction area measured was 14.2 µm at an axial spacing of 289 µm. A plot of laser interaction versus z spacing is given in Figure 110. A single pulse going through the capsule resulted in an average 4.6 µm puncture defect in the capsule.
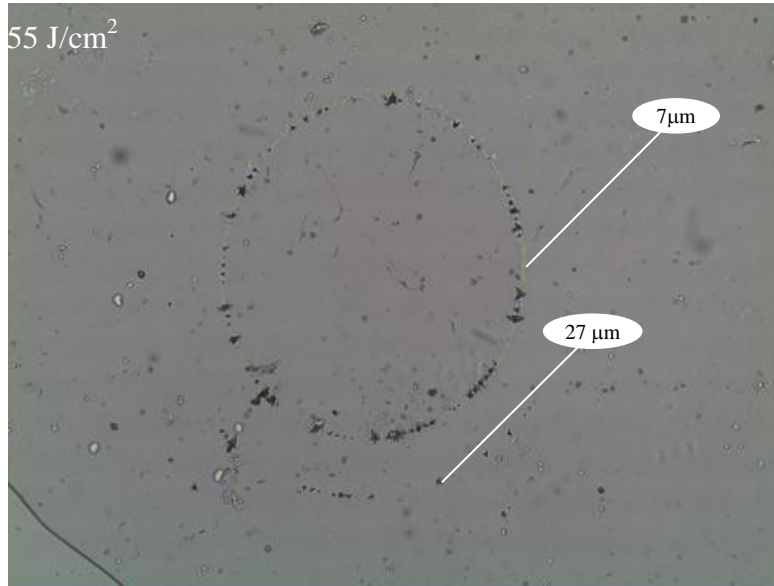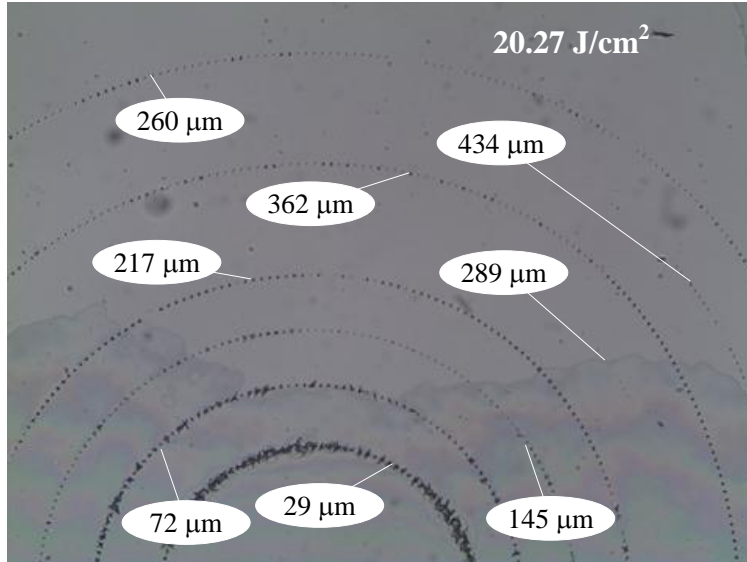
Figure 109 Porcine capsular microscopy for 20.27 J/cm^2 capsulotomies generated at different axial focal spot separation.

$$y = 228.69x^{-0.496}$$
$$R^2 = 0.925$$
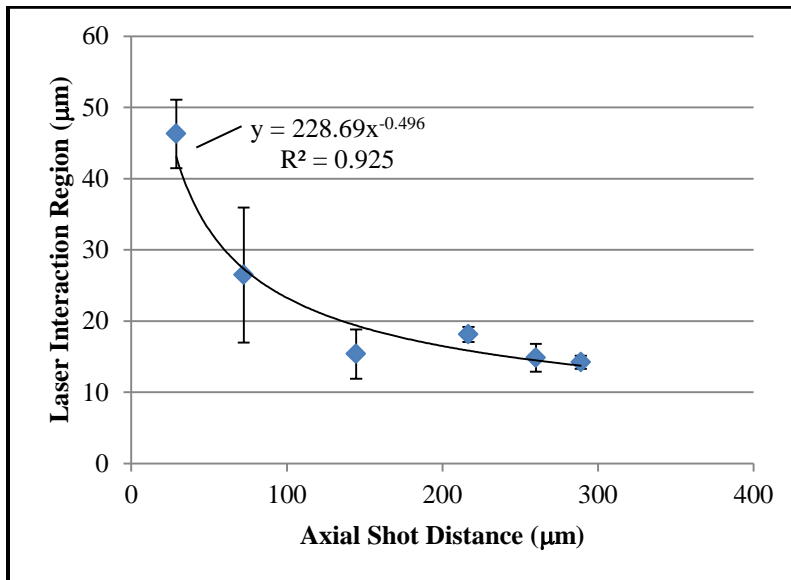
Figure 110 Laser Interaction Region versus axial focal spot spacing for 20.27 J/ cm^2 for photodisruptions that punctured the capsule.

7.2.6   Analysis of 25.34 J/cm^2 laser interaction
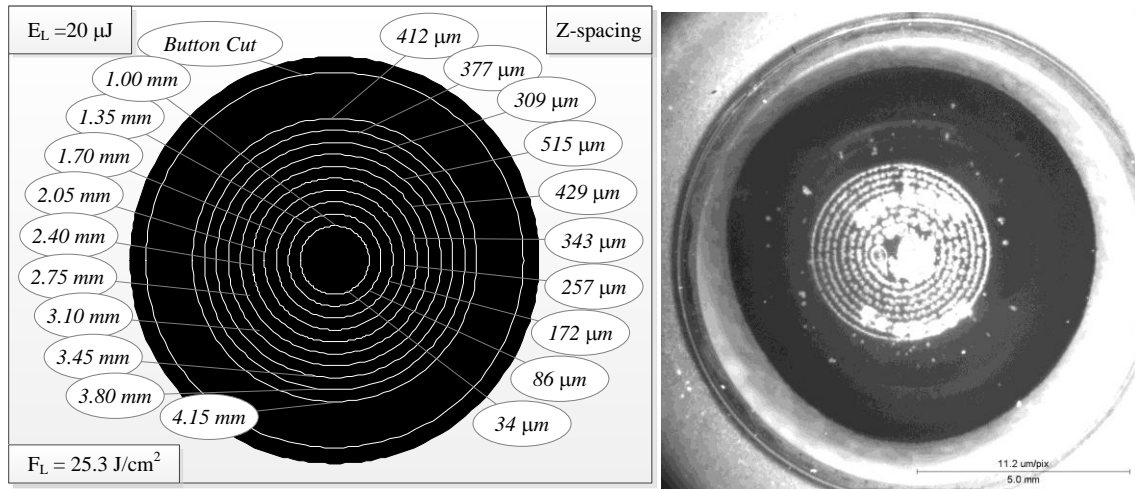
Figure 111 (a) Laser Pattern generated in the eye. (b) Surgery Image after last pattern was made for F_L = 25.34 J/cm^2

The axial, z, spacing diagram for this surgery is shown in Figure 111(a). The surgical patterns were at a fluence of 25.34 J/cm^2 at focus in the eye. The photodisruption length for the laser was expected to be 343 µm for this fluence level, based on measurements made in water. Figure 111(b) shows the porcine eye after the last pattern was generated.   The rings that were visible in the capsule, (Figure 112), indicating laser interaction occurred with the capsule, were at axial focus spot spacing from 34µm to 525µm. Only the axial spacing of 34 µm is complete having photodisruption sites that punctured the capsule at every intended site. None of other ring patterns observed were complete. The maximum laser interaction area from the laser pulses came for a z spacing of 34 µm, with an average diameter of 42 µm. The minimum laser interaction was measured at an axial spacing of 343 µm with an average diameter of 18.7 µm. A plot of laser interaction versus z spacing is shown in Figure 104. The single pulse effective diameter in the capsule was 7.3 µm.
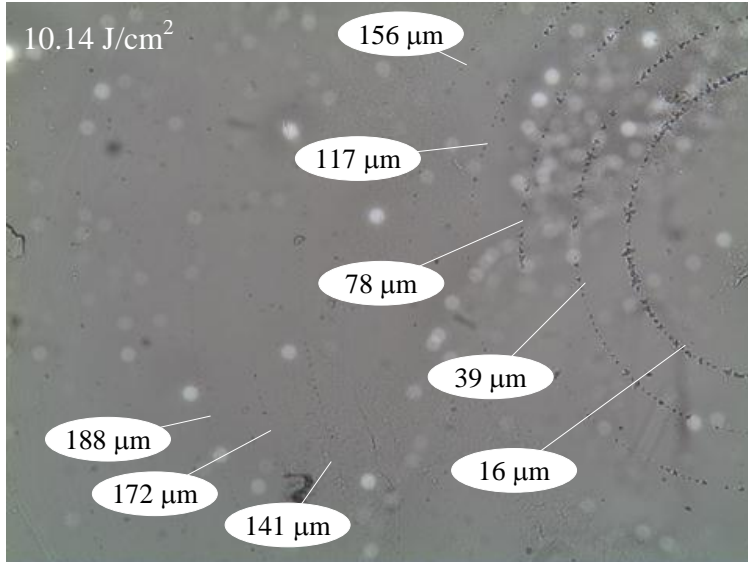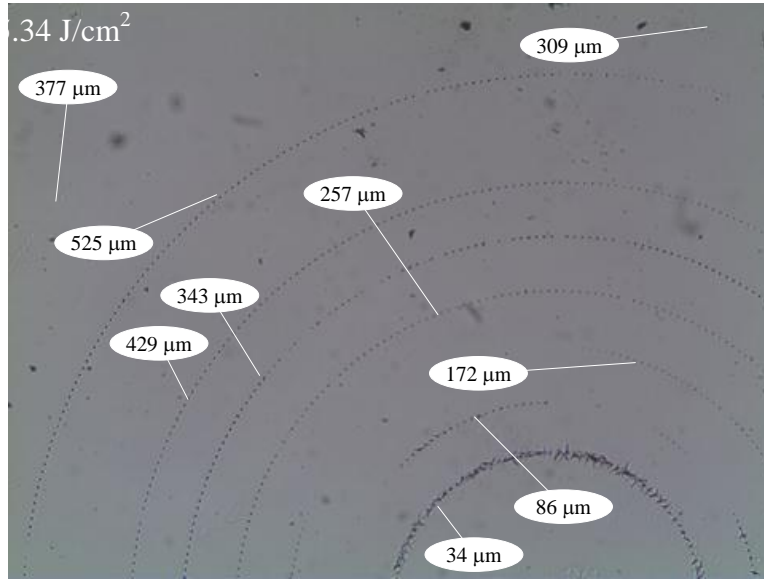
Figure 112 Porcine capsular microscopy for 25.34 J/cm^2 capsulotomies generated at different axial focal spot separation.
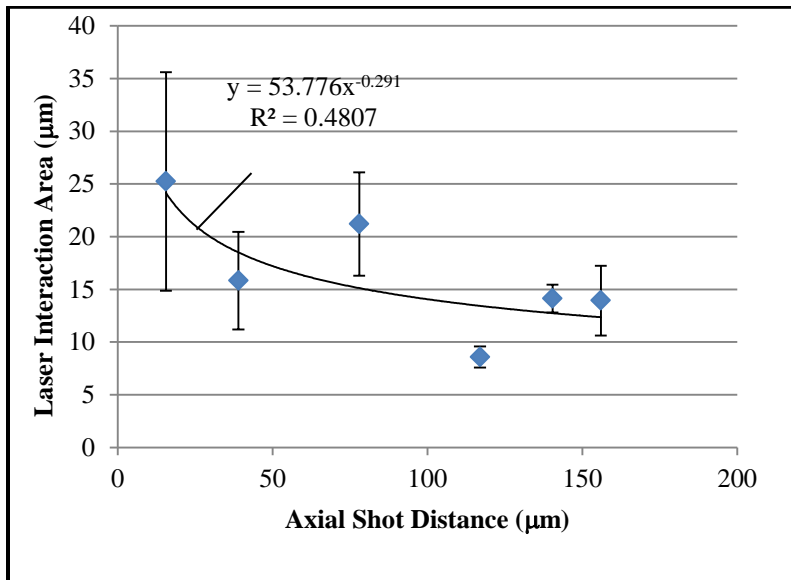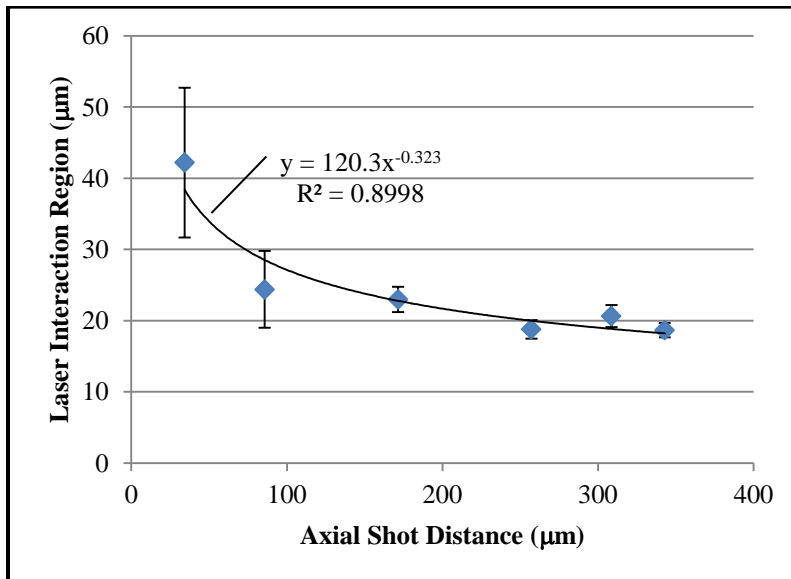

Figure 113 Laser Interaction Region versus axial focal spot spacing for 25.34 J/ cm^2 for photodisruptions that punctured the capsule.

7.3   Summary and Conclusions

In studying photodisruption at or near the boundary between the anterior chamber and

lens, the mechanics of the lens had to be studied. This led to an understanding of the mechanics

and the properties of the eye, which allowed a new model to be developed that was used to look at the behavior of the laser moving across the capsule. The model predicted conditions where the laser would not dissect the capsule due to the placement of the laser focus relative to the capsule. To test the model and further study the interaction of a 10 ps laser in the eye, a state of the art, first of its kind, laser system was utilized. The mechanics of the eye dictated the manner in which laser pulses were applied. A beam directing system determines the location of the lens and guides the main laser system focus to the desired location in the eye. This required that the focal spot be able to be scanned in 3-dimensions. After the laser system was built, a physical model was needed to study the interaction of the laser system with biological materials that were similar to the lens and anterior chamber. This allowed the effects of photodisruption to be studied in the lab prior to performing tests on animal models. From the study of gelatin and water, the length of the photodisruption in water and gelatin as a function of laser fluence was determined, defining the axial distance between successive rings of the capsulotomy pattern. This guided the experiments that were done in the porcine eye model. These pulses started posterior to the capsule and moved anteriorly into the anterior chamber.

The experiments conducted determined that the threshold fluence that caused photodisruption in the fibrous mass was 8.55 J/cm^2. The single pulse photodisruption threshold for the capsule was found to be 10.14 J/cm^2. This was the first time that laser photodisruption evidence was seen for focal spot spacing equal to 100% of the photodisruption length for this fluence level. During the experiments it was found that photodisruptions in the anterior chamber result in bubbles of mostly oxygen that can shield the laser beam from photodisrupting in the capsule. Surgical patterns must therefore start from within the lens, the posterior of the capsule, and move anteriorly toward the anterior chamber. This limits the complexity of the laser patterns

170

that are used to treat the capsule and requires that the laser interaction be complete when treating

the capsule. It was found that the most consistent laser interactions occurred when the axial

spacing between focal spots was 10% of the photodisruption length, as measured in water. A

summary plot of the laser interaction region versus laser fluence shows that the laser interaction

region of all the fluence levels tested was comparable (Figure 114). The large area of capsule

affected by laser interaction compared to the size of the photodisruption capsule puncture defect

appears to be due to the shock wave and heating of the capsule by the laser.
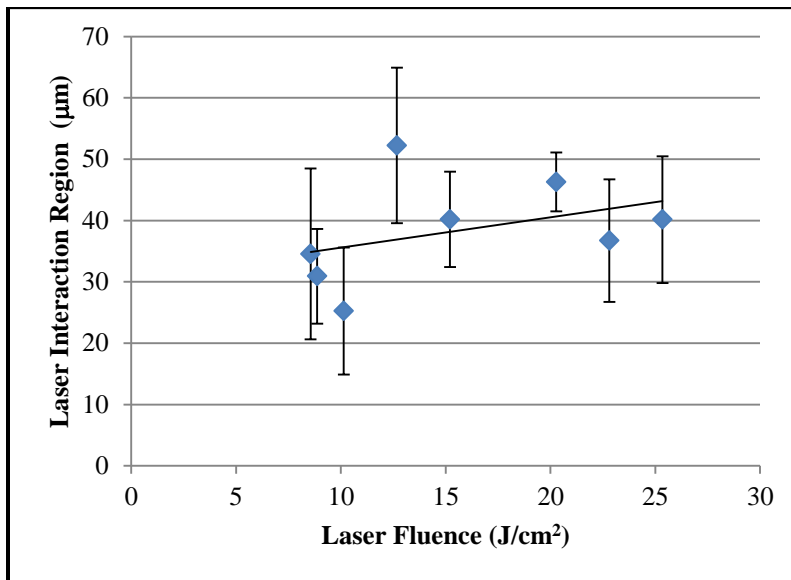
Figure 114 Laser interaction zone versus fluence for 10% fluence photodisruption length.

In Summary:

- Axial focal spot placement greater than 10% of a fluence level's photodisruption
  length did not photodisrupt the capsule in every targeted location.

- For an axial focal spot spacing of 10% of a fluence level's photodisruption length,
  the total laser interaction zones were comparable in size of the interaction zone as
  shown in Figure 115.

- 25.34 J/cm^2 resulted in a photodisruption puncture of 7.3 μm. This fluence should be used to dissect the capsule because it will result in the fastest surgery time.

- The research done has examined a fluence range of 7.60 J/cm^2 to 25.34 J/cm^2 for a 10ps laser. Future work should look at regions outside of this zone of interaction.

- The laser system was effective at treating porcine eyes. This work should be continued into cadaver eyes.

CHAPTER 8 SUMMARY AND CONLUSIONS

This chapter summarizes previous chapters demonstrating the objective of the study has been met. The chapter is organized to show findings, conclusions, and areas for further research. State of the art considerations resulting from this effort are listed along with a final summary.

In Chapter 1, the objectives of this study to look at 10 ps laser interaction at the boundary between the anterior chamber and the crystalline lens were summarized. This region of the eye presents a unique set of problems for laser physics. In this area, the aqueous environment of the anterior chamber contacts the collagenous matrix of the lens capsule and the lens capsule is in direct contact with the fibrous mass of the lens. The lens capsule in human eyes is approximately 20 μm in thickness; it is about 40 μm thick in the porcine eye, which was used as a model for this study. The capsular thickness is less than the Rayleigh range of an F\4.2 laser system, 118 μm in water, but the fibrous mass of the lens and anterior chamber are larger than the Rayleigh range of the laser. To photodisrupt the capsule, the covalent amide bonds must be broken. The binding energy of the amide bond is greater than the binding energy for the water bonds that are more prevalent in the aqueous humor and the fibrous mass of the lens. This may cause an incomplete or partial interaction of the laser with the capsule, resulting in a failure to adequately dissect the lenticular capsule when treated with the laser.

In Chapter 2, the anatomy and biomechanics of the human eye were examined to define the environment in which the laser interaction would occur. In this study, ultrasound A-scan data from Filipino cataract surgery patients indicated significant variability in the exact location

of lens with respect to the epithelium of the cornea. This anticipated natural variation required the system design to accurately locate and measure defined parameters within the anterior chamber of the eye. The beam directing system directs the laser where to focus the laser pulses. The scanning system must be able to define and locate the focal spot of the laser in 3 dimensions to accurately perform a capsulotomy. Patient data was used to build an optical model to look at the optical performance in the eye with increasing age. The model suggests a gradual degradation in the optical performance of the eye with age. Within the Filipino population, the spot size on the retina for the model of an average 80 year old Filipino was 1 micron larger than the spot size for the model of an average 27 year old Filipino. This is the first time an optical model based on the Filipino population has been made. Other effects of aging on the eye were examined to understand cataract development and the need for removal of the fibrous mass of the lens as part of the standard of care.

The usual procedure for capsulorhexis (capsule tearing) involves a small stab incision in the sclera just posterior to the limbal margin. Through this incision the surgeon injects a viscoelastic material to protect the cellular lining of the cornea and the tissues of the uvea (iris and ciliary body). The surface of the capsule is punctured using a needle with an angle in the sharp beveled tip. The surgeon than grasps the edge of the capsular rent and by using delicate traction tears a circular window in the anterior lens capsule. This delicate manual technique is being replaced by the 10 picosecond laser capsulotomy. To achieve better results and outcomes for cataract patients undergoing this laser operative procedure, the interaction of the 10 picosecond laser with each of the boundary between the anterior chamber and the crystalline lens was needed.

In Chapter 3, the laser physics that occur in the formation of plasma was developed. This work was based on the contributions of Kennedy (107), Noack and Vogel (104), Zhou (115), and Keldysh (110). Their work enabled a means to determine a theoretical threshold for plasma. Additionally, a means to look at the laser interaction thermally to determine the temperature evolution of a pulse was developed. This model indicated that the temperature rise in water would be several hundred Kelvin for an 8.55 J/cm^2 10ps pulse. This indicates that the capsule would be heated by the laser system. This model also allowed the shockwave velocity resultant from a laser pulse to be calculated. It was found to be in good agreement with data collected for the 10 picosecond laser in water. However, the model failed to account for the trapping that occurs in the fibrous mass because the water is contained in cells. There is limited information on thermal impact by laser interaction in these conditions. Further study in this area is needed to learn more about the thermal impact of the laser interaction in confined media such as the fibrous mass.

In Chapter 4, the laser interaction at the boundary between the anterior chamber and the lens was modeled. A new multi-material interaction model that considers the three materials in contact was used to examine the evolution of the plasma. This type of model is unique in that it does not require a continuous material to describe the evolution of the electron density. The model used a threshold density to define plasma threshold. The anatomy of the eye presents a unique problem that this model addressed. Before modeling the interaction, consideration of using the approximation made by Kennedy, Noack, and Vogel of a large Keldysh coefficient, $\gamma \gg 1$, was evaluated. This was relevant to study laser interaction at the interface between the lens and anterior chamber because it may lead to an overestimation of plasma length. It was found that the large Keldysh coefficient approximation resulted in an over estimation of electron

population at power levels 10 times threshold of 2.7×10^{21} per cm^3. At powers of 3 times

threshold the approximation only overestimated the electron population by 7.8×10^{20} per cm^3.

The new multi-material interaction model was compared to the moving breakdown model. The

multi-material interaction model predicted a plasma length that was 3 microns smaller than the

moving breakdown model. The model determined the start and stop times of the plasma along

the axial length of the plasma that allowed the model to be used to examine the temporal

evolution of the plasma. This indicated that the plasma was very short duration; only lasting

approximately 11.5ps for the 10 ps laser pulse. The model used a piecewise continuous function

that described the plasma shielding attenuation length. This allowed the model to make

predictions about laser interaction at the interface between the anterior chamber and the lens.

The multi material interaction model predicted that it was possible for the laser to not effectively

photodisrupt the capsule, yet start plasma before and after the capsule. Experiment with porcine

capsules showed regions where the capsule was not treated by the laser. It was inconclusive as

to whether this was due to the plasma location relative to the capsule. Future work to study the

effectiveness of this model should include algorithms that allow the Keldysh coefficient to be

more quickly calculated.

In Chapter 5, a state of the art laser system used to treat eyes was reviewed. This laser

was able to cut 3 dimensional patterns in the eye at the depth of the lens. The 3-dimensional

movement of the focal spot was necessary for treatment of the patient population due to patient

to patient variability. A brief overview of a beam directing system that is capable of determining

where to place laser focus was presented. Other highlights detailed in Chapter 5 including the

difficulty with the slit laser/camera system that impacted overall system performance. Future

efforts should consider an incoherent light such as Superluminescent Light Emitting Diodes

(SLEDs) as a source. A SLED would be helpful in reducing the speckle in the images captured by CCD sensor. This would allow a more accurate interpretation of the capsule surface of the lens. Using the Scheimpflug technique on the CCD would also be useful in improving the image quality of the lens surfaces being observed. A final improvement in the diagnostic system would be to orient the camera and SLED on different optical axes.

In Chapter 6, the evolution of the photo disruption pulse in water and in gelatin was studied. The photodisruption length for various fluence levels was determined in water using the laser system. The lengths of the photodisruption column in gelatin was also found and compared. The gelatin photodisruption length was compared to the photodisruption length in water. There is a difference of 35 μm in length at laser fluence of 25.34 J/cm$^{2.}$ It was found that the threshold fluence found in water also caused photodisruption in the gelatin. Threshold was found to be 8.55 J/cm^2 in water and gelatin. The evolution of photodisruption due to the laser pulse in gelatin examined to determine how the photodisruption bubbles evolved. The photodisruption bubble grows very uniformly for approximately 50 μs at a rate of 0.58 μm/μs., but then starts to oscillate. The bubble evolution indicates that there is an advantage to using higher frequencies for treating materials like gelatin or the fibrous mass. The advantage is that laser pulse can be packed closer together without the previous pulse's photodisruption bubble interfering with the successive pulses. This is the first time that the evolution of the photodisruption bubble has been studied in gelatin using a scanning system. More work should be done to explore the evolution of the bubble for higher fluence levels. Similar work in shorter pulse lasers should be compared to the work done at 10ps.

In Chapter 7, the interaction of the laser system with porcine eyes was examined. Relevant data from earlier chapters was used to develop the experiment. The experiment used axial focal spot separations relative to the length of the photodisruption length measured in water to examine laser interaction with the fibrous mass and capsule. Laser interaction was studied from 6.3 to 25.3 J/cm^2. Threshold in the fibrous mass was found to be 8.55 J/cm^2 for the 10 ps laser. Threshold in the capsule was found to be 10.14 J/cm^2 for the 10 ps laser. Observations were made that many of the patterns used to treat the capsule had regions that did not photodisrupt. The only exception to the incomplete photodisruption rings was for the axial length spacing of equal to 10% of the photodisruption length. Figure 115 shows the rings of photodisruption events in a porcine eye at 25.3 J/cm^2. The 86 μm axial spacing ring, 25% of photodisruption length, did not photodisrupt at each targeted sight. In cataract surgery this would result in the dissection of the capsule being incomplete. The surgeon would have to perform a manual capsulorhexis on the part of the capsule that was not treated by the laser. This could cause surgical complications such as a tear in the capsule. This tear could effect IOL placement in the capsular bag. Figure 115, demonstrates laser treatment of the inner ring was limited by the photodisruption puncture size. This indicates that the focal spot placement to ensure dissection of the capsule must be less than the photodisruption puncture size. Figure 116 shows the effective puncture size versus laser fluence. To dissect the capsule with the laser, the focal spot placement is limited by the puncture size made by the photodisruption and in the uncertainty in its size and focus position of the laser. These uncertainties reduce the distance possible between focal spots to ensure that the capsule is dissected. The uncertainty in focal spot placement was found in Chapter 5 to be 0.79 μm. The uncertainty in the photodisruption puncture size is 0.59 μm. For 25.34 J/cm^2 this corresponds to a shot spacing of 4.59 μm to

ensure that 95.4% of the photodisruption punctures overlap. Figure 117 shows surgical times based on 95.4% overlap for z spacing equal to 10% of the fluence photodisruption length for a 5.25 mm capsulotomy. This plot indicates that the highest fluence has the greatest advantage for surgical time taken to dissect the capsule. Assuming that the capsular strength for each laser fluence level is equal, the highest fluence is the best for surgical application.

Figure 115 Capsulotomy pattern in porcine capsule at laser fluence of 25.3 J/cm^2 at axial, z, spacing indicated.
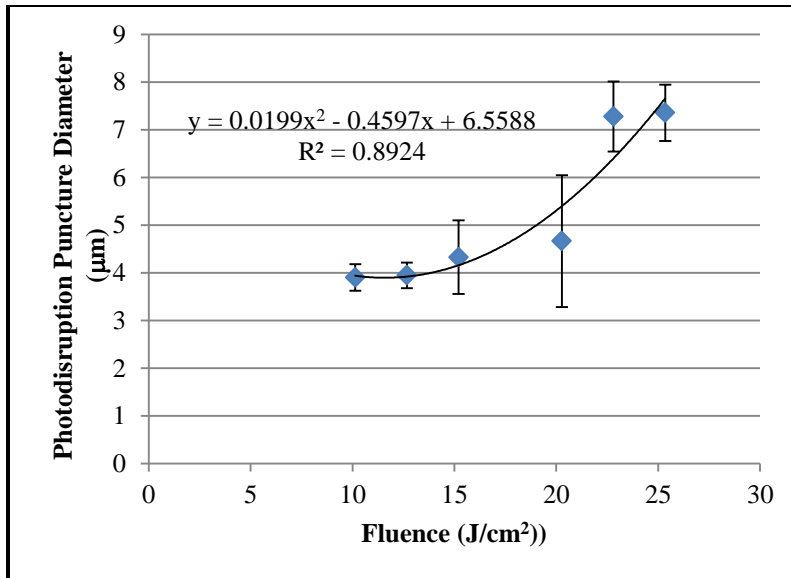
Figure 116 Puncture sizes of photodisruption in porcine capsule with fluence.
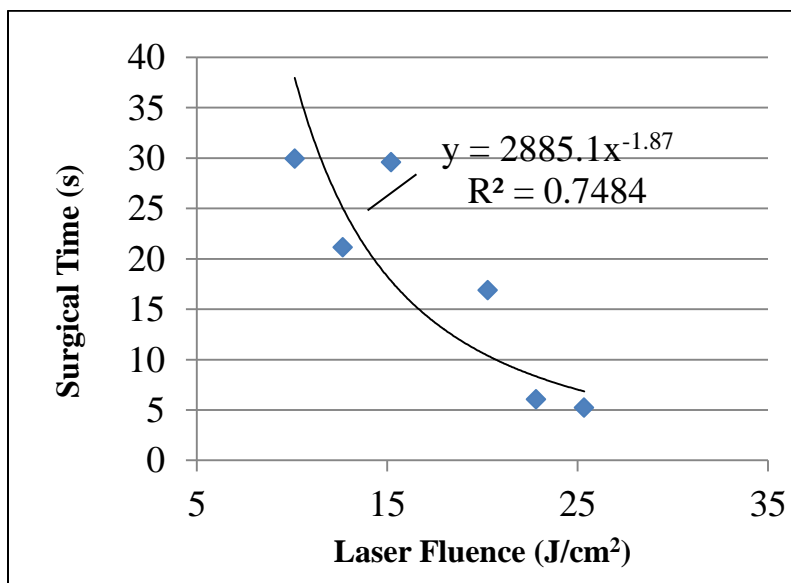
Figure 117 Surgical Time with fluence for laser at 20 kHz.

To test the before mentioned analysis of capsulotomy focal spot spacing, 10 porcine eyes treated with the capsulotomy pattern with focal spot spacing of 3μm laterally and 35 μm axially. The corneas of the porcine eyes were removed and the laser dissected capsule was removed using capsulorhexis forceps. The capsules were removed with minor attachment points without incident. An image of one of the capsular buttons is presented in Figure 118
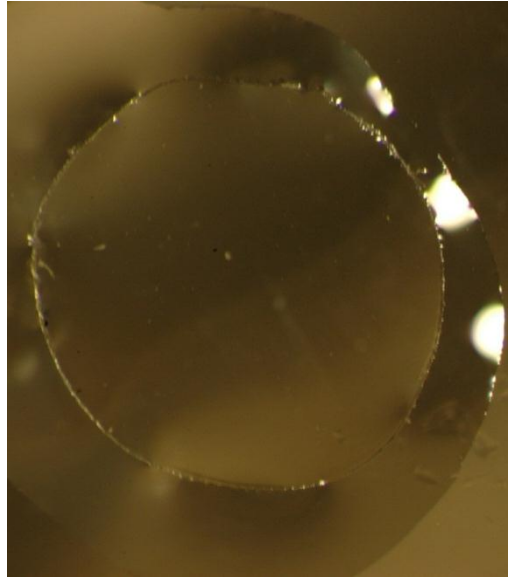
Figure 118 Micrograph of capsular button cut with 3 μm lateral and 35 μm axial spacing.

Throughout this experiment, various leading edge technologies and procedures were included. A short summary of these state of the art findings is listed below.

In Chapter 2, an optical model based on Filipino clinical data was presented. This model represents the first time an optical eye model based on variability in the ophthalmic anatomy of a Filipino population has been presented. This model is likely unique to this population and only considered the biometrics of this population.

In Chapter 4, a Multi-Material Interaction Model was presented. This model introduced a method to study the plasma growth across the boundary at the crystalline lens and anterior chamber. This is the first time a model like this has been constructed where multiple transparent materials were modeled at the boundary where a plasma ignites across it. This model indicated that there were conditions where the plasma would not form in the capsule. This model also predicted failure in the moving breakdown model in predicting the plasma length across the boundary.

In Chapter 5, a state of the art laser system was introduced that is capable of delivering laser pulses into an eye. This is a system targets the lens inside of the eye without physically entering the eye. This system uses a state of the art beam directing system to adjust the focal position of laser system in the eye. The laser is capable of scanning in 3-dimensions producing random user defined patterns.

In Chapter 6, the bubble evolution of an F/4.2 series of laser pulses was measured. This is the first time this has been done for a 10ps laser using a scanning system. This allowed an optical snapshot of the bubble evolution to be considered over a 90 μs period. This technique offers a new methodology to study interaction physics in materials.

In Chapter 7, a study of ex vivo porcine eyes using a 10 ps laser was done to examine interaction across the capsule as a function of axial focal spot spacing. This is the first time a study of this type has been done in porcine eyes using an F/4.2 10ps laser system. This experiment demonstrated the need for close axial spacing for successive axial spaced focal spots to get a uniform effect across the capsule. The optimal spacing from these experiments was found to be 10% of the fluence level's photodisruption length.

FINAL SUMMARY

In conclusion, laser interaction at the boundary between the lens and the anterior chamber has been investigated. The results of this investigation are reflected in Table 12. A summary of the achievements by priority are shown in the first column. Column two shows the major impact from this experimental effort for each achievement. The next column identifies possible steps in moving these finds forward. The last column shows the possible end point with a similar treatment laser system for treating humans. This work has identified the required system

parameters to treat the capsule using a surrogate porcine eye. This work can now be used to

guide work in cadaver eyes. This is the next step to treating human eyes in the clinic.

Table 12 Table of Study Achievements, Impact, Next steps for research, and Human studies

Priority	Achievements	Impact	Next steps	Human Studies
1	Reported Photodisruption effects in the capsule using a 10ps laser.	Found that 10% photodisruption length for a fluence level was more effective at treating the capsule then other lengths studied.	Cadaver eyes need to be studied to see how the effects determined for porcine eyes translate into human eyes.	Starting fluence levels for studying photodisruption in human cadaver eye have been defined.
2	Direction for focal pulse spot spacing to effectively treat the capsule.	Treatment parameters used to examine human eyes have been identified based on a surrogate model of the human eye.	Test this in cadaver eyes.	Direction for focal spot placement has been defined for further testing.
3	Established a threshold in the porcine fibrous mass for a porcine eye using a 10ps laser.	Threshold for porcine fibrous mass is known.	Thermal effects need to be studied as a function of focal spot placement and frequency. In cadaver eyes fragmentation patterns need to be studied.	Studies should consider this as a starting fluence level for non cataractous eyes.
4	Developed new interaction model that describes the electron evolution that leads to plasma formation in multiple materials.	This model allows the interaction across the boundary between the anterior lens and anterior chamber to be examined.	Develop the model to include the complete Keldysh Multiphoton Absorption Treatment to determine the plasma length. Examine the effects of an electron density dependent attenuation term.	Additional studies to validate the model are required.
5	Provided a methodology to treat the lens using a 3-dimensional scanning focal spot laser system with a beam directing diagnostic system.	A laser system that is capable of treating an eye.	Use this system to treat cadaver eyes. Develop focal spot spacing for fibrous mass using phacoemulsification energy to determine effectiveness.	Laser system can treat human eyes in a limited clinical trial at completion of cadaver eye study.
6	Measured the evolution of a photodisruption bubble in surrogate material for the fibrous mass.	The effects of the bubble formation in fixed media will affect successive laser pulses dependent on frequency and focal spot spacing.	Study the effect of increasing energy on bubble growth rates. Study the effects varying frequency in treatment of the capsule.	This is unknown to the impact on human studies. Further effort is needed to determine impact on dissection of human lenses.
7	Developed and utilized an optical model of Filipino eyes with clinical data.	An optical model to study the eye of Filipinos.	Study the effects of cataracts using this model. Build a better model of the lens.	The optical model can be used to further research.

This concludes this study of ps laser interaction at the boundary between the anterior chamber and the lens. The need for additional work has been identified. Various leading edge technologies and procedures involved in this study have moved the body of knowledge forward.

LIST OF REFERENCES

1. *Optical and microwave-optical experimentsin ruby.* **Maiman, T.** 1960, Phy. Rev. Lett, pp. 564-566.

2. *Infrared nd Optical Masers.* **Townes, A.L. Schawlow and C.H.** 6, December 15, 1958, Physical Review, Vol. 112, pp. 1940-1949.

3. *Ocular Lesions produced by an optical maser.* **Zaret, M. M., et al., et al.** 1961, Science, Vol. 134, p. 1525.

4. *Experimental laser photocoagulations.* **Zweng, H. C., et al., et al.** 1964, American Journal of Opthomology, Vol. 58, pp. 353-362.

5. *The optical maser as a retinal coagulator: an evlaution.* **Campbell, C. J., Rittler, M. C. and Koester, C. J.** 1963, American Academy of Opthalmology, Vol. 68, p. 58.

6. *Laser beam effect on dental hard tissues.* **Stern, R. H. and Sognnaes, R. F.** 1964, J. Dent Res., Vol. 43, p. 873.

7. **Niemz, Markolf H.** *Laser-Tissue Interactions (Fundamentals and Applications).* Berlin Heidelberg : Springer-Verlag, 2004.

8. *Photophysicial processes in recent medical laser developments: a revew.* **Boulnois, J.-L.** 1986, Lasers Med. Sci., Vol. 1, pp. 47-66.

9. *The History of Photodetection and Photodynamic Therapy.* **Ackroyd, Roger, et al., et al.** 5, 2007, Photochemistry and Photobiology, Vol. 74.

10. *Photodynamic effects on human cells exposed to light in the presence of hematoporphyrin. Localization of the active dye.* **Moan, Johan and Chirstensen, Terje.** 3, January 1981, Cancer Letters, Vol. 11, pp. 209-214.

11. *Sensitization of Streptococcus sanguis to Killing by Light from a Helium/Neon Laser .* **Micheal Wilson, John Dobson, Wilson Harvey.** 1, s.l. : Springer London, March 1993, Lasers in Medical Science, Vol. 8, pp. 69-73. 0268-8921/93/010069 .

12. Water structure and behavior. [Online] December 7, 2006. [Cited: January 1, 2007.] http://www.lsbu.ac.uk/water/vibrat.html.

13. **Takata, A.N., Zaneveld, L. and Richter, W.** *Laser-induced thermal damage in skin.* Brook eAir Force base, Texas : USAF School of Aerospace Medicine, 1977. SAM-TR-77-38.

14. *Neodymium-YAG laser for posterior capsulotomy.* **AC, Terry, et al., et al.** 6, Dec 1983, Am J Ophthalmol, Vol. 96, pp. 716-20.

15. *A systematic overview of the incidence of posterior capsule opacificati.* **Schaumberg, Debra A, et al., et al.** 7, July 1998, Ophthalmology, Vol. 105, pp. 1213-1221.

16. *Mutation and sister chromatid exchange induction by chinese hamster ovary (CHO) cells by pulsed excimer laser radiation at 193nm and 308nm and continuous UV radiation at 254nm.* **Rasmussen, Ronald E., Hammer-Wilson, Marie and Berns, Micheal W.** 4, 1989, Photochemistry and Photobiology, Vol. 49, pp. 413-418.

17. **Lide, Davide R.** *Handbook of Chemistry and Physics.* Boca Raton : CRC Press, 1992. pp. 10-229. ISBN 0-8493-0473-3.

18. *Short-Pulsed Nd:YAG Laser Microsurgery of the Eye: Biophysical Considerations.* **PULIAFIT, CARMEN A. and STEINERT, ROGER F.** 12, s.l. : IEEE, 1984, IEEE

JOURNAL OF QUANTUM ELECTRONICS, Vol. 20, pp. 1442-1448. 0018-9197/84/1200-144.

19. *Liquid water as a lone pair amorphous semiconductor.* **Williams, F., Varma, S.P. and Hillenius, S.** 4, February 15, 1976, Journal of Chemical Physics, Vol. 64, pp. 1549-1554.

20. *Laser-induced breakdown in the eye at pulse durations from 80 ns to 100 fs.* **Vogel, Alfred, et al., et al.** s.l. : SPIE , 1998, Vol. 3255.

21. *Treatment of Retinopathy of Prematurity With Argon Laser Photocoagulation.* **Maurice B. Landers III, MD, et al., et al.** 1, 1992, Arch Ophthalmol. , Vol. 110, pp. 44-47.

22. *Excimer laser treatment of corneal surface pathology: a laboratory and clinical study.* **Gartry, D., Muir, M. Kerr and Marshall, J.** 1991, Br J Ophthalmol , Vol. 75, pp. 258-269.

23. *Erbium:YAG laser-assisted cataract surgery.* 3, Mar 1998, Ophthalmic Surg Lasers, Vol. 29, pp. 185-9.

24. *Photodisruption in the human cornea as a function of laser pulse width.* **Kurtz RM, Liu X, Elner VM, Squier JA, Du D, Mourou G.** 1997, J Cataract Refract Surg. , Vol. 13, pp. 653-658.

25. *Optimal Laser Parameters for Intrastromal Corneal Surgery.* **Kurtz, Ron M., et al., et al.** 1998, Proceedings SPIE , Vol. 3255. 277-786-81.

26. *Cornea surgery with nanojoule femtosecond laser pulses.* **König, Karsten, et al., et al.** s.l. : Proceedings of SPIE, 2005, Ophthalmic Technologies XV , Vol. 5688.

27. *Study of Photoablation of Rabbit Corneas by Er:YAG Laser.* **Rinaldo Cubeddu, PhD, Rosario Brancato, MD, Carlo Sozzi, PhD, Paola Taroni, PhD, Giuseppe Trabucchi, MD, Gianluca Valentini, PhD, and Mariangela Verdi, MD.** 1996, Lasers in Surgery and Medicine, Vol. 19, pp. 32-39.

28. *Custom photorefractive keratectomy ablations for the correction of spherical and cylindrical refractive error and higher-order aberration.* **Schwiegerling, Jim and Snyder, Robert W.** 9, September 1998, J. Opt. Soc. Am. A, Vol. 15, pp. 2572-2579.

29. *Femtosecond Optical Ranging of Corneal Incision Depth.* **Stern, David, et al., et al.** 1, January 1989, Investigative Ophthalmology & Visual Science, Vol. 30.

30. *Ti me-Resolved Observations of Shock Waves and Cavitation Bubbles Generated by Femtosecond Laser Pulses in Corneal Tissue and Water.* **Juhasz, Tibor, et al., et al.** s.l. : Wiley-Liss, Inc, 1996, Lasers in Surgery and Medicine, Vol. 19, pp. 23-31.

31. *Femtosecond Laser Corneal Refractive Surgery.* **Kurtz, Ron, et al., et al.** s.l. : SPIE, January 1999, Ophthalmic Technologies IX, Vol. 3591.

32. *First safety study of femtosecond laser photodisruption in animal lenses: Tissue morphology and cataractogenesis.* **Krueger, Ronald R., et al., et al.** 12, December2386-2394 2005, Journal of Cataract & Refractive Surgery , Vol. 31, pp. 2386-2394.

33. *Initial clinical experience with the picosecond Nd:YLF laser for intraocular therapeutic applications.* **Geerling, Gerd, et al., et al.** 1998, Br J Ophthalmol , Vol. 82, pp. 504–509.

34. *Femtosecond laser-assisted cataract surgery.* **He L, Sheehy K, Culbertson W.** Dec 9, 2010 , Curr Opin Ophthalmol. .

35. *How a femtosecond laser increases safety and precision in cataract surgery?* **Naranjo-Tackman, Ramon.** Dec 9, 2010, Curr Opin Ophthalmol. .

36. *Femtosecond laser-assisted cataract surgery with integrated optical coherence tomography.* **Palanker DV, Blumenkranz MS, Andersen D, Wiltberger M, Marcellino G, Gooding P, Angeley D, Schuele G, Woodley B, Simoneau M, Friedman NJ, Seibel B, Batlle J, Feliz R, Talamo J, Culbertson W.** 58, Nov 17, 2010, Sci Transl Med., Vol. 2.

37. *Crystalline lens photodisruption using femtosecond laser: experimental study.* **Chatoux O, Touboul D, Buestel C, Balcou P, Colin J.** 7, Sep 2010 , J Fr Ophtalmol., Vol. 33, pp. 472-80.

38. *Initial Clinical Evaluation of an Intraocular Femtosecond Laser in Cataract Surgery.* **Zoltan Nagy, MD, Agnes Takacs, MD and Tamas Filkorn, MD and Melvin Sarayba, MD.** 12, December 2009, Journal of Refractive Surgery , Vol. 25.

39. LensAR Corporate Page. *www.lensar.com.* [Online] 2010.

40. LensX Corporate Site. *www.lensxlasers.com.* [Online]

41. Optimedica Corporate Website. *www.optimedica.com.* [Online]

42. Technolas Corporate Website. *www.technolaspv.com.* [Online]

43. *Intraocular Nd:YAG laser surgery laser-tissue interaction, damage range, and reduction of collateral effects .* 12, December 1990, IEEE Journal of Quantum Electronics, Vol. 26.

44. *Tissue Dissection with Ultrafast Laser using Extended and Multiple Foci .* **I. Toytman, A. Silbergleit, D. Simanovski, D. Palanker.** s.l. : SPIE, 2040, SPIE Proceedings, Optical Interactions with Tissues and Cells XXI, Vol. 7562.

45. *MEASURING THE BIAXIAL STRESS-STRAIN CHARACTERISTICS OF HUMAN SCLERA.* **C.G. Olesen, I. Tertinegg, A. Eilaghi, G.W. Brodland, C. Horst, J.H. Veldhuis, J.G. Flanagan, C.R. Ethier.** 176531, Keystone : s.n., June 20-24, 2007, Proceedings of the ASME 2007 Summer Bioengineering Conference, Vol. SBC2007.

46. **Kaufman, Paul L. and Alm, Albert.** *Adler's Physiology of the Eye.* St. Louis : Mosby, 2002. 0-323-01136-5.

47. *The Role of the Iris in Accommodation of Rhesus Monkeys.* **Kathryn S. Crawford, Paul L. Kaufman, and Laszlo Z. Birof.** 10, 1990, investigative ophthalmology and visual science, Vol. 31, pp. 2185 – 2190.

48. **William J. Benjamin, OD, MS, PhD.** *Borish's Clinical Refraction, 2nd Edition.* New York : Elsevier, 2007. ISBN: 978-0-7506-7524-6.

49. *Presbyopia and Optical Changes in the Human Crystalline Lens with Age.* **Glasser, Adrian and Campbell, Melanie C. W.** 2, s.l. : Elsevier Science, 1998, Vision Res., Vol. 38, pp. 209-229. 0042-6989/98.

50. *Intraocular Light Scattering in Age-Related Cataracts.* **Waard, Peter W. T. de, et al., et al.** 3, s.l. : Association for Research in Vision and Ophthalmology, 1992, Investigative Ophthalmology & Visual Science, Vol. 33.

51. *Distribution, spherical structure and predicted Mie scattering of multilamellar bodies in human age-related nuclear cataracts.* **Gilliland, Kurt O., et al., et al.** s.l. : Elsevier Ltd., 2004, Experimental Eye Research, Vol. 79, pp. 563–576.

52. **Atchison, David A. and Smith, George.** *Optics of the Human Eye.* Edinburgh : Elsevier Science, 2003. 0750637757.

53. *The Aging Cornea.* **Faragher, R G A, B Mulholland, S J Tuft and S Sandeman, P T Khaw.** 1997, British Journal of Ophthalmology, Vol. 81, pp. 814–817.

54. *A comparative study of Bowman's layer in some mammals: Relationships with other constituent corneal structures.* **Merindano, Mª.D., et al., et al.** 3, 2002, Eur J Anat, Vol. 6, pp. 133-139 .

55. *The architecture of the corneal stroma.* **BRON, A J.** 2001 , British Journal of Ophthalmology, Vol. 85, pp. 379-381.

56. *Collagen Fibrils Appear More Closely Packed in the Prepupillary Cornea: Optical and Biomechanical Implications.* **Boote, Craig, et al., et al.** 7, s.l. : Association for Research in Vision and Ophthalmology, July 2003, Investigative Ophthalmology & Visual Science, Vol. 44.

57. **Schwiegerling, Jim.** *Field Guide to Visual and Ophthalmic Optics (SPIE Press Book).* s.l. : SPIE, 2 November 2004. ISBN: 9780819456298.

58. *The chemical composition of the human aqueous humour in normal and pathological conditions.* **Berardinis, E. de, et al., et al.** 3, September 1965, Experimental Eye Research, Vol. 4, pp. 179-186.

59. *Fiber Cell Denucleation in the Primate Lens.* **Bassnett, Steven.** 9, August 1997 1997, Investigative Ophthalmology & Visual Science, Vol. 38.

60. *Refractive index distribution and optical properties of the isolated human lens measured using magnetic resonance imaging (MRI).* **Jones, C.E., et al., et al.** s.l. : Elsevier, 2005, Vision Research , Vol. 45, pp. 2352–2366.

61. *A Review of Literature on the Crystaline Lens.* **Adams, Dorothy Rose.** 1925, Br J Ophthalmol, Vol. 9, pp. 281-299.

62. *The mechanism of presbyopia.* **Strenk, Susan A., Strenk, Lawrence M. and Koretz, Jane F.** 3, s.l. : Elsevier Ltd , 2005, Progress in Retinal and Eye Research, Vol. 24, pp. 379-393 .

63. *Accommodation and Presbyopia in the Human Eye: Changes in the Anterior Segment and Crystalline Lens With Focus.* **Koretz, Jane F., Cook, Christopher A. and Kaufman, Paul L.** 3, s.l. : Association for Research in Vision and Ophthalmology, March 1997, Ophthalmology & Visual Science, Vol. 38.

64. *What causes steroid cataracts? A review of steroid-induced posterior subcapsular cataracts.* **Andrew I Jobling BScHons PhD, Robert C Augusteyn BScHons PhD DipEd FVCO.** 2, 2009, Clinical and Experimental Optometry, Vol. 85.

65. *Lens-specific expression of transforming growth factor beta1 in transgenic mice causes anterior subcapsular cataracts.* **Y Srinivasan, F J Lovicu, and P A Overbeek.** 3, February a, 1998, J Clin Invest. , Vol. 101, pp. 625–634.

66. *THE EPIDEMIOLOGY OF SENILE CATARACTS: A REVIEW.* **SPERDUTO2, M. CRISTINA LESKE1 AND ROBERT D.** 2, 1983, AMERICAN JOURNAL OF EPIDEMIOLOGY, Vol. 118.

67. *Gamma-D crystallin gene (CRYGD) mutation causes autosomal dominant congenital cerulean cataracts.* **E Nandrot, C Slingsby, A Basak.** 2003 , J Med Genet, Vol. 40, pp. 262-267.

68. *The γ-Crystallins and Human Cataracts: A Puzzle Made Clearer.* **Elise Héon, 1,2,3 Megan Priston,1 Daniel F. Schorderet,4 Gail D. Billingsley, Philippe Othenin Girard, Nicolette Lubsen, and Francis L. Munier.** 5, November 1999, Am J Hum Genet. , Vol. 65, pp. 1261–1267.

69. *The Search for a Solution to Senile Cataracts.* **Specror, Abraham.** February 1984, INVESTIGATIVE OPHTHALMOLOGY G VISUAL SCIENCE, Vol. 25.

70. *LOCS III versus the Oxford Clinical Cataract Classification and Grading System for the assessment of nuclear, cortical and posterior subcapsular cataract.* **Hall AB, Thompson JR, Deane JS, Rosenthal AR.** 4, Dec 1997, Ophthalmic Epidemiol, Vol. 4, pp. 179-94.

71. *Lens opacities classification system II (LOCS II).* **L T Chylack Jr, M C Leske, D McCarthy, P Khu, T Kashiwagi, R Sperduto.** 7, Jul 1989, Arch Ophthalmol, Vol. 107 , pp. 991-7.

72. *Cataract classification.* **Hockwin, Otto.** 3-4, March 1995, Documenta Ophthalmologica, Vol. 88, pp. 263-275.

73. *A simplified cataract grading system.* **Thylefors B, Chylack LT Jr, Konyama K, Sasaki K, Sperduto R, Taylor HR, West S.** 2, Apr 2002 , Ophthalmic Epidemiol., Vol. 9, pp. 83-95.

74. *A simple accurate method of cataract classification Cataract I.* **Sharma YR, Vajpayee RB, Bhatnagar R, Mohan M, Azad RV, Kumar M, Nath R.** 1989, Indian J Ophthalmol, Vol. 37, pp. 112-7.

75. **Fannin, Troy E. and Grosvenor, Theodore.** *Clinical Optics.* Boston : Butterworth-Heinemann, 1996. ISBN 0-7506-9670-2.

76. *Laser in situ keratomileusis monovision.* **Goldberg, Daniel B.** 9, September 2001, Journal of Cataract & Refractive Surgery, Vol. 27, pp. 1449-1455.

77. *Photopic pupillometry–guided laser in situ keratomileusis for hyperopic presbyop.* **Kerry K. Assil, MD, Steve H. Chang, Sunil G. Bhandarkar, Julie M. Sturm, William K. Christian.** 2008, J Cataract Refract Surg, Vol. 34, pp. 205–210.

78. *Femtosecond laser in situ keratomileusis versus conductive keratoplasty to obtain monovision in patients with emmetropic presbyopia.* **Ayoubi, Mohammad Ghassan.** s.l. : ASCRS and ESCRS, 2010, J Cataract Refract Surg, Vol. 36, pp. 997–1002.

79. **Wallace, Bruce.** *Refracive Cataract Surgery and Multifocal IOLS.* Thorofare : Slack, 2001. ISBN 1-55642-460-4.

80. *Correction of presbyopia with refractive multifocal phakic intraocular lenses.* **Baïkoff, Georges, et al., et al.** s.l. : ASCRS and ESCRS, 2004, J Cataract Refract Surg, Vol. 30, pp. 1454–1460.

81. *Multifocal Intraocular Lenses.* **Lane, Stephen S., et al., et al.** 1, March 2006, Ophthalmology Clinics of North America, Vol. 19, pp. 89-105.

82. *Intraocular implants for the surgical correction of presbyopia.* **Parel, Jean-Marie, et al., et al.** s.l. : SPIE, 2000, In Ophthalmic Technologies X, Proceedings of SPIE, Vol. 3908, pp. 115-122.

83. *Lens refilling to restore accommodation.* **Nishi, Yutaro, et al., et al.** 2, February 2009, Journal of Cataract & Refractive Surgery , Vol. 35, pp. 374-382.

84. *Capsular bag refilling using a new accommodating intraocular lens .* **Nishi, Okihiro, et al., et al.** s.l. : ASCRS and ESCRS, 2008, J Cataract Refract Surg, Vol. 34, pp. 302–309 .

85. *Fs-laser induced elasticity changes to improve presbyopic len accommodation.* **Ripken, T., et al., et al.** 2005, Proceedings SPIE, Vol. 5688.

86. *Experimental increase in accommodative potential after neodymium:yttrium–aluminum–garnet laser photodisruption of paired cadaver lenses.* **Krueger, Ronald R, et al., et al.** 11, November 2001, Ophthalmology , Vol. 108, pp. 2122-2129.

87. *Combined phacoemulsification and pars plana vitrectomy: clear corneal versus scleral incisions: Prospective randomized multicenter study.* **Arnd Heiligenhaus, Alexa Holtkamp, Jörg Koch, Harald Schilling, Norbert Bornfeld, Cay Christian Lösche, Klaus-Peter Steuhl.** 6, June 2003, Journal of Cataract & Refractive Surgery, Vol. 29, pp. 1106-1112.

88. *Corneal incision quality Microincision cataract surgery versus microcoaxial phacoemulsification.* **Elkady, Bassam, Pinero, David and Alio´, Jorge L.** s.l. : ASCRS and ESCRS, 2009, J Cataract Refract Surg, Vol. 35, pp. 466–474.

89. *Profile of clear corneal cataract incisions demonstrated by ocular coherence tomography.* **Fine, I. Howard, Hoffman, Richard S. and Packer, Mark.** 1, January 2007, Journal of Cataract & Refractive Surgery , Vol. 33, pp. 94-97.

90. *Viscoelastic protection from endothelial damage by air bubbles.* 6, June 2002, Journal of Cataract & Refractive Surgery , Vol. 28, pp. 1047-1053.

91. *Ultrasonic transmission in viscoelastic substances.* **Andreas Frohn, Hans Burkhard Dick, Claus Peter Fritzen, Manfred Breitenbach, Hans Jürgen Thiel.** 2, February 2000, Journal of Cataract & Refractive Surgery, Vol. 26, pp. 282-286.

92. *Anterior chamber maintainer versus viscoelastic material for intraocular lens implantation: case-control study.* **Bradford J Shingleton, Peter V Mitrev.** 5, May 2001, Journal of Cataract & Refractive Surgery , Vol. 27, pp. 711-714.

93. *A comparative study of the elastic properties of continuous tear curvilinear capsulorhexis versus capsulorhexis produced by radiofrequency endodiathermy.* **Luck, J, Brahma, A K and Noble, B A.** 1994, Br J Ophthalmol, Vol. 78, pp. 392-396.

94. *Effect of Continuous Circular Capsulorhexis and Intraocular Lens Fixation on the Blood-Aqueous Barrier.* **Tsuboi, Shunji, et al., et al.** 1992, Arch Ophthalmol, Vol. 110.

95. *Continuous curvilinear (circular) capsulorhexis and planned extracapsular cataract extraction--are they compatible?* **Pande, M.** 1993, Br J Ophthalmol , Vol. 77, pp. 152-157.

96. *Anterior capsulotomy with a pulsed-electron avalanche knife.* s.l. : ASCRS and ESCRS, 2010, J Cataract Refract Surg, Vol. 36, pp. 127–132.

97. *The History of the Capsulorhexis Technique.* **GIMBEL, HOWARD V.** OCTOBER 207, CATARACT & REFRACTIVE SURGERY TODAY, pp. 39-41.

98. *Effect of hydrodissection alone and hydrodissection combined with rotation on lens epithelial cells: Surgical approach for the prevention of posterior capsule opacification.* **Abhay R. Vasavada, Shetal M. Raj, Kaid Johar, Mayank A. Nanavaty.** 1, January 2006, Journal of Cataract & Refractive Surgery, Vol. 32, pp. 145-150.

99. *Effect of hydrodissection on intraoperative performance: randomized study.* **Vasavada, Abhay R, et al., et al.** 9, September 2002, Journal of Cataract & Refractive Surgery, Vol. 28, pp. 1623-1628.

100. **Jackson, J.D.** *Classical Electrodynamics.* New York : John Wiley and Sons, Inc, 1975. 0-471-43132-X.

101. **Saleh, Bahaa E. A. and Teich, Malvin Carl.** *Fundamentals of Photonics.* New York : John Wiley and Sons, Inc., 1991. 0-471-83965-5.

102. **Nibbering, E.T.J., et al., et al.** Measurement of the nonlinear refractive index of transparent materials by spectral analysis after nonlinear propagation. *OPTICS COMMUNICATIONSS.* September 15, 1995, Vol. 119, pp. 479-484.

103. **Koechner, Walter.** *Solid State Laser Engineering.* New York : Springer-Verlag, 1999. 3-540-65064-4.

104. *Laser-Induced Plasma Formation in Water at Nanosecond to Femtosecond Time Scales: Calculation of Thresholds, Absorption Coefficients, and Energy Density.* **Noack, Joachim and Vogel, Alfred.** 8, s.l. : IEEE, 1999, Vol. 35, pp. 1156-1167.

105. **Paschotta, R.** *Field Guide to Lasers.* Bellingham : SPIE Press, 2008.

106. *Laser-Induced Electric Breakdown in Solids.* **Bloembergen, Nicolaas.** 3, s.l. : IEEE, March 1974, Quantum Electronics, Vol. 10, pp. 375-386.

107. *A First Order Model for Computation of Laser Induced Breakdown Thresholds in Ocuar and Aquesous Media: Part I- Theory.* **Kennedy, Paul K.** 12, s.l. : IEEE, December 1995, Quantum Electronics, Vol. 31, pp. 2241-2248.

108. **Arnold, D and Cartier, E.** Theory of laser-induced free-electron heating and impact ionization in wide-band-gap solids. *Phys. Rev. B.* 1992, Vol. 46, pp. 15102-15115.

109. *Theory and simulation on the threshold of water breakdown induced by focused ultrashort laser pulses.* **Feng, Q., et al., et al.** 2, s.l. : IEEE, 1997, Vol. 33.

110. *Ionization in the field of a strong eectromagnetic wave.* **Keldysh, L. V.** 5, May 1965, Vol. 20, pp. 1307-1314.

111. *Laser Induced Gas Breakdown: A ibliographical Review.* **DEMICHELIS, CLAUD10.** 4, s.l. : IEEE JOURNAL OF QUANTUM ELECTRONICS,, April 1969, Vols. QE-5, pp. 188-202.

112. **Vogel, A., et al., et al.** Mechanisms of femtosecond laser nanosurgery of cells and tissues. *Applied Physics B.* November 15, 2005, Vol. 81, pp. 1015-1047.

113. **Haberman, Richard.** *Elementary Applied Partial Diferential Equations.* Englewood Cliffs : Prentice-Hall Inc, 1987. 0-13-252875-4.

114. *Non-Invasive Determination of Shock Wave Pressure Generated by Optical Breakdown.* **Doukas, A. G., et al., et al.** 1991, Appl. Phys. B , Vol. 53, p. 237 245.

115. *Numerical modeling of transient progression of plasma formation in biological tissues induced by short laser pulses.* **zhou, j., chen, j.k. and zhang, y.** 2008, Appl. Phys. B, Vol. 90, pp. 141–148. 10.1007/s00340-007-2843-z.

116. Lumera Laser. *Lumera Laser Web Page.* [Online] [Cited: 03 31, 2007.] http://www.lumera-laser.com/index2.html.

117. **Labs, Scan.** Installation and Operation Operation for intelliSCAN®10. Germany : Scan Labs, 2006. www.scanlab.de.

118. *The Use of an Off Axis Slit Laser Camera System for Determining Photodisruptive Laser Placement in Lenses.* **T. Olmstead, G. Gray, N. Zepkin, R. Frey.** 6-10 May 2007. ARVO. p. B573 #3835 .

119. *The physical properties of gelatin solutions and gels.* **Ward, A. G.** March 1954, Br. J. Appl. Phys. , Vol. 5.

120. *The Science and Technology of Gelatin.* **Ward, A.G. and Courts, A.** New York : Academic Press, 1977.

121. *Biosynthesis and Degradation of Collagen in Connective tissue in meat and meat products.* **Genes, A.J. Baily and N.D. Light.** London : Elsevier Applied Science, 1989.

122. rain x Original Glass Treatment. [Online]

http://www.rainx.com/Products/Windshield_Treatment/Original.aspx.

123. *Noncontact Specular Microscopy of Human Lens Epithelium.* **Mini Balaram, William H. Tung, Jerome R. Kuszak, Masahiko Ayaki,Toshimichi Shinohara, and Leo T. Chylack, Jr.** 2, 2000, Invest Ophthalmol Vis Sci., Vol. 41, pp. 474-481.